

ACTIVE MAGNETIC BEARING CONTROL FOR AN EXPERIMENTAL
FLYWHEEL ENERGY STORAGE SYSTEM

A Thesis

Presented in Partial Fulfillment of the Requirements for the

Degree of Master of Science

with a

Major in Electrical Engineering

in the

College of Graduate Studies

University of Idaho

by

Brent A. Kisling

May 2014

Major Professor: Joseph D. Law, Ph.D.

Authorization to Submit Thesis

This thesis of Brent Kisling, submitted for the degree of Master of Science with a Major in Electrical Engineering and titled “Active Magnetic Bearing Control for an Experimental Flywheel Energy Storage System,” has been reviewed in final form. Permission, as indicated by the signatures and dates below, is now granted to submit final copies to the College of Graduate Studies for approval.

Major Professor: _____ Date: _____
Joseph D. Law, Ph.D.

Committee
Members: _____ Date: _____
Brian K. Johnson, Ph.D.

Christine A. Berven, Ph.D. Date: _____

Department
Administrator: _____ Date: _____
Fred Barlow, Ph.D.

Discipline’s
College Dean: _____ Date: _____
Larry Stauffer, Ph.D.

Final Approval and Acceptance

Dean of the College
of Graduate Studies: _____ Date: _____
Jie Chen, Ph.D.

Abstract

High speed flywheel energy storage (FES) systems are predicted to outperform battery systems in terms of lifetime and energy density. With proper development FES systems could become the new standard in energy storage for space and terrestrial applications. Active magnetic bearings (AMBs) are an enabling technology for FES systems. Flywheel energy storage systems rely on AMBs to suspend the flywheel without physical contact and allow the flywheel to rotate freely at high speeds. Active magnetic bearings provide magnetic suspension forces which are adjusted in response to control feedback to remove incident disturbances on the suspended flywheel. This thesis describes the modeling, simulation, and control system design of two decentralized AMB systems utilized on an experimental FES system built at the University of Idaho. One AMB is a dedicated outer-rotor eight pole system. The other AMB system is integrated within a self-bearing field regulated reluctance machine.

Acknowledgements

I would like to sincerely thank Dr. Joseph Law for his guidance and encouragement over the course of my graduate work. Dr. Law provided me the opportunity to work on this exciting project, and for that I am very grateful. If it was not for his enthusiasm when I first spoke to him regarding a potential graduate research position, I would have left the University of Idaho without a graduate degree, perhaps never to receive one.

I would also like to extend my sincere gratitude:

To Dr. Michael Santora for his valuable knowledge and guidance on microcontrollers, programming, and control systems;

To my committee members Dr. Christine Berven and Dr. Brian Johnson for their time and aid in reviewing this work;

To Kevin Ramus and Bridget Wimer for their feedback and friendship, I could not have remained sane without them;

To Dan Schneider for his help in fabricating numerous aspects of the testing equipment and final design hardware;

To the entire University of Idaho flywheel research team for their feedback, and for exposing me to other interesting academic disciplines;

To my family for their support and for the knowledge that they will always support me throughout all my future endeavors;

To my girlfriend Kate for her support, optimism, and contagious happiness.

Table of Contents

Authorization to Submit Thesis	ii
Abstract	iii
Acknowledgements	iv
Table of Contents	viii
List of Figures	xii
List of Tables	xiii
List of Abbreviations	xiv
Chapter 1: Introduction	1
1.1 Flywheel Energy Storage System	2
1.1.1 Advantages of FES Systems	5
1.2 Magnetic Bearings	7
1.2.1 Magnetic Bearing Classification	7
1.2.2 Earnshaw's Theorem and Permanent Magnet Suspension	10
1.2.3 AMB Advantages and Application to FES Systems	11
1.3 University of Idaho's FES system design	14
Chapter 2: Thesis Objectives	19
Chapter 3: Scope	20
Chapter 4: Literature Review	22
Chapter 5: Active Magnetic Bearing Model	25

	vi
5.1	Introduction 25
5.2	Magnetic Circuit Model 25
5.3	Magnetic Bearing Force 29
5.4	Active Magnetic Bearing Control Considerations 31
5.5	Bearing Coil Model 37
5.6	Single Axis Single Bearing Model 39
5.7	Single Axis Dual Bearing Model 40
Chapter 6:	Active Magnetic Bearing Control System 44
6.1	Introduction 44
6.2	Current vs. Voltage Control 44
6.3	Linearization of Current Controlled AMB 46
6.3.1	Single Axis Single Bearing Force Linearization 48
6.3.2	Single Axis Dual Bearing Force Linearization 49
6.4	Digital Control Implementation 50
6.5	Decentralized Control 51
6.6	PID Position Control 53
6.7	Digital Control Aspects 53
6.8	Digital PID Algorithm 55
6.9	Discretization of AMB System Plant 58
6.10	Underlying “Inner” Current Control 62
Chapter 7:	Single Axis Single Bearing Test Setup 64
7.1	Purpose and Introduction 64
7.2	Test Setup Description 64
7.2.1	System Parameters 66
7.3	PID Controller Design for SASB Test Setup 67
7.4	SASB Simulink Model 70

	vii
7.5 Digital Filter	74
7.6 SASB Hardware Implementation	76
7.7 SASB Software Implementation	77
7.8 Control Performance	78
7.9 Integral Windup Prevention for PID Controller	81
7.10 Conclusion	83
Chapter 8: Stabilization Bearing Design	85
8.1 Introduction	85
8.2 Theory of Operation	85
8.3 Stabilization Bearing Lamination Geometry	87
8.3.1 Lamination Material	94
8.3.2 Number of Turns	95
8.3.3 Stabilization Bearing Coil Inductance and Resistance	97
8.4 Rotor Stability	98
8.5 Summary of SB Design Parameters	101
8.6 FEA Verification	101
8.7 Point Mass Simplification of Rotor	104
8.8 PID Controller Design for SB	105
8.9 SADB Simulink Model	106
8.10 SB Wiring and Orientation	112
8.11 SB Hardware Implementation	112
8.12 SB Software Implementation	114
8.13 Control Performance	114
8.13.1 Test Scenario One	116
8.13.2 Test Scenario Two	116
8.13.3 Test Scenario Results Summary	121

Chapter 9: Self-bearing Machine Control	122
9.1 Introduction	122
9.2 Theory of Operation	122
9.3 SLFBM Rotation Control	124
9.4 SLFBM Bearing Control	128
9.5 PID Controller Design for SLFBM	130
Chapter 10: Summary and Conclusions	132
10.1 Summary	132
10.2 Conclusions	135
Chapter 11: Recommendations for Future Work	137
References	139

List of Figures

1.1	Comparison of energy densities between energy storage solutions	6
1.2	Classification of Lorentz-type magnetic bearings. A=Active, P=Passive, from [10].	9
1.3	Classification of reluctance-type magnetic bearings. A=Active, P=Passive, from [10].	10
1.4	Simple AMB with position feedback, from [1]	11
1.5	Eight pole radial AMB for inner-rotor machine, from [15]	13
1.6	The complete UIFESS	14
1.7	The UIFESS with labeled components, vacuum system and shaft indexer are removed	16
1.8	The UIFESS stator hub with SB and SLFBM stator laminations	17
1.9	The UIFESS copper plate with embedded HTS pucks	17
5.1	Ferromagnetic core with air gap	26
5.2	Basic magnetic bearing, from [1]	28
5.3	Basic magnetic bearing forces	32
5.4	Bearing magnetic force vs. i when $x = x_0$, from [1]	33
5.5	Bearing magnetic force vs. x when $i = i_0$, from [1]	33
5.6	Bias point linearization of magnetic force vs. i , from [1]	35
5.7	Bias point linearization of magnetic force vs. x , from [1]	35
5.8	Typical magnetization curve for ferromagnetic material showing the re- gion which can be approximated linearly	36
5.9	Nonlinear SASB AMB model	40
5.10	SADB model	41
5.11	Nonlinear SADB AMB model	43

6.1	Current Controlled AMB	45
6.2	Voltage controlled AMB	45
6.3	Current controlled AMB with underlying current control loop	46
6.4	Decentralized control scheme for a conventional inner-rotor design, from [1]	52
6.5	Magnitude and phase of the frequency response for three types of PID controllers: continuous time without derivative filter, continuous time with derivative filter, and discrete time with derivative filter	57
6.6	Interaction between analog and digital portions of the AMB control system	59
6.7	AMB control system with ideal sampler and ZOH models	60
6.8	Equivalent z-domain system to Figure 6.7	62
6.9	Hysteresis current control algorithm	63
7.1	SASB test setup	65
7.2	High-level block diagram of SASB functionality	66
7.3	Pole-zero plot of the closed loop SASB system	70
7.4	PID position control subsystem from SASB Simulink model	72
7.5	Current control and coil dynamics subsystem from SASB Simulink model	72
7.6	Plant dynamics subsystem from SASB Simulink model	72
7.7	SASB air gap response to input step change	73
7.8	SASB coil current response to input step change	74
7.9	Zoomed in SASB coil current response to input step change showing cur- rent controller switching	75
7.10	Bode plots comparing PID controller frequency response with and without the additional digital filter	76
7.11	Top level SASB hardware diagram	77
7.12	Top level SASB software flow chart	79
7.13	Actual vs. simulated air gap response to step change	80
7.14	Actual vs. simulated coil current response to step change	81

7.15	Actual vs. simulated air gap response to step change without additional digital filter	82
7.16	Actual vs. simulated coil current response to step change without additional digital filter	82
7.17	PD and PID control strategy to prevent integral windup	83
8.1	Eight pole magnetic bearing cross section, from [33]	88
8.2	UIFESS inside-out eight pole magnetic bearing cross section	89
8.3	Geometric parameters of SB laminations	91
8.4	SB triangular winding	92
8.5	Force per SB pole pair over θ_1	94
8.6	B-H curve for M-36 silicon steel	95
8.7	Required bias current and number of turns vs. wire radius	96
8.8	UIFESS rotor assembly	98
8.9	Worst case scenario for rotor tilt	99
8.10	Design process for setting SB and spacer lengths	100
8.11	FEA results for SB with 2.6 A in all coils	102
8.12	Calculated and FEA magnetic force vs. current for each SB pole pair . .	103
8.13	Point mass representation of the rotor	104
8.14	PID position control subsystem from SADB Simulink model	108
8.15	Underlying bearing coil current control subsystem from SADB Simulink model	108
8.16	Bearing coil dynamics subsystem from SADB Simulink model	109
8.17	Plant dynamics subsystem from SADB Simulink model	109
8.18	SADB air gap response x_1 to input step change	110
8.19	SADB air gap response x_2 to input step change	110
8.20	SADB coil current response i_1 to input step change	111
8.21	SADB coil current response i_2 to input step change	112

8.22	SB wiring and position sensor orientation	113
8.23	Functional block diagram of SB hardware	115
8.24	Air gap g_x for test scenario 1	116
8.25	Bearing coil current D for test scenario 1	117
8.26	Bearing coil current B for test scenario 1	117
8.27	Air gap g_x for test scenario 2	118
8.28	Air gap g_y for test scenario 2	118
8.29	Bearing coil current D for test scenario 2	119
8.30	Bearing coil current B for test scenario 2	119
8.31	Bearing coil current A for test scenario 2	120
8.32	Bearing coil current C for test scenario 2	120
9.1	FRRM rotor and stator laminations	125
9.2	SLFBM drive control system	126
9.3	SLFBM current control, expanded from Figure 9.2	128
9.4	Depiction of stationary to rotational reference frame for the SLFBM . . .	129
9.5	SLFBM bearing function control algorithm	130

List of Tables

7.1	SASB test setup parameters	66
7.2	Poles and zeros of SASB plant	67
7.3	SASB PID position controller parameters	69
7.4	Poles and zeros of closed loop SASB system	71
7.5	Performance of SASB air gap response simulation	73
7.6	Filter parameters for 2nd order digital Butterworth filter with 1.5 kHz cutoff frequency	75
8.1	SB design constraints	86
8.2	Calculated SB lamination design parameters	94
8.3	Rotor stability design parameters and constraints	101
8.4	SB parameters	101
8.5	SB PID position controller parameters and closed loop performance . . .	106
8.6	Poles and zeros of closed loop SB system	106
8.7	Performance of SADB air gap response simulation	111
8.8	SB pole pair bearing designations	114
9.1	Coil states during operation	127
9.2	SLFBM bearing control parameters	131

List of Abbreviations

ADC	Analog to Digital Converter
AMB	Active Magnetic Bearing
AWG	American Wire Gauge
DAC	Digital to Analog Converter
DOF	Degree of Freedom
FEA	Finite Element Analysis
FEMM	Finite Element Method Magnetics (computer program)
FES	Flywheel Energy Storage
FRRM	Field Regulated Reluctance Machine
HTS	High Temperature Superconductor
IDE	Integrated Development Environment
MCU	Microcontroller Unit
MIMO	Multiple Input Multiple Output
PD	Proportional Derivative
PID	Proportional Integral Derivative
SADB	Single Axis Dual Bearing
SASB	Single Axis Single Bearing
SB	Stabilization Bearing
SISO	Single Input Single Output
SLFBM	Self-Bearing Machine
UIFESS	University of Idaho's Flywheel Energy Storage System
ZOH	Zero Order Hold

Chapter 1

Introduction

Energy storage is an essential aspect of countless electrical and mechanical systems. Energy storage solutions are found in everything from flashlights to spacecraft and provide energy when sources of generation are not available, feasible, or sufficient. In many applications, energy is stored with the intent of providing electrical energy at a later point in time. Batteries, for instance, provide electrical energy by converting energy stored chemically.

Like a battery, a flywheel energy storage (FES) system is a storage device which can provide electrical energy on demand. Unlike a battery, however, a FES system stores energy mechanically in the inertia of a rotating mass. FES systems are a promising energy storage technology with a number of advantageous characteristics. With proper advancement of FES system technology, FES systems could become the best option for energy storage in a wide range of applications.

The University of Idaho is investigating FES systems with the goal of providing NASA a viable energy storage solution for a permanent lunar colony. A lunar colony would require continuous electrical power to run scientific instruments and life support systems. Although solar or nuclear power can provide the source of energy generation, these methods cannot provide continuous electrical power. In addition, sources of generation may be unable to meet power requirements for instances of peak demand. To mitigate these problems, a FES system could be employed to store excess energy for instances when energy from generation is unavailable or insufficient.

Electrochemical batteries are the current standard for energy storage in space. However, FES systems have the potential to offer a substantial improvement over battery systems in terms of lifetime and energy density. FES systems have an expected lifetime of over 20 years with essentially an infinite number of charge/discharge cycles. In addition,

energy densities of up to 2700 Wh/kg are theoretically possible with high speed carbon nanotube rotors.

Active magnetic bearings (AMBs) enable FES systems to realize their full potential in lifetime and energy density. An AMB is a frictionless bearing that provides support by means of magnetic forces. Without friction, the flywheel is free to rotate at the high speeds necessary to achieve a high energy density. The absence of physical contact eliminates mechanical wear, drastically reducing the need for maintenance.

AMBs rely on feedback from a control loop to “actively” adjust the magnetic forces required to stabilize the flywheel. Incident disturbance forces on the flywheel are attenuated in real time by the AMB control system to ensure the flywheel remains fully suspended. Although AMBs are inherently more complex than their contact bearing counterparts, energy losses are 5 to 20 times less at high rotational speeds [1].

This thesis describes the design and initial testing of the AMB systems employed on the University of Idaho flywheel energy storage system (UIFESS), an experimental low-speed FES system designed and built at the University of Idaho. The main objective of this work is to develop the groundwork for the UIFESS AMB systems. In turn, future UIFESS researchers will be able to build on this work to realize state of the art AMB systems capable of controlling high speed flywheels.

The following two sections in this chapter provide more details regarding the advantages and applications of FES systems and magnetic bearings. The final section in this chapter outlines the various systems of the UIFESS, including the UIFESS AMB systems.

1.1 Flywheel Energy Storage System

A flywheel is a mechanical device that stores energy in the inertia of its own rotating mass. A flywheel energy storage (FES) system uses a flywheel as an energy storage medium. In its basic form, a FES system consists of a flywheel, an electromagnetic

machine, and power electronics. The input energy to a FES system is in the form of electrical energy, which drives the electromagnetic machine as a motor to rotate the flywheel. This process stores the input electrical energy as mechanical energy in the rotating flywheel. To extract the stored energy, the electromagnetic machine is operated as a generator, relying on the inertia of the rotating flywheel to act as a prime mover.

The power electronics are responsible for controlling the direction of energy flow by operating the electromagnetic machine as either a motor or generator, depending on whether energy is actively being stored or extracted. During periods of energy storage, the electromagnetic machine is placed in an idle state. Minimizing the energy loss during the idling (storage), is especially important to achieve a high storage efficiency from the FES system.

In addition, to achieve high efficiency and high speeds, FES systems must overcome the primary contributors to machine losses: windage and friction. Placing the flywheel within a vacuum containment vessel and employing non-contact bearings drastically reduces the losses and speed limitations due to windage and friction, respectively.

The amount of energy stored within the rotating flywheel is proportional to flywheel moment of inertia and the square of the rotational speed:

$$E_k = \frac{1}{2}I\omega^2 \quad (1.1)$$

where E_k is the stored kinetic energy, I is the flywheel moment of inertia, and ω is the angular velocity of the flywheel [2]. The moment of inertia is dependent upon the geometric shape of the flywheel as well as the flywheel's mass. Noting the square dependency of the kinetic energy on angular velocity, the importance of achieving high rotational speeds is apparent. Doubling the flywheel's rotational speed will quadruple the stored energy. Due to this fact, development of materials capable of high rotational speeds play a major role in FES system research and design.

Pure mechanical flywheels have existed since the 11th century, where their resistance to changes in rotational speed helped stabilize the speed of rotating shafts in various forms of machinery [3]. Thanks to improvements in flywheel material, power electronics, and magnetic bearings in the 20th century, flywheel energy storage systems gained attention as a viable means of electrical energy storage. In the 1970's, FES systems were proposed for use in electric vehicles and stationary power backup [2].

Today, the main application areas for FES systems include:

- **Terrestrial Power Grid.** FES systems can be employed to mitigate various power quality issues including frequency regulation and voltage sag compensation for the power grid [4].
- **Renewable Energy Systems.** Power production from renewable energy sources such as wind and solar varies significantly on an hourly, daily, and seasonal basis. The integration of FES systems into a renewable energy system will allow excess generation to be stored and provide power during periods of insufficient generation [5].
- **Uninterruptable Power Systems (UPS).** FES systems can provide short term backup power to critical systems in the event of power outages. Today, UPS FES systems are commercially available.
- **Aerospace.** In addition to general energy storage for a lunar colony as previously mentioned. NASA is investigating using FES systems to replace battery systems in satellites and even the International Space Station [6]. In addition, FES systems may offer a novel method to combine attitude control (by replacing momentum wheels) and energy storage (by replacing batteries) to reduce the overall mass of the combined systems for satellites and spacecraft [6].

1.1.1 Advantages of FES Systems

FES systems are one of many energy storage solutions along with batteries, fuel cells, and super capacitors, amongst others. Although the current state of FES system technology offers a number of important advantages over other energy storage solutions, FES systems are not the clear favorite. However, proper advancement of FES system technology could potentially make FES systems the top choice among energy storage solutions for both terrestrial and space applications.

Although a detailed comparison of energy storage solutions is beyond the scope of this thesis (and can be found in [5, 7, 8]), FES systems offer the following advantages:

- Expected lifetime of over 20 years [7, 9].
- No capacity degradation due to level of charge, depth of discharge, or number of charge-discharge cycles [2, 7].
- High turn around efficiency on the order of 85-95% [5, 7, 9].
- High power density on the order of 5000 W/kg [7, 8].
- Environmentally friendly materials, low environmental impact [2]. No environmental concerns for disposal [9].
- State of charge is easily determined from knowledge of rotational speed [2].
- Quick response time for power demands [8].
- Short recharge time [2, 5].
- Potential for extremely high energy density. FES systems utilizing high speed carbon nanotube flywheels are theoretically predicted to have an energy density of 2700 Wh/kg [6]. To place this in perspective, Figure 1.1 compares the theoretical

carbon nanotube FES system energy density with that of current energy storage systems and other theoretical energy storage capabilities.

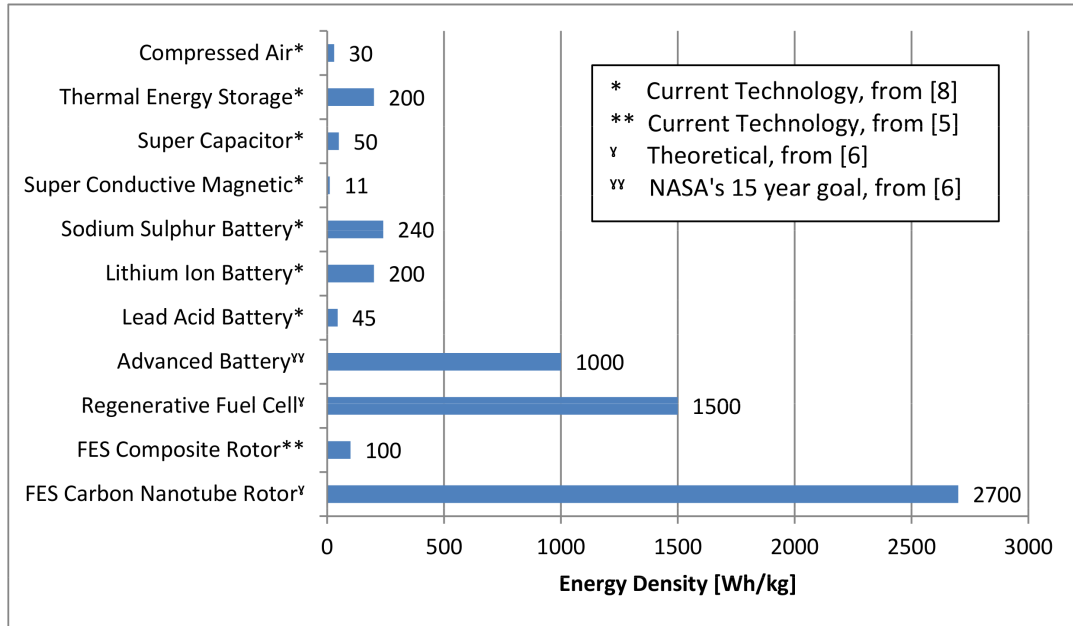


Figure 1.1: Comparison of energy densities between energy storage solutions

One of the largest drivers of FES research, especially in space applications, is apparent in Figure 1.1: the potential for superior energy density in comparison to other energy storage solutions. However, to achieve the 2700 Wh/kg mark, the flywheel must achieve extremely high rotational speeds.

Although the University of Idaho (UI) is currently developing a low-speed flywheel, the eventual research goal is the development of high-speed flywheels. By initially developing a low speed flywheel, the UI flywheel research team will gain valuable knowledge and experience in FES systems to help tackle the technical difficulties of a high speed design. Once the low-speed flywheel is complete, work will begin on a high-speed flywheel that is specifically designed for the lunar surface.

1.2 Magnetic Bearings

Magnetic bearings are non-contact bearings that employ magnetic forces to provide frictionless suspension for moving machinery. The two main areas of industrial application for magnetic bearings are rotating machinery and transportation.

Perhaps the most familiar application of magnetic bearings is MAGLEV trains, for which the first patent appeared as early as 1937. These trains, which employ magnetic bearings to levitate the train's cabin above the track, are capable of extremely high speeds of over 300 mph due to zero friction with the track. When applied to rotating machinery, magnetic bearings look to replace conventional mechanical bearings such as ball or journal bearings by offering lower losses and higher rotational speeds.

1.2.1 Magnetic Bearing Classification

The implementation of a magnetic bearing can take on various forms depending on how the magnetic field is generated and used to create force. A classification scheme has been proposed in [10], where magnetic bearing implementations are divided into two main types. As in [10], this thesis will use the term “levitation” to refer to complete suspension of an object with zero physical contact and a full six degrees of freedom.

From [10], the distinction between the two main types of magnetic bearings is taken from how the magnetic force is calculated. Magnetic bearings that derive their force from (1.2) are termed Lorentz-force type [10].

$$\mathbf{f} = \mathbf{i} \times \mathbf{B} \tag{1.2}$$

Equation (1.2) is taken from the general equation for Lorentz force:

$$\mathbf{f} = Q(\mathbf{E} + \mathbf{v} \times \mathbf{B}) \tag{1.3}$$

Since the energy density of feasible electrical fields in macroscopic technical arrangements is usually around 100 times smaller than that of magnetic fields, the electrostatic term \mathbf{E} in (1.3) is not considered [1]. The product of charge Q and velocity \mathbf{v} equates to current \mathbf{i} , and (1.3) becomes (1.2). Equation (1.2) is the familiar equation describing force on a current carrying conductor. The Lorentz force in this type of magnetic bearing acts perpendicular to the magnetic flux lines and thus along the air gap.

The other main type of magnetic bearing is the reluctance-force type [10]. For this type, the force exists at the surface of media of different relative permeability, such as iron and air [10]. Thus, the force acts across the air gap and parallel to the magnetic flux lines between the media. Reluctance-force type magnetic bearings derive their force from the principle of virtual displacement:

$$f = \frac{\partial W}{\partial s} \quad (1.4)$$

where W is the field energy and ds is the virtual displacement of the supported body. The reluctance force acts in such a way as to reduce the overall reluctance of the magnetic circuit, i.e. decreasing the air gap distance between two magnetic materials.

Both types of magnetic bearings are utilized as rotor bearings. Lorentz-type magnetic bearings are mainly used in induction and synchronous self-bearing machines. Self-bearing machines integrate the action of a magnetic bearing within the machine itself, providing both rotation and levitation to the rotor. There are various types of self-bearing machines and their implementation is accomplished by appropriate control and design of the machine. Figure 1.2 outlines the classification of Lorentz-type bearings.

The vast majority of magnetic bearings used in industry today are reluctance-force magnetic bearings. When compared on the basis of a standalone magnetic bearing system, Lorentz-type bearings are more difficult to realize for rotating machinery than reluctance-type magnetic bearings [10]. However, it is difficult to designate a clear

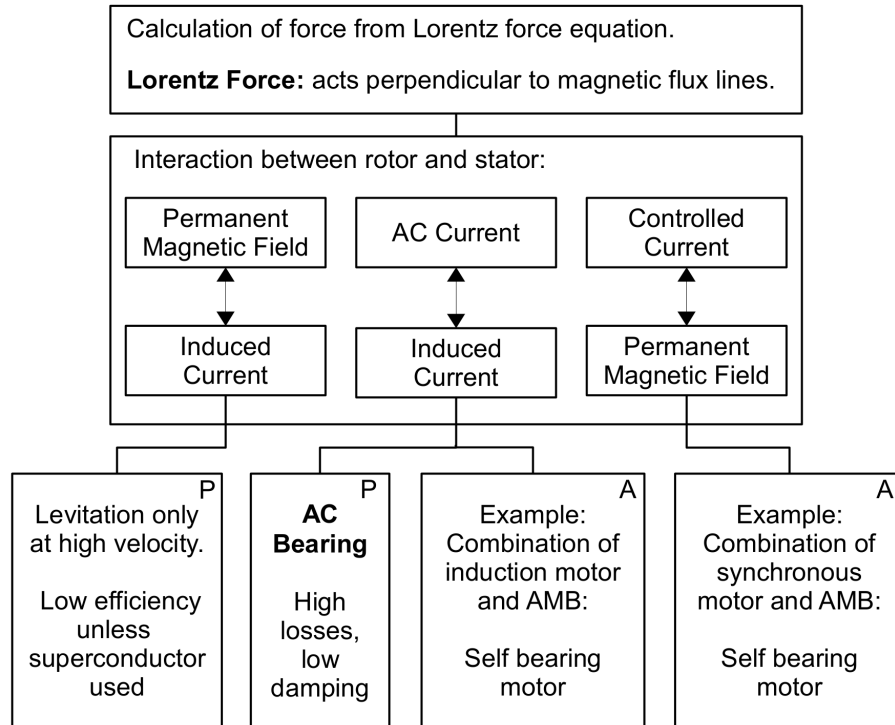


Figure 1.2: Classification of Lorentz-type magnetic bearings. A=Active, P=Passive, from [10].

favorite between the two types, as the ultimate decision is mainly determined by the application at hand [10].

Another essential classification of magnetic bearings is based upon levitation stability. The qualifier “active” describes magnetic bearing systems that require dynamic sensor feedback to achieve stable levitation. Conversely, the qualifier “passive” designates magnetic bearing systems that do not require dynamic sensor feedback for stable levitation. Figures 1.2 and 1.3 further classify Lorentz-type and reluctance-type magnetic bearings, respectively, and provide a basic summary of each magnetic bearing solution. These figures also designate the magnet bearing solution as either “active” or “passive” based on the definitions previously described.

The reluctance-type magnetic bearing classification can be broken down into four types which are described in Figure 1.3. The most common type of magnetic bearing utilized in industry is type 1. The typical implementation of a type 1 magnetic bearing

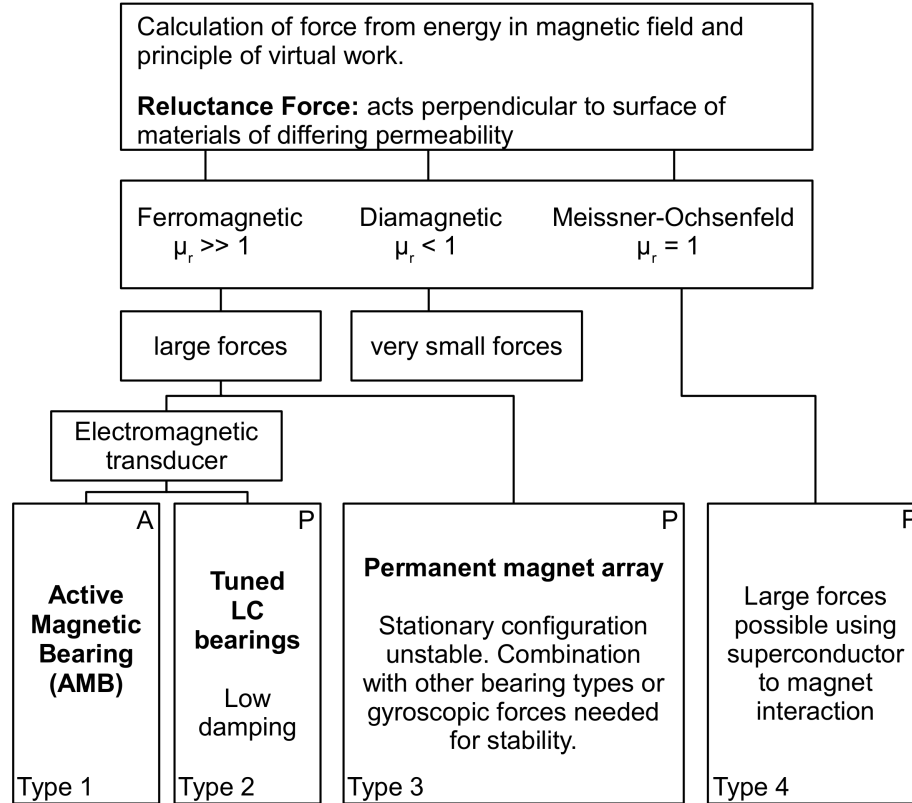


Figure 1.3: Classification of reluctance-type magnetic bearings. A=Active, P=Passive, from [10].

consists of an electromagnet with a time varying current. In turn, the current in the electromagnet is manipulated with respect to a feedback mechanism. Figure 1.4 depicts this configuration when feedback is provided by a distance sensor. For this work, active magnetic bearing (AMB) will refer to the type 1 magnetic bearing implementation in Figure 1.4.

1.2.2 Earnshaw's Theorem and Permanent Magnet Suspension

It is important to note that stable levitation is not possible for a non-rotating object solely supported by permanent magnets. In 1842 Samuel Earnshaw developed a theorem proving that a collection of point charges cannot maintain a stationary equilibrium configuration based solely upon the electrostatic forces produced by the point charges [11]. This theorem can be applied to a set of permanent magnets attempting to levi-

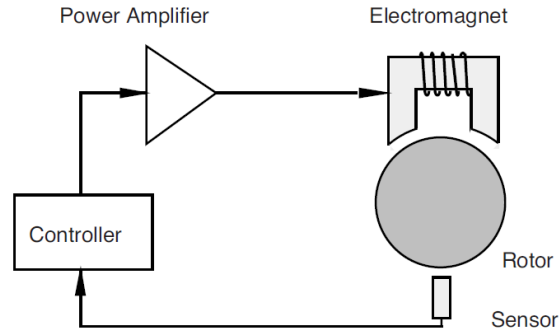


Figure 1.4: Simple AMB with position feedback, from [1]

tate a non-rotating object. For this setup, the theorem proves that stable suspension is physically unrealizable, with instability occurring in at least one degree of freedom for any permanent magnet configuration [1]. Although levitation of a rotating object is possible within a permanent magnet configuration, stability is only achieved under certain conditions over a limited rotational speed range.

Therefore, to achieve stable suspension over a range of rotational speeds, levitation through permanent magnets alone is not possible. Although permanent magnets can play a partial role in levitation of a rotating object, an active magnetic bearing or superconductor-to-magnet interaction must be employed to provide stable levitation over a range of rotational speeds.

1.2.3 AMB Advantages and Application to FES Systems

The characteristics of AMBs provide many advantages over conventional contact bearings and passive magnet bearing systems. The following points describe the advantages and additional features of AMBs along with the benefits they offer FES systems:

- **Active imbalance attenuation.** Incident forces and vibrations are actively damped from the system, this is especially important when the rotor reaches bending critical speeds (also referred to as bending modes). To store more energy, flywheels are rotated as fast as material properties allow. Desired flywheel

rotational speeds for storage may be greater than one or more bending critical speeds.

- **Adjustable stiffness and damping coefficients.** A digital control system can dynamically change the AMB's stiffness, damping, or overall control law. The AMB's control law can be scheduled to change at bending critical speeds to minimize the resulting vibrations. Again, this provides an important advantage to flywheels, as their rotational speed range may pass one or more bending critical speeds. In addition, control laws within the digital control system can be adapted and tuned while the machine (or flywheel) is on-line [1].
- **Load independent positioning.** AMBs can adjust rotor position in response to constant loads or rotor imbalances; in turn, the air gap can be maintained at its nominal value. This characteristic is not possible in conventional bearings. AMBs can allow the rotor to rotate about its principle axis of inertia, thus avoiding vibrations due to the imbalance [12, 13]. Vibrations due to the high speeds of flywheels could otherwise be damaging if transferred to the machine founding through conventional bearings.
- **Low loss.** AMB losses at high speeds are 5 to 20 times less than conventional ball or journal bearings, this results in better overall efficiency for the FES system [1].
- **Allows very high speed rotation.** Rotational speed of the rotor is limited by the material strength of the rotor and not by any characteristic of the AMB [1]. In reference to FES systems, it is seen from (1.1) that energy storage within a flywheel increases quadratically with respect to rotational speed. Thus, AMBs will not limit the FES system's ability to store energy as higher rotational speeds are reached. In industry, speeds of up to 30,000 RPM have been reached in small turbo machinery. In laboratory experiments, a NASA flywheel has achieved speeds of up to 60,000 RPM [14] utilizing magnetic bearings.

- **Zero wear.** Due to physical contact with the rotor, conventional contact bearings release wear particles and must eventually be replaced or repaired. Without physical contact, AMBs have essentially infinite lifetime. This is a welcome characteristic to FES systems, which are designed to be highly dependable with lifetimes of over 20 years. Wear particles from mechanical bearings degrade vacuum environments. Since FES systems operate within a vacuum environment to remove losses due to windage, AMBs become the preferred choice.
- **Operation at harsh temperatures.** AMBs require no lubrication and can be designed to suffer harsh temperatures from $-270\text{ }^{\circ}\text{C}$ up to $550\text{ }^{\circ}\text{C}$ [1]. Conventional contact bearings are temperature limited by their lubrication and material makeup. Depending upon the specific design, the vacuum environment inside a FES system may limit the ability to regulate temperatures. Therefore, the wide temperature range of AMBs is a welcome advantage for FES systems.

Figure 1.5 depicts a radial eight pole AMB and rotor journal for an inner-rotor rotary machine. The eight pole design is common in industry, as will be discussed later in this thesis.



Figure 1.5: Eight pole radial AMB for inner-rotor machine, from [15]

1.3 University of Idaho's FES system design

The UIFESS is an experimental FES system designed and built at the University of Idaho. The UIFESS was designed as a low speed FES system. The system was designed for an operating speed of 1800 RPM, although the design may be able to achieve higher speeds of up to 5000 RPM [16].

The UIFESS flywheel is integrated within the rotor. In this thesis, the terms “flywheel” and “rotor” refer to the same object, the rotating portion of the UIFESS. The UIFESS is an outer-rotor design with the stator located on the inside of the rotor. The outer-rotor (also known as inside-out) design allows for a higher rotational speed and energy density. The complete UIFESS is shown in Figure 1.6.

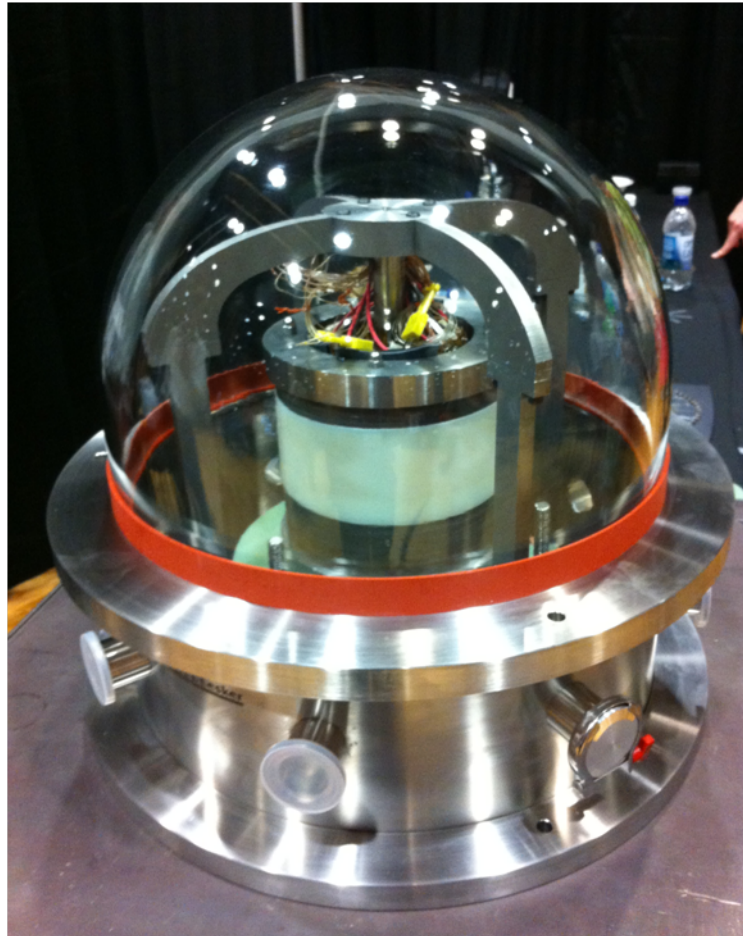


Figure 1.6: The complete UIFESS

The entire FES system is encapsulated within a vacuum chamber. To drastically reduce windage losses, the vacuum chamber is evacuated to a pressure of about 10^{-4} Torr. Feedthroughs in the vacuum chamber collar provide access for electrical and liquid cooling connections to the internal FES system.

To eliminate frictional losses due to conventional bearings, the UIFESS utilizes magnetic bearings to completely levitate the UIFESS rotor without any physical contact. Magnetic bearings are responsible for controlling five degrees of freedom of the levitated rotor. The field regulated reluctance machine (FRRM) provides torque to the flywheel about the remaining degree of freedom. The UIFESS design adapts the functionality of the FRRM to provide corrective radial forces in addition to providing the torque necessary to rotate the flywheel. Therefore, the FRRM is referred to as the self-bearing machine (SLFBM) since the function of an AMB has been integrated within the machine. The stabilization bearing (SB), on the other hand, is a dedicated AMB system that only provides corrective radial forces to the flywheel.

The UIFESS, depicted without the vacuum chamber and shaft indexer, is shown in Figure 1.7. The major components of the UIFESS are shown in Figure 1.7 along with the coordinate system used to describe the UIFESS. The z axis of the UIFESS coordinate system is defined as parallel to the stator hub.

The SB and SLFBM prevent rotor tilt (rotation about the x and y axes) and translation of the rotor within the x-y plane. The SB and SLFBM are active magnetic bearing systems that will dynamically react to imbalance forces to maintain the radial air gap using measurements provided by radial position sensors. The UIFESS center hub with SB and SLFBM stator laminations is shown in Figure 1.8.

Support in the z direction is provided by a high temperature superconducting (HTS) bearing. The HTS bearing is a passive magnetic bearing system that provides a large suspension force through a permanent magnet to superconductor interaction. The permanent magnets are embedded into the bottom of the rotor in a Halbach array

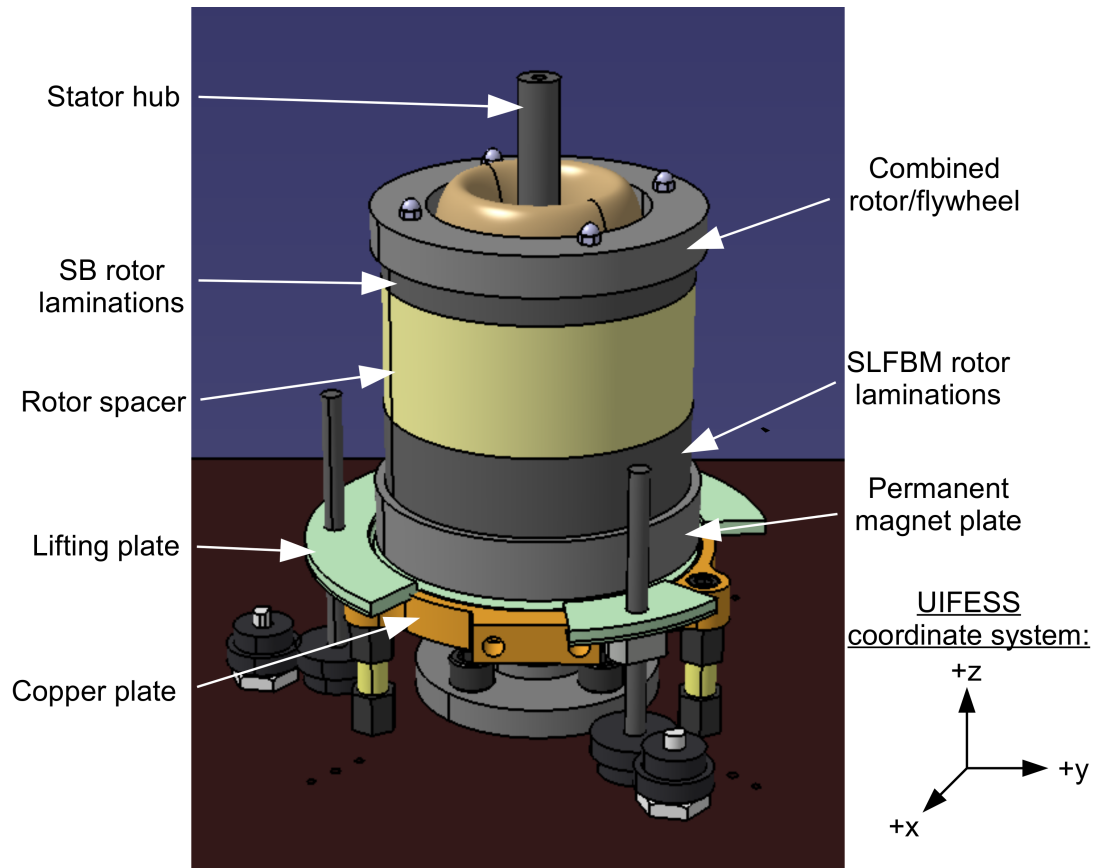


Figure 1.7: The UIFESS with labeled components, vacuum system and shaft indexer are removed

configuration. A Halbach array configuration focuses the permanent magnets' magnetic field in the direction of the HTS, increasing the magnetic suspension force.

To provide suspension, the HTS must be cooled to below 90 K. The HTS cooling is accomplished using a liquid nitrogen cooling system. The liquid nitrogen is pumped into a small reservoir within a copper plate. The HTS "pucks" are set into the top of the copper plate to maximize cooling from the liquid nitrogen without releasing the liquid nitrogen into the vacuum containment. The copper plate with the embedded HTS pucks is shown in Figure 1.9.

To help remove heat from the stator due to copper and iron losses, a water cooling system is utilized. Chilled water is pumped into the center of the stator column, which features two internal channels to allow water flow in and out.

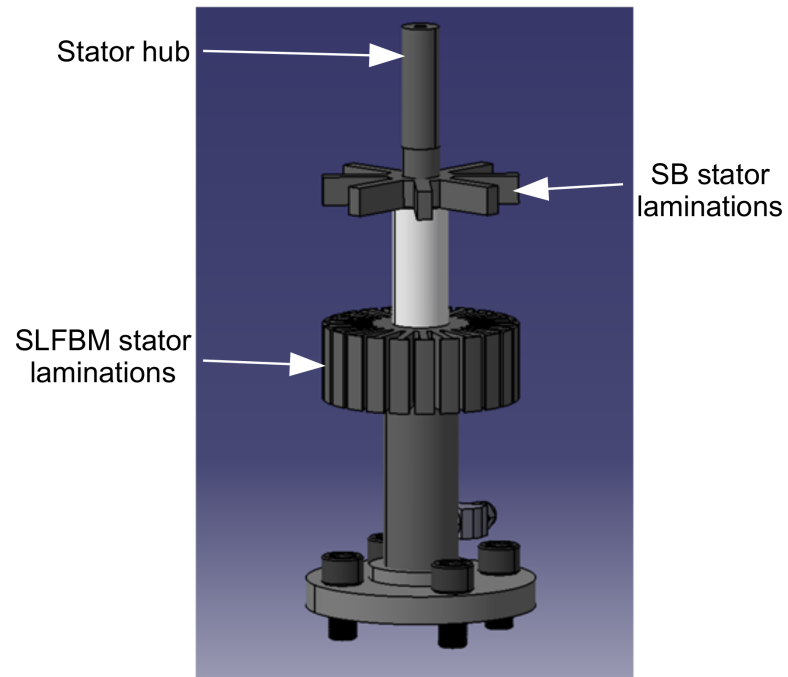


Figure 1.8: The UIFESS stator hub with SB and SLFBM stator laminations

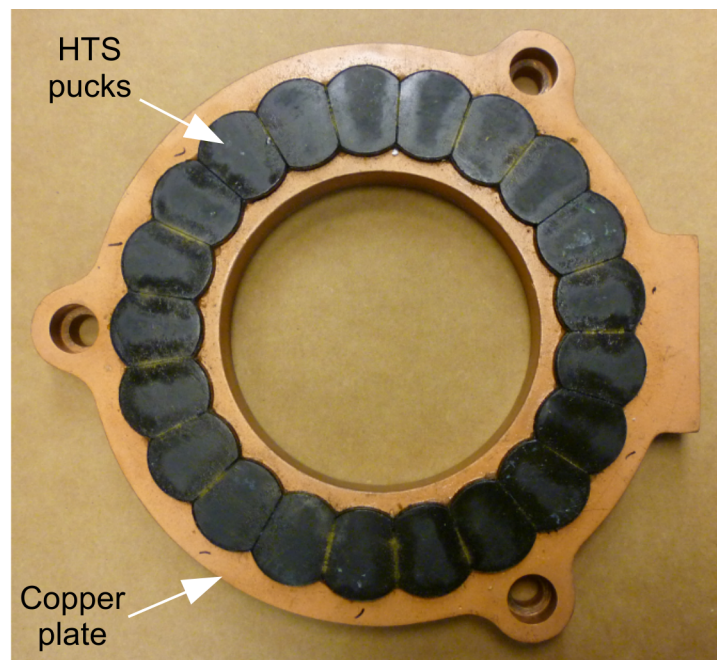


Figure 1.9: The UIFESS copper plate with embedded HTS pucks

The lifting plate supports the rotor until the HTS pucks are properly cooled and the SB and SLFBM magnetic bearings are energized. The lifting plate also serves to protect the HTS from the weight of the rotor in the event of a levitation failure.

Chapter 2

Thesis Objectives

The first and foremost objective of this work is to lay a foundation of knowledge for the implementation of active magnetic bearings (AMBs) on the UIFESS. This foundation of knowledge is given in the form of AMB models, AMB simulations, and initial testing results for the SB.

Implementation of an active magnetic bearing control system is a non-trivial task. A large research community is actively investigating many different aspects of its development and application. State of the art AMB control involves substantial familiarity with advanced modeling and control techniques. In order to utilize advanced techniques, however, a firm understanding of the fundamental AMB modeling and control concepts is required. This thesis aims to develop this fundamental understanding so that future UIFESS researchers may utilize state of the art control techniques to achieve very high rotational speeds for the UIFESS.

The second objective of this work is to document and report on the physical design of the stabilization bearing, an integral component of the UIFESS. Future researchers on the UIFESS project will benefit from this documentation as modeling and control of the UIFESS is improved or adapted.

The third objective of this work is to describe the operation of the self-bearing FRRM. The next major hurdle for the UIFESS is achieving both rotation and bearing control of the self-bearing FRRM. The work supporting this objective will aid the next team of UIFESS researchers in overcoming this hurdle.

Chapter 3

Scope

The work described in this thesis was performed during the fall of 2012, throughout the entire year of 2013, and the first months of 2014. During this time-frame, two other researchers were conducting work on the UIFESS that is directly related to work in this thesis. Work from the other two researchers is available in the form of theses by Kevin Ramus and Bridget Wimer, given in [16] and [17], respectively.

Collaboration between this work and work done by Ramus and Wimer was frequent and interconnected. Therefore, the following lists serve to outline and clarify the division of research performed between this work, [16], and [17]:

In this work:

- Description of current controlled AMB model
- AMB control system and control software design
- Stabilization bearing design and implementation
- Initial development of self-bearing machine control algorithms

By Ramus, [16]:

- UIFESS sensor and vacuum system selection
- Power amplifier design
- Signal conditioning and PCB design
- Prediction of UIFESS speed capabilities

By Wimer, [17]:

- FRRM design

- Determination of FRRM current and position stiffness values
- Modeling and simulation of UIFESS rotor dynamics

Chapter 4

Literature Review

Research into active magnetic bearing control began as early as 1946 with [18], which successfully levitated small steel balls (about 1 mm in diameter) entirely supported by active magnetic forces utilizing a simple control loop. The steel balls were rotated freely up to 300 kHz (18 million RPM) until they burst to investigate their material strength under centrifugal load.

The late 1970's and early 1980's saw a surge of research into the fundamentals of magnetic bearing technology and the new possibilities offered by magnetic bearings in rotating machinery [19]. The increase in research popularity surrounding magnetic bearings culminated with the establishment of the International Symposium on Magnetic Bearings (ISMB) in 1988. Thorough state of the art surveys on various aspects of magnetic bearing technology are given by the ISMB, and in its proceedings [1, 20].

An important component of the magnetic bearing research in the 1980's is the transition from analog to digitally controlled AMBs. Digital control offers greater flexibility over analog control [21]. However, digital control of AMB systems require short sampling times and fast digital processing speeds [22]. The performance capabilities of digital control technology in the 1980's demanded a distributive approach to the digital control system processing. Therefore, a decentralized control method is utilized to implement simplified digital control algorithms within a set of decoupled microcontrollers. The decentralized control method is accomplished through simplification of the AMB rotor dynamics into multiple low-order SISO (single input single output) plants. In turn, the low-order plants can be controlled by an appropriate low-order controller, reducing the processing requirements of the microcontroller [19].

The initial work in decentralized control is given in [22], which develops a method of designing decentralized PD controllers for rigid rotors. The main result from [22] shows that a decentralized control method is possible in most AMB applications without any

significant effect on system performance when compared to an optimal centralized *state feedback* method.

Although the processing performance of digital control technology has drastically improved, allowing complex control algorithms to be implemented within a centralized microcontroller, the decentralized approach is still commonly used due to its simplicity and satisfying performance in certain applications. In addition, the decentralized control scheme lends itself to the utilization of the well known proportional-derivative (PD) and proportional-integral-derivative (PID) controller topologies.

Two decades ago, over 90% of AMB systems were based on decentralized PID control [21]. Today, the majority of industrial AMB systems are still controlled by PID-type controllers [23]. Experimental flywheel energy storage systems utilizing decentralized PID-type controllers are given in [24] and [25].

Research in decentralized PID controllers for AMB systems have centered around tuning and controller gain optimization to achieve high levels of robustness. Work in [26] compares the performance of various PID tuning methods and evaluates the resulting robustness of each design. A rule-based approach for selection of PID parameters has been suggested in [27] to provide adequate controller robustness and stability. Modern robust control methodologies, such as \mathcal{H}_∞ control theory have also been applied to PID parameter design as investigated in [28].

The combination of gyroscopic effects and non-collocation at high rotor speeds poses stability issues for decentralized PID control and is described in detail in [1]. To solve this issue, a parallel/conical decomposition control method is adopted [1]. The parallel/conical decomposition control relies on parallel and conical mode decomposition of the rotor dynamics to allow design of SISO controllers such as PID. The trade-off for the increased performance of parallel/conical decomposition control is that pure decentralization is lost. A PID controller design optimization procedure for parallel/conical decomposition control is given in [23].

State of the art AMB control involves modeling the rotor as a flexible body. High rotor speeds will excite bending modes that must be controlled by the AMB control system. The difficulty of controlling the flexible modes often demands a more complicated multiple-input multiple-output (MIMO) approach utilizing modern robust controller design techniques such as \mathcal{H}_∞ and μ -synthesis [1]. However, as the UIFESS is a low speed design, an in-depth review of flexible control is beyond the scope of this thesis. As a start, however, modern robust control design has been applied to FES systems and reported in [29, 30].

A topic surrounding AMB research worth mentioning in passing is self-sensing AMBs. Self-sensing AMBs extract information regarding the air gap from the measurement of the bearing coil current. This approach removes the need for a dedicated position sensor, reducing cost and hardware complexity. A description of self-sensing AMBs is given in [1]. Although significant technical hurdles still exist for self-sensing AMBs in terms of robustness and implementation, these hurdles are steadily diminishing. Self-sensing AMBs have successfully suspended rotor speeds of 52000 RPM in a laboratory setting [31].

Another topic investigated in this thesis is the physical bearing design of the AMB. The 8-pole bearing design is the most prevalent due to its ability to be easily controlled as a consequence of its symmetric design. Current research work focuses on designing geometrically efficient magnetic bearings capable of large forces while minimizing the overall bearing size and material requirements.

Work in [32] introduces a geometric efficiency coefficient to evaluate the maximum bearing force with respect to the geometric dimensions of the bearing. Work in [33] simultaneously considers the geometric bearing design with the AMB power amplifier and controller design to create a nonlinear constrained optimization problem. A genetic algorithm in [33] is then used as an optimization tool to find the best overall AMB design in terms of bearing stiffness, damping, and volume.

Chapter 5

Active Magnetic Bearing Model

5.1 Introduction

This chapter develops two different single degree of freedom (DOF) AMB models. These AMB models are referred to as the single-axis single-bearing (SASB) and single-axis dual-bearing (SADB) models, and will be referenced throughout this thesis.

The SASB model describes the force of one magnetic bearing against the force of gravity. The SASB model was realized in hardware in Chapter 7 as the SASB test setup. The SASB test setup exhibits many of the same design challenges in applying the SADB model to the Stabilization Bearing (SB) and the Self-Bearing Machine (SLFBM) systems. In turn, the SASB test setup was utilized to develop familiarity with the necessary hardware and software requirements for the SB and SLFBM systems in a simplified setting.

The SADB model describes a system of two opposing bearings which can provide corrective forces in both directions along a single axis. The SADB model provides the basis for designing the decentralized controllers for the SB and SLFBM systems.

Sections 5.2 through 5.5 develop ideas and equations that are common to both SASB and SADB models. Sections 5.6 and 5.7 present the full SASB and SADB system models separately.

5.2 Magnetic Circuit Model

Figure 5.1 depicts a simple magnetic circuit created by a wire wrapped around a ferromagnetic core with an air gap. The basic equation governing the production of a

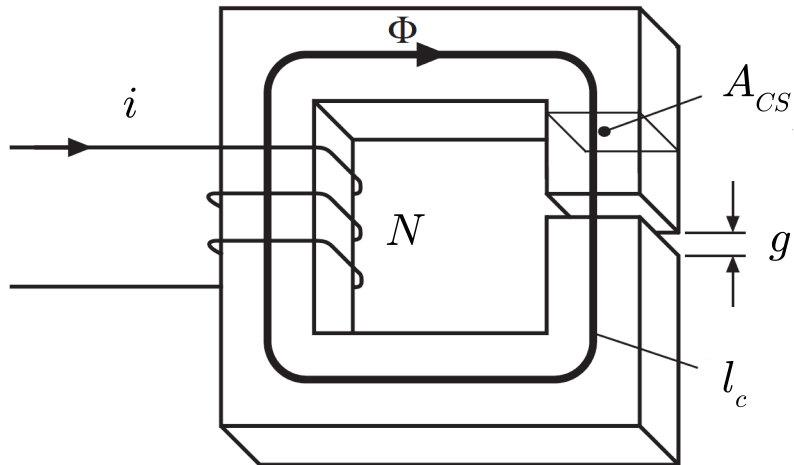


Figure 5.1: Ferromagnetic core with air gap

magnetic field by a current is Ampere's Law:

$$\oint \mathbf{H} \cdot d\mathbf{l} = i_{encl} \quad (5.1)$$

where \mathbf{H} is the magnetic field intensity produced by the current i_{encl} contained within the surface enclosed by the path \mathbf{l} . Applying Ampere's Law to Figure 5.1, the path \mathbf{l} from equation (5.1) is depicted as \mathbf{l}_c . The total enclosed current bounded by the closed path \mathbf{l}_c is Ni , where N is the number of turns in the coil of wire and i is the coil current. Therefore, Ampere's Law for Figure 5.1 gives:

$$\oint \mathbf{H} \cdot d\mathbf{l}_c = Ni \quad (5.2)$$

Neglecting the nonlinear characteristics of ferromagnetic material such as magnetic saturation and magnetic hysteresis, a linear relationship between the magnetic field intensity \mathbf{H} and magnetic field density \mathbf{B} is assumed and defined as:

$$\mathbf{B} = \mu_0 \mu_r \mathbf{H} \quad (5.3)$$

and in magnitude:

$$B = \mu_0 \mu_r H \quad (5.4)$$

where μ_0 is the permeability of free space and μ_r is the relative permeability of the ferromagnetic material.

Since μ_r is much greater than the relative permeability of air, this development assumes all of the magnetic flux produced by the coil is linked along the closed path \mathbf{l}_c . Fringing flux for the geometry in Figure 5.1 is assumed to be negligible. Therefore, no leakage flux and no fringing flux is assumed. The cross sectional area of the ferromagnetic core A_{fe} and cross sectional area of the air gap A_g are equal to A_{CS} in Figure 5.1. These assumptions create the following relationships:

$$\Phi = B_{fe} A_{fe} = B_g A_g \quad (5.5)$$

$$A_{fe} = A_g = A_{CS} \quad (5.6)$$

$$B = B_{fe} = B_g \quad (5.7)$$

where Φ is the magnetic flux within the magnetic circuit, B_{fe} is the magnetic flux density within the ferromagnetic core, and B_g is the magnetic flux density within the air gap.

Beginning from the application of Ampere's Law in equation (5.2) and substituting in (5.4) and (5.7), the magnetic flux density B of Figure 5.1 follows:

$$Ni = \oint \mathbf{H} \cdot d\mathbf{l}_c = \oint_{fe} \mathbf{H} \cdot d\mathbf{l}_{fe} + \oint_{airgap} \mathbf{H} \cdot d\mathbf{g} \quad (5.8)$$

$$Ni = Hl_{fe} + Hg = \frac{B_{fe}}{\mu_0 \mu_r} l_{fe} + \frac{B_g}{\mu_0} g \quad (5.9)$$

$$B = \mu_0 \frac{Ni}{\left(\frac{l_{fe}}{\mu_r} + g\right)} \quad (5.10)$$

Realizing that $\mu_r \gg 1$ for ferromagnetic materials, the magnetic flux density of Figure 5.1 is approximately represented as the flux density within the air gap, as shown in (5.11).

$$B = \mu_0 \frac{Ni}{g} \quad (5.11)$$

Figure 5.2 depicts a slightly different magnetic configuration where the bottom piece of material, designated as the “flotor,” is separated from the electromagnet and is free to move. Figure 5.2 will serve as the basic model for a magnetic bearing.

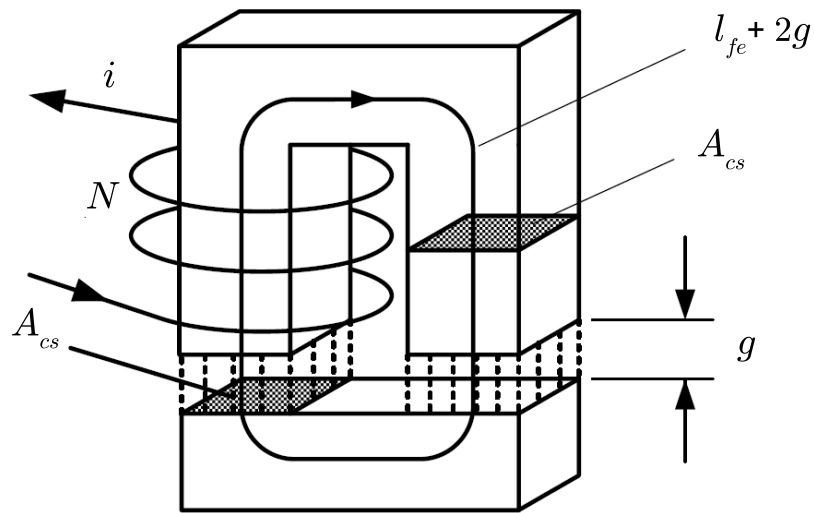


Figure 5.2: Basic magnetic bearing, from [1]

Following the same development as presented above, the air gap flux density for Figure 5.2 is found:

$$B = \mu_0 \frac{Ni}{2g} \quad (5.12)$$

Since the flux in Figure 5.2 is linked across two gaps instead of one, as in Figure 5.1, the $1/2$ factor appears.

The flux density B in (5.12) becomes large for small values of air gap g and large values of current i . Since the core is made of ferromagnetic material, magnetic saturation can occur for sufficiently large values of magnetic field intensity. Magnetic saturation of the core will place an upper bound on the magnetic flux density within the ferromagnetic core, rendering the linear B-H relationship defined in (5.3) to be inaccurate. In turn, (5.12) will not provide an accurate measure of the magnetic flux density in the air gap. This is an important consequence that will be investigated further in Section 5.4.

The following section will use (5.12) to develop an expression for the magnetic force applied to the flotor.

5.3 Magnetic Bearing Force

In contrast to the Lorentz force, which describes the magnetic forces acting on a current carrying conductor, a magnetic reluctance force is generated at the boundary of media with differing permeability μ [1]. In Figure 5.2 the magnetic reluctance force exerts an attractive force on the flotor, attempting to pull it toward the “U” shape electromagnet. If large enough, this force will pull the flotor until it makes contact with the electromagnet, resulting in an air gap distance g equaling zero.

Equation (5.13) describes the stored field energy W_{air} within a volume of air V_{air} , where B_{air} and H_{air} represent the magnetic flux density and magnetic field intensity within the volume of air, respectively.

$$W_{air} = \frac{1}{2}H_{air}B_{air}V_{air} \quad (5.13)$$

Consider the case when $V_{air} = A_{cs}2g$ as seen in Figure 5.2. The force acting on a ferromagnetic body (e.g. the flotor from Figure 5.2) is generated by a change in the air gap field energy W_{air} as a function of body displacement g [1]. If the air gap distance g increases by dg , the air gap volume V_{air} increases and the air gap field energy W_{air}

increases by dW_{air} . For a small displacement dg , the magnetic flux $B_{air}A_{cs}$ remains constant.

The increase in air gap field energy must be provided mechanically, and an attractive force must be overcome [1]. The reluctance force equals the partial derivative of the air gap field energy with respect to the air gap distance, and is taken from the principle of virtual displacement [1]:

$$f_m = -\frac{\partial W_{air}}{\partial g} \quad (5.14)$$

Equation (5.14) becomes (5.15) via substitution of (5.13) and noting $B_{air} = \mu_0 H_{air}$.

$$f_m = \frac{B_{air}^2 A_{cs}}{\mu_0} \quad (5.15)$$

The negative sign in (5.14) signifies f is generated from a change in coenergy with respect to displacement. The negative sign is dropped in (5.15) for simplification, as it is unneeded for the purpose of this thesis. A more in-depth derivation of (5.14) is seen in [34].

The force acting on the ferromagnetic flotor from Figure 5.2 is found via substitution of (5.12) into (5.15):

$$f_m = \frac{B^2 A_{cs}}{\mu_0} = \left(\mu_0 \frac{Ni}{2g} \right)^2 \frac{A_{cs}}{\mu_0} \quad (5.16)$$

and rearranging (5.16):

$$f_m = \frac{1}{4} \mu_0 N^2 A_{cs} \left(\frac{i}{g} \right)^2 \quad (5.17)$$

It is convenient to introduce the parameter k_B in (5.18). The parameter k_B represents the geometric design of the magnetic bearing and will remain fixed during the operation of the magnetic bearing.

$$k_B = \frac{1}{4} \mu_0 N^2 A_{cs} \quad (5.18)$$

The magnetic bearing force equation is now rewritten to emphasize its dependencies:

$$f_m(i, g) = k_B \left(\frac{i}{g} \right)^2 \quad (5.19)$$

It is important to note the nonlinear relationship of the magnetic force equation in (5.19) with respect to both current i and air gap g . Equation (5.19) indicates that the magnetic force produced in Figure 5.2 is proportional to the square of the current and to the inverse square of the air gap.

In order to utilize the magnetic bearing in Figure 5.2 as an *active* magnetic bearing, the nonlinear force/current and force/air gap relationships must be well understood. The following section investigates the magnetic bearing from the standpoint of active control.

5.4 Active Magnetic Bearing Control Considerations

Looking at (5.19), it is easy to see the potential of using the magnetic actuator in Figure 5.2 as a force controlled device. By dynamically changing the current in the coil, the magnetic actuator can produce a variable force. However, as the force is applied to a body (e.g. the flotor), a displacement will occur that changes the magnetic force due to the change in air gap. Thus, for the magnetic actuator to be used as a force controlled device, a firm understanding of the relationship between magnetic force, current, and air gap is absolutely necessary.

To help investigate the nonlinear dependencies of (5.19), Figure 5.2 is redrawn in Figure 5.3 to display the force of gravity on the flotor, f_g . The position of the flotor is measured by a displacement x in Figure 5.3.

Suppose a bias point exists such that $f_m(i_0, g_0) = f_g$, where i_0 and g_0 are the bias point current and air gap distance, respectively. If g and x are held at their bias point values, Figure 5.4 describes the magnetic force behavior to a changing i . For large values of i , the ferromagnetic material of the magnetic bearing core will saturate.

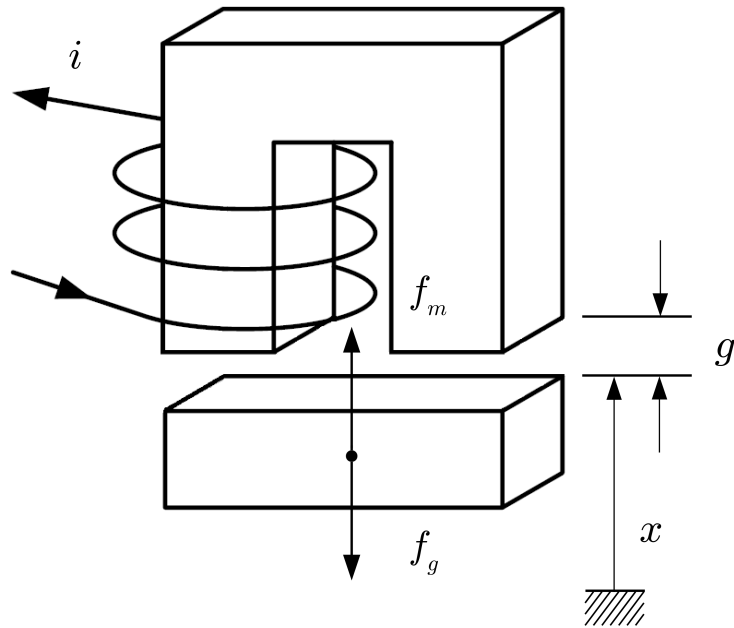


Figure 5.3: Basic magnetic bearing forces

On the other hand, Figure 5.5 describes the magnetic force behavior if i is held at its bias point value for a changing x . Note that increasing x results in decreasing g . For small values of g (large values of x), the ferromagnetic core of the magnetic bearing will saturate.

Figure 5.5 shows the magnetic force increasing dramatically with increasing x . This relationship causes an unstable behavior of the flotor (assuming a constant i_0), and results with the flotor striking the magnetic bearing. This behavior is opposite to the familiar behavior of a spring. Unlike the magnetic force, the force from a spring can change sign and repel the rotor as x increases, allowing the rotor to stabilize around the bias point.

The unstable behavior of the flotor is due to the negative mechanical stiffness of the magnetic bearing. In general, the mechanical stiffness k_{mech} of a bearing is defined

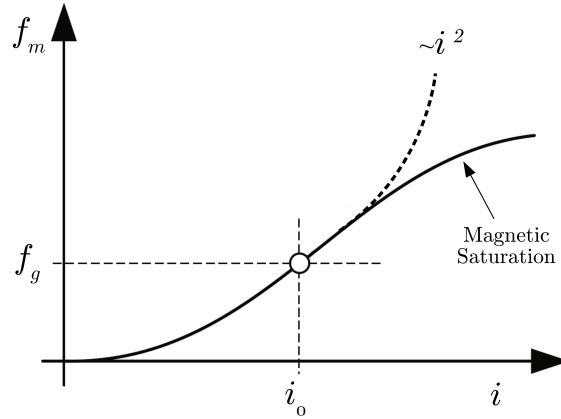


Figure 5.4: Bearing magnetic force vs. i when $x = x_0$, from [1]

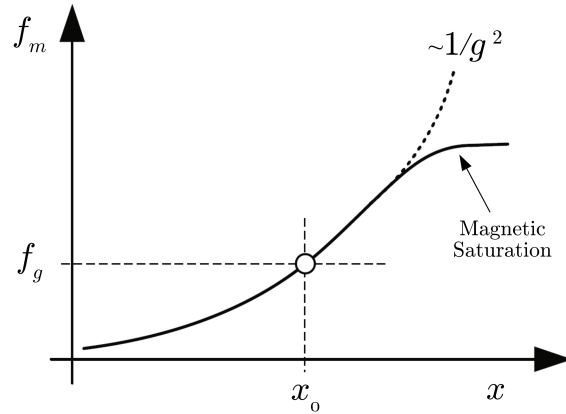


Figure 5.5: Bearing magnetic force vs. x when $i = i_0$, from [1]

as the negative derivative of its suspension force f_s with respect to displacement [1]:

$$k_{mech} = -\frac{df_s}{dx} \quad (5.20)$$

In other words, the mechanical stiffness is a measure of the force which opposes a given displacement. Equation (5.20) represents the mechanical stiffness behavior of a spring. However, Figure 5.5 displays a positive change in the suspension force (designated as f_m for the magnetic bearing) with respect to displacement. Thus, the mechanical stiffness for the magnetic bearing is:

$$k_x = \frac{df_m}{dx} \quad (5.21)$$

Equating (5.21) to the definition of mechanical stiffness in (5.20), the sign of k_x becomes negative.

Despite the strong nonlinearities with respect to current and air gap distance, an active magnetic bearing can usually be well controlled by a linear control scheme [1]. For the linear control scheme to be properly designed, the force/current and force/displacement relationships in Figures 5.4 and 5.5 must be linearized. The linearization is performed at the bias point (i_0, g_0) , which is the desired point of equilibrium for the active magnetic bearing system. Linearizing the magnetic force equation around the bias point provides the best performance for operation around the equilibrium state of the AMB system.

The following relationships are introduced to develop a small signal model around the bias point:

$$f = f_m - f_g \quad (5.22)$$

$$\Delta i = i - i_0 \quad (5.23)$$

$$\Delta x = x - x_0 \quad (5.24)$$

Using (5.22) through (5.24), Figures 5.6 and 5.7 depict the linearization around the bias point $f_m(i_0, g_0) = f_g$. The constants $k_x(N/m)$ and $k_i(N/A)$ approximate the force/displacement and force/current behavior of the magnetic bearing about the operating point, and yield the following small-signal relationship:

$$f(\Delta i, \Delta x) = k_x \Delta x + k_i \Delta i \quad (5.25)$$

The constants k_x and k_i are commonly called the “force/displacement factor” and the “force/current factor” [1]. Although k_x and k_i are developed graphically in this context, Section 6.3 describes a more formal derivation to calculate their values. The

values of parameters k_x and k_i depend on the bearing geometry and the choice of bias point values i_0 and g_0 .

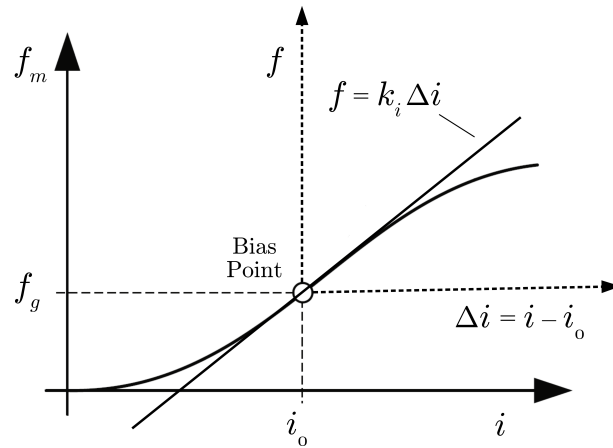


Figure 5.6: Bias point linearization of magnetic force vs. i , from [1]

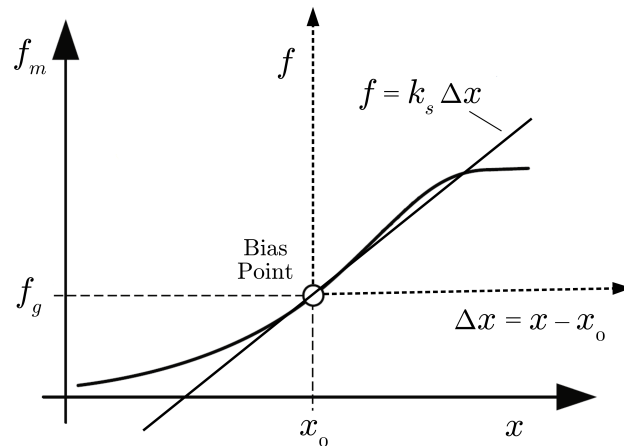


Figure 5.7: Bias point linearization of magnetic force vs. x , from [1]

Equation (5.25) is a linear approximation of the truly nonlinear magnetic bearing force. The approximation is only accurate within the operational vicinity of the bias point, i.e. for small deviations in current and air gap around i_0 and g_0 . However, linearization of the magnetic force equation about an operating point “has proved through many years of practical experience to work extraordinarily well for a wide range of applications [1].”

Accuracy limitations of (5.25) are present when the magnetic bearing is operated near the extremes of the B-H curve for the ferromagnetic core. Although a linear B-H relationship for the ferromagnetic material was assumed in the development of the magnetic force equation in Section 5.2, a true B-H relationship for ferromagnetic material is shown in Figure 5.8. It is apparent from Figure 5.8, that the linear region of the curve exists between the highly nonlinear extremes.

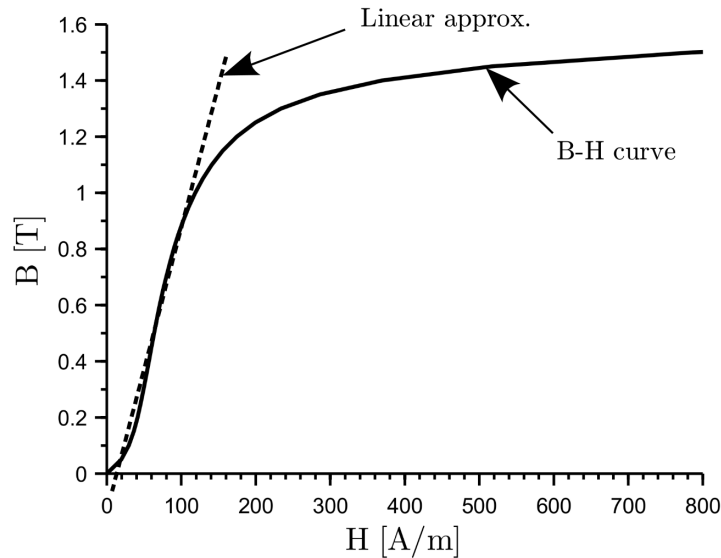


Figure 5.8: Typical magnetization curve for ferromagnetic material showing the region which can be approximated linearly

Therefore, the magnetic bearing bias point must be selected, or specifically designed, to exist somewhere between the nonlinear extremes of the B-H curve. In addition, the current and air gap deviations from the selected bias point must not push the magnetic bearing system into the nonlinear extremes. Ensuring that the magnetic bearing remains in the linear region of the B-H curve allows the linear approximation in (5.25) to be the most accurate. In turn, ensuring linear region operation allows the magnetic bearing control system to achieve its best performance.

One method of bias point selection is found in [33] and [35]. First, the maximum load capacity of the magnetic bearing is set to correspond with B_{sat} of the ferromagnetic

core. The bias flux B_0 is then set to $B_{sat}/2$ to produce a linear approximation of the entire operating range.

For instances of rotor-stator contact, flux saturation of the core, and low bias currents, it becomes necessary to use more detailed and typically nonlinear models [1]. However, these models are not necessary if the magnetic bearing system is not intended to operate in the aforementioned situations.

5.5 Bearing Coil Model

The magnetic force equation (5.19) shows that magnetic force is proportional to the square of the current i passing through the coil. A varying magnetic force is achieved by dynamically manipulating i , providing the ability to actively control the bearing force. However, the physical nature of the bearing coil and magnetic circuit limit the speed at which the current i , and thus bearing force, can change. A bearing coil model is developed to investigate the limitations of changing the bearing force.

Faraday's induction law predicts a back EMF will be induced in the magnetic bearing coil in Figure 5.2 for a change in air gap flux:

$$v_{emf} = N \frac{d\phi}{dt} \quad (5.26)$$

where N is the number of coil turns and ϕ is the air gap flux. As described in Section 5.2, this development assumes constant magnetic flux through both the air gap and ferromagnetic core. Thus, from (5.5) through (5.7):

$$\phi = \Phi = BA_{CS} \quad (5.27)$$

Kirchoff's Voltage Law for the AMB coil circuit is:

$$v_{coil} = iR + v_{emf} \quad (5.28)$$

where iR is the voltage drop caused by the coil resistance. Substituting (5.26) and (5.27) into (5.28) gives:

$$v_{coil} = iR + N \frac{d\phi}{dt} = iR + N \frac{dBA_{CS}}{dt} \quad (5.29)$$

Using the flux density equation from (5.12), equation (5.29) is rearranged:

$$v_{coil} = iR + \frac{1}{2} \mu_0 N^2 A_{cs} \frac{d}{dt} \left(\frac{i}{g} \right) \quad (5.30)$$

giving the bearing coil model in terms of bearing current and air gap.

For simplification, the definition of k_B from (5.18) is inserted into (5.30):

$$v_{coil} = iR + 2k_B \frac{d}{dt} \left(\frac{i}{g} \right) \quad (5.31)$$

Utilizing the quotient rule, equation (5.31) is expanded:

$$v_{coil} = iR + \frac{2k_B}{g} \frac{di}{dt} - \frac{2k_B i}{g^2} \frac{dg}{dt} \quad (5.32)$$

Equation (5.32) is the final form of the bearing coil model. Note the nonlinear nature of (5.32) due to its products and quotients of time dependent variables i and g .

In some coil model developments, such as [36], a leakage inductance term L_s is included to represent the voltage drop due to magnetic flux that is not linked through the air gap. The addition of L_s to (5.32) gives:

$$v_{coil} = iR + \left(L_s + \frac{2k_B}{g} \right) \frac{di}{dt} - \frac{2k_B i}{g^2} \frac{dg}{dt} \quad (5.33)$$

For this thesis, the leakage inductance term L_s is assumed to be very small and is neglected.

5.6 Single Axis Single Bearing Model

Combining the magnetic force model from Section 5.3 and the bearing coil model from Section 5.5, the complete SASB system model takes shape. The final piece of the model are the dynamics of the flotor. For the single degree of freedom situation depicted in Figure 5.3, the Newtonian equation of motion governs the system:

$$m\ddot{x} = f_m - mg_e \quad (5.34)$$

where m is the mass of the flotor and g_e is the force of gravity. This model assumes the flotor can only move along a single axis.

The magnetic force and bearing coil equations are repeated in (5.35) and (5.36), respectively, and together with (5.34) form the complete SASB AMB model.

$$f_m = k_B \left(\frac{i}{g} \right)^2 \quad (5.35)$$

$$v_{coil} = iR + \frac{2k_B}{g} \frac{di}{dt} - \frac{2k_B i}{g^2} \frac{dg}{dt} \quad (5.36)$$

Figure 5.9 displays the SASB system model using equations (5.34) through (5.36). The model in Figure 5.9 represents a nonlinear AMB model in which the flotor is constrained to move along one axis and is acted on by a single magnetic bearing against gravity. This single bearing model will be designated as the single-axis single-bearing (SASB) model to distinguish it from the single-axis dual-bearing model developed in the following section. The SASB model is used for the SASB test setup in Chapter 7.

Due to the nonlinearities of SASB AMB system, the system cannot be directly modeled as a linear time-invariant (LTI) system. A host of well known system analysis and control system design techniques exist for LTI systems, including root-locus, Bode

along a single axis. Therefore, an object (such as the flotor) can be fully controlled within one axis, regardless of its orientation relative to the force of gravity.

The SADB model is used to model the bearing behavior of each orthogonal axis of the SB and SLFBM systems. A two-bearing, single axis AMB model (such as the SADB) is a typical starting point for realizing radial and axial AMB systems.

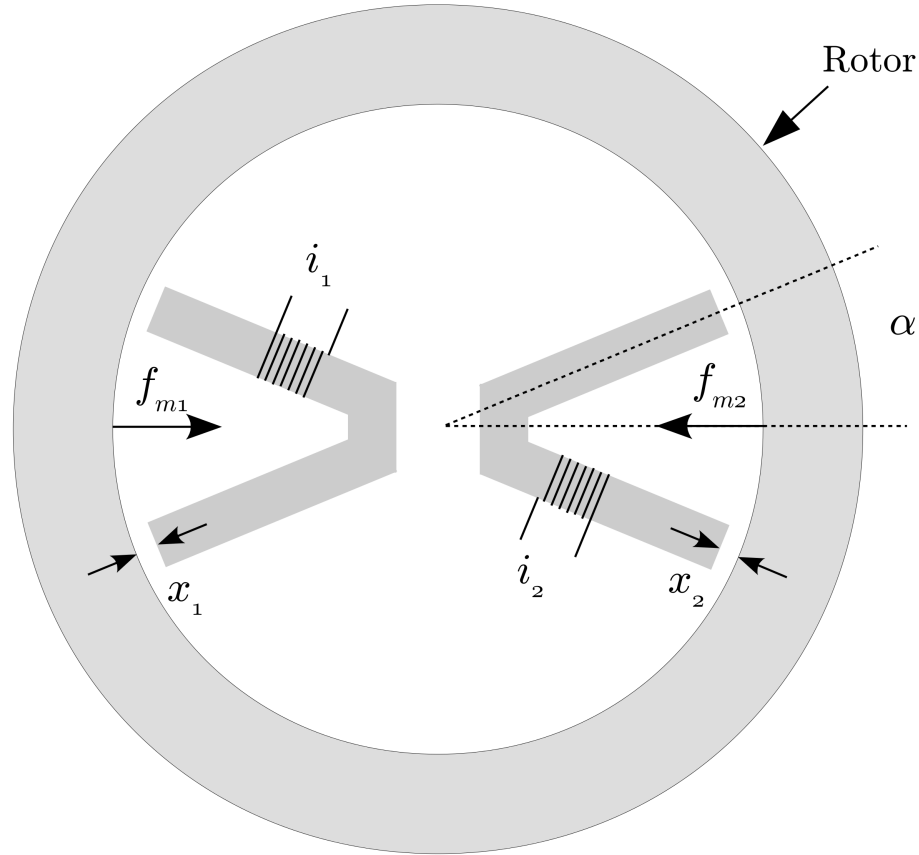


Figure 5.10: SADB model

The SADB model in Figure 5.10 is described by the following set of equations:

$$m\ddot{x} = f_{m_{total}} = f_{m1} - f_{m2} \quad (5.37)$$

$$f_{m1} = k_B \cos(\alpha) \left(\frac{i_1}{x_1} \right)^2 \quad (5.38)$$

$$f_{m2} = k_B \cos(\alpha) \left(\frac{i_2}{x_2} \right)^2 \quad (5.39)$$

$$v_{coil1} = i_1 R + \frac{2k_B}{x_1} \frac{di_1}{dt} - \frac{2k_B i_1}{x_1^2} \frac{dx_1}{dt} \quad (5.40)$$

$$v_{coil2} = i_2 R + \frac{2k_B}{x_2} \frac{di_2}{dt} - \frac{2k_B i_2}{x_2^2} \frac{dx_2}{dt} \quad (5.41)$$

Note that the force of gravity is ignored in (5.37) to preserve the generality of SADB model to any orientation. A small signal model is eventually derived, in which case the constant force of gravity drops off. A small signal model only models the SADB behavior for deviations in the vicinity of the bias point and does not model constant forces. The mathematical SADB system model described by equations (5.37) through (5.41) is given in Figure 5.11.

The SADB system is controlled about a bias point (i_0, g_0) . The displacement Δx of the flotor from its equilibrium position g_0 is related to the bearing air gaps:

$$x_1 = g_0 - \Delta x \quad (5.42)$$

$$x_2 = g_0 + \Delta x \quad (5.43)$$

To account for the flotor displacement from its equilibrium position, bearing forces are adjusted accordingly. To adjust bearing forces, the bearing currents are adjusted from the bias current i_0 by a control current Δi in the following manner:

$$i_1 = i_0 + \Delta i \quad (5.44)$$

$$i_2 = i_0 - \Delta i \quad (5.45)$$

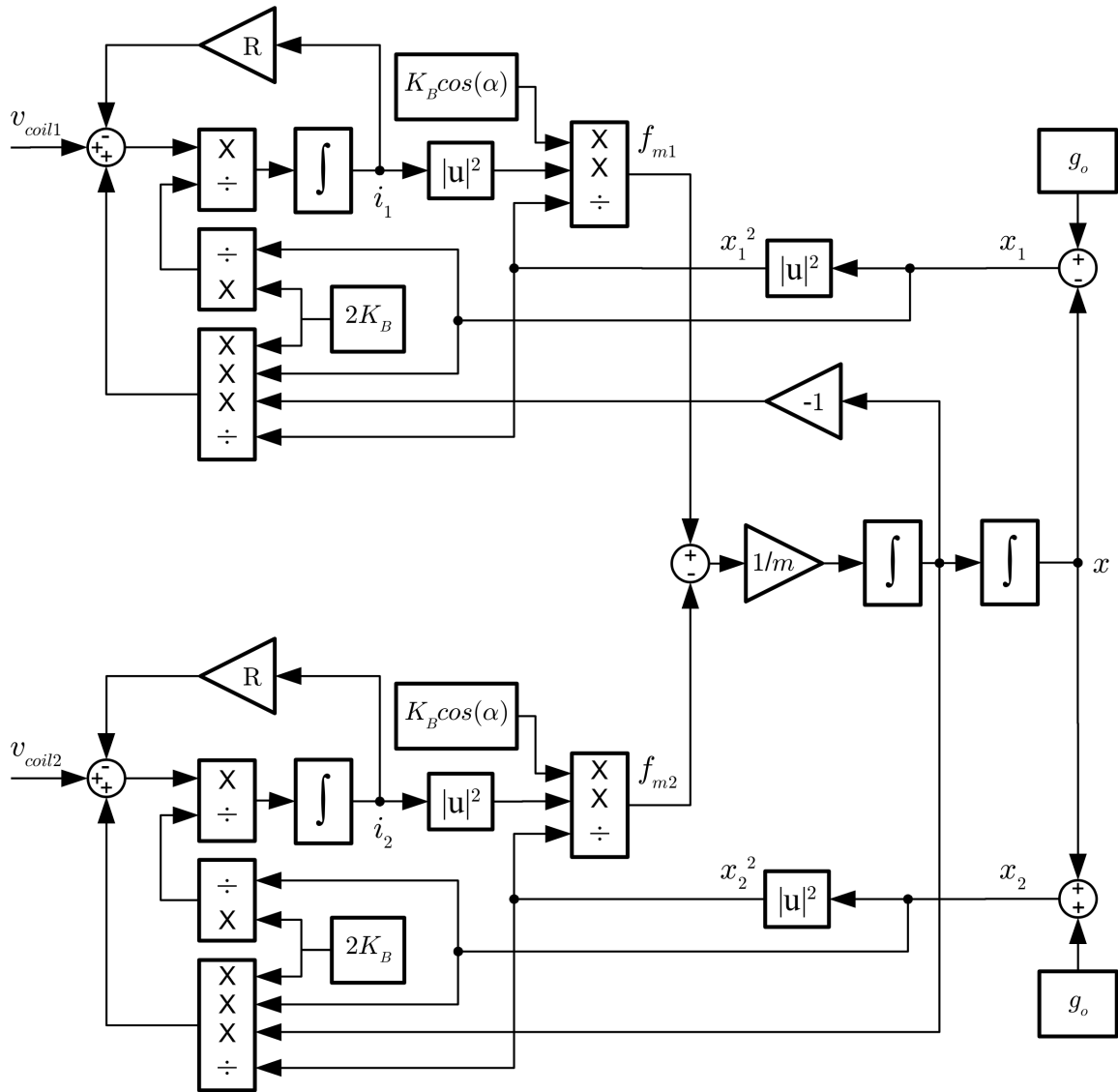


Figure 5.11: Nonlinear SADB AMB model

Equations (5.44) and (5.45) describe the so-called “differential driving mode” scheme. If the magnetization of iron is neglected, a differential driving mode produces a linear force-current relationship [37]. Retaining a linear force-current relationship is an essential result to developing an overall linear approximation of the AMB behavior.

Similar to the SASB model, the SADB model is also nonlinear. The SADB model is approximated as a LTI system by linearization around a desired operating point. Linearization of the SADB system is described in Section 6.3.

Chapter 6

Active Magnetic Bearing Control System

6.1 Introduction

This chapter discusses various aspects of the AMB control system utilized for the UIFESS. The UIFESS AMB control scheme is a decentralized, current controlled approach that is implemented digitally. Descriptions of this control scheme along with the rationale behind its selection for the UIFESS is given in Sections 6.2, 6.4, and 6.5. The linearization and derivation of the small signal transfer functions for the SASB and SADB models are given in Section 6.3. PID position controllers were selected for controlling the SASB and SADB models and are discussed in Section 6.6.

The remaining sections of this chapter help develop the digital control algorithms for the UIFESS AMB control, including the PID position controller (Section 6.6) and underlying hysteresis current controller (Section 6.10). In order to design the PID position controller and to account for the effects of the digital sampling delay and ZOH element, the SASB and SADB small signal transfer functions must be transformed into z -domain, this development given in Section 6.9.

6.2 Current vs. Voltage Control

As previously described, the magnetic bearing force is dependent on the bearing coil current i . The ability to produce an adjustable force is achieved by appropriately changing i . In order to realize a magnetic bearing which can dynamically react to force imbalances and stabilize an object, such as the flotor from Figure 5.3, a control loop is designed to manipulate the coil current in response to an object's displacement. In AMB control literature, this is referred to as "current control" and is shown in Figure 6.1.

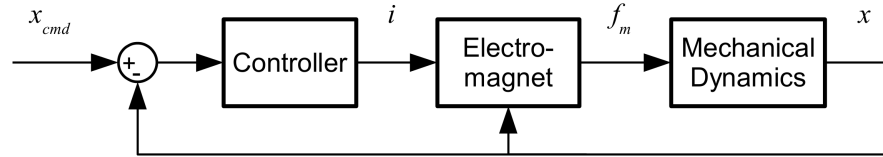


Figure 6.1: Current Controlled AMB

The control system in Figure 6.1 operates under the assumption that the magnetic bearing current i instantly tracks the commanded current signal from the controller. However, the inductance of the magnetic bearing coil will resist any sudden changes in current and the coil current will be unable to perfectly track the commanded value. Fast current changes can only be achieved by a suitably large voltage across to the coil.

In practice, a limit exists on the maximum voltage that may be applied to the coil in an AMB system. Therefore, to correctly model the AMB system the current must be considered a system state, and the dynamics associated with the inductance must be taken into account. The voltage across the coil now becomes the control variable. This type of AMB control is referred to as “voltage control” and is shown in Figure 6.2 [1]. The coil model including the inductance dynamics was developed in Section 5.5.

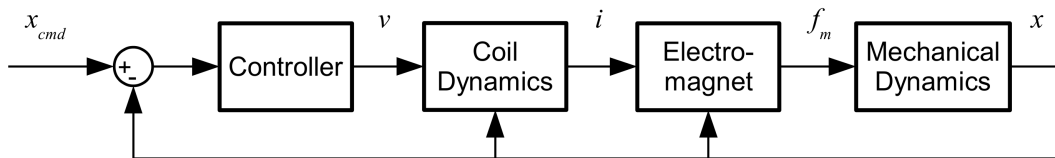


Figure 6.2: Voltage controlled AMB

In order to deal with the bearing coil dynamics, current controlled AMBs utilize an underlying current control loop. The current control loop is designed to be much faster than the remaining dynamics of the system such that the real component of the eigenvalue corresponding to the bearing coil dynamics has a large negative value [1]. Figure 6.1 is redrawn in Figure 6.3 to incorporate the underlying current control loop for the current controlled AMB.

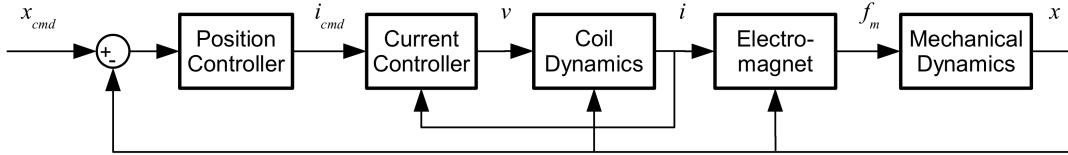


Figure 6.3: Current controlled AMB with underlying current control loop

The design decision between implementing current control or voltage control depends on the specific AMB application, as each method has advantages and disadvantages. Voltage control offers better overall system robustness since the plant model is more accurate [1]. There is also no need to design an underlying current control loop.

However, since voltage control incorporates the dynamics of the bearing coil, the system plant order is now raised to three. The increased system plant order prohibits the use of simpler, more well known, PD or PID controllers. A voltage control scheme instead demands a more complex controller design. In addition, in the case of voltage control, the control parameters can no longer be readily interpreted by an analogy to a mechanical spring-damper system. It is for these reasons that, historically, most industrial AMB applications have employed current control [1].

The UIFESS design utilizes current controlled AMBs with an associated underlying current control loop. This decision allows the use of PID position controllers, which offer a relatively simple design and implementation.

6.3 Linearization of Current Controlled AMB

As stated in Section 6.2, current controlled AMBs are employed for the UIFESS. Current controlled AMBs decouple the bearing coil dynamics from the remaining AMB system plant, and feature a separate underlying current control loop. A position controller serves as the outer control loop.

From the perspective of the position controller, the inner current control dynamics are assumed to be instantaneous. In other words, the current commanded by the position

controller is instantaneously present within the bearing coil. Although instantaneous changes in current are not physically achievable, this assumption is made to decouple the design of the position controller from the bearing coil dynamics. In turn, the PID position controller can now be designed directly from the simplified (i.e., second order) system plant, which does not include the bearing coil dynamics.

In order to find the transfer function for the AMB system plant, the SASB and SADB models must be linearized. As described in Section 5.4, the linearization is taken around the bias point to achieve the best performance from the linear controller. With the bearing coil dynamics ignored, only the magnetic force equations (5.19) and (5.37), from the SASB and SADB models, respectively, must be linearized.

A linear approximation of a nonlinear function $h(a, b)$ about a bias point (a_0, b_0) is accomplished using the Taylor series expansion:

$$h(a, b) \approx h(a_0, b_0) + \left. \frac{\partial h(a, b)}{\partial a} \right|_{\substack{a=a_0 \\ b=b_0}} (a - a_0) + \left. \frac{\partial h(a, b)}{\partial b} \right|_{\substack{a=a_0 \\ b=b_0}} (b - b_0) + \dots \quad (6.1)$$

while neglecting the higher order terms. Applying equation (6.1) to the magnetic force equations from each model give different results and are presented in the following sections.

Although not utilized in this thesis, linearization for a voltage controlled AMB system is given in [12]. It is convenient to perform a linearization of a voltage controlled AMB system using a Jacobian matrix due to the added complication of linearizing the coil bearing dynamics.

6.3.1 Single Axis Single Bearing Force Linearization

Applying (6.1) to (5.19) at the bias point (i_0, g_0) , the linearized SASB magnetic force equation is found:

$$f_m(i, g) \approx f_m(i_0, g_0) + k_B \frac{-2i_0^2}{g_0^3} \Delta s + k_B \frac{2i_0}{g_0^2} \Delta i \quad (6.2)$$

In order to properly relate (6.2) to (5.34), Equation (6.2) must be defined relative to body displacement x . Since $\Delta s = -\Delta x$, (6.2) becomes:

$$f_m(i, g) \approx f_m(i_0, g_0) + k_B \frac{2i_0^2}{g_0^3} \Delta x + k_B \frac{2i_0}{g_0^2} \Delta i \quad (6.3)$$

The force/displacement factor k_x and the force/current factor k_i are thus:

$$k_x = k_B \frac{2i_0^2}{g_0^3} \quad (6.4)$$

$$k_i = k_B \frac{2i_0}{g_0^2} \quad (6.5)$$

With the linearized magnetic force equation from (6.3), the linearized current controlled AMB plant is given:

$$m\ddot{x} = f_m(i_0, g_0) + k_x \Delta x + k_i \Delta i - mg_e \quad (6.6)$$

By setting the bias point (i_0, g_0) such that $f_m(i_0, g_0) = mg_e$, the s-domain linearized small signal plant becomes (Δ signs are removed, but still assumed):

$$ms^2 X(s) = k_x X(s) + k_i I(s) \quad (6.7)$$

giving the transfer function:

$$G(s) = \frac{X(s)}{I(s)} = \frac{k_i/m}{s^2 - k_x/m} \quad (6.8)$$

The open loop poles for (6.8) are $\lambda_1 = +\sqrt{|k_x|/m}$ and $\lambda_2 = -\sqrt{|k_x|/m}$. Clearly, λ_1 exists in the right half of the complex plane, mathematically verifying the open loop instability of the magnetic bearing described in Section 5.4. Therefore, a controller must be designed to shift the open loop poles into the left hand side of the complex plane while providing sufficient damping and system control.

6.3.2 Single Axis Dual Bearing Force Linearization

To linearize the SADB force equation, Equations (5.42) through (5.45) are substituted into the right hand side of (5.37):

$$f_{m_{total}}(\Delta i, \Delta x) = k_B \cos(\alpha) \left(\frac{i_0 + \Delta i}{g_0 - \Delta x} \right)^2 - k_B \cos(\alpha) \left(\frac{i_0 - \Delta i}{g_0 + \Delta x} \right)^2 \quad (6.9)$$

Equation (6.9) is linearized around the bias point $(\Delta i_0, \Delta x_0)$. Unlike the SASB magnetic force equation, the SADB magnetic force equation in (6.9) is already derived from a small-signal perspective. Therefore, the desired operating point for (6.9) is when complete cancellation of the bearing forces exist, which is realized for $(\Delta i_0, \Delta x_0) = (0, 0)$.

Applying (6.1) to (6.9) at the bias point $(\Delta i_0, \Delta x_0)$, the linearized SADB magnetic force equation is found:

$$f_{m_{total}}(\Delta i, \Delta x) \approx f_{m_{total}}(\Delta i_0, \Delta x_0) + k_B \cos(\alpha) \frac{4i_0^2}{g_0^3} \Delta x + k_B \cos(\alpha) \frac{4i_0}{g_0^2} \Delta i \quad (6.10)$$

The force/displacement factor k_x and the force/current factor k_i become:

$$k_x = k_B \cos(\alpha) \frac{4i_0^2}{g_0^3} \quad (6.11)$$

$$k_i = k_B \cos(\alpha) \frac{4i_0}{g_0^2} \quad (6.12)$$

Since $f_{m_{total}}(\Delta i_0, \Delta x_0) = f_{m_{total}}(0, 0) = 0$, the linearized s-domain small signal plant becomes (again, the Δ signs are removed but still assumed):

$$ms^2 X(s) = k_x X(s) + k_i I(s) \quad (6.13)$$

giving the transfer function:

$$G_{SADB}(s) = \frac{X(s)}{I(s)} = \frac{k_i/m}{s^2 - k_x/m} \quad (6.14)$$

Although the structure of the transfer function in (6.14) is identical to the SASB case in (6.8), the values of k_i and k_x are different. The SADB transfer function plant in (6.14) is used to design the UIFESS decentralized PID controllers for the SB and SLFBM systems.

6.4 Digital Control Implementation

Although the first applications of AMB control systems were realized in analog electronics, digital control has now become the standard means for AMB control [1]. The transition from analog to digital control was driven by advances in the speed and peripheral capabilities of microprocessors. Digital control offers much higher flexibility over analog control. Among the many advantages of digital control (a more detailed list is available in [1]), the following advantages were most important for the selection a digital control scheme for the UIFESS [1, 21]:

- Controller parameters are easily tuned, enabling rapid prototyping.
- No controller parameter drift due to aging and temperature change.

- Possibility for adaptive control techniques and gain scheduling or speed dependent controller behavior.
- Ability to implement special start-up and shut-down procedures for the AMB system and UIFESS.

Although not utilized in this stage of the UIFESS project, a digital control system could eventually enable full system monitoring with real time feedback. The monitoring system could provide the UIFESS operator with information regarding bearing forces, air gap distances, flywheel speed, and temperature data among other operating conditions.

Digital control does exhibit some limitations. Digital sampling speeds, quantization noise, and calculation delays may limit a digital control system's ability to control high frequency system dynamics. These limitations are further discussed in Section 6.7.

6.5 Decentralized Control

The UIFESS employs a decentralized control scheme. A decentralized control scheme decouples the control of each bearing unit. For the UIFESS, the SB and SLFBM are the decoupled bearing units. Within each bearing unit, the x and y axes are controlled separately with feedback from a "local" sensor and controller [1]. A decentralized control scheme features no communication between bearing units. Each local controller is responsible for maintaining the air gap in its respective axis. Figure 6.4 depicts the decentralized control scheme for a conventional machine where the rotor is enclosed within the stator.

The main reason a decentralized control scheme was selected for the UIFESS is simplicity. The decentralized control scheme was chosen for the following reasons:

- **AMB Control Hardware Simplification.** Due to the processing requirements and the speed of the digital controllers available, two separate controllers are required for the SB and SLFBM control. A decentralized control scheme removes the

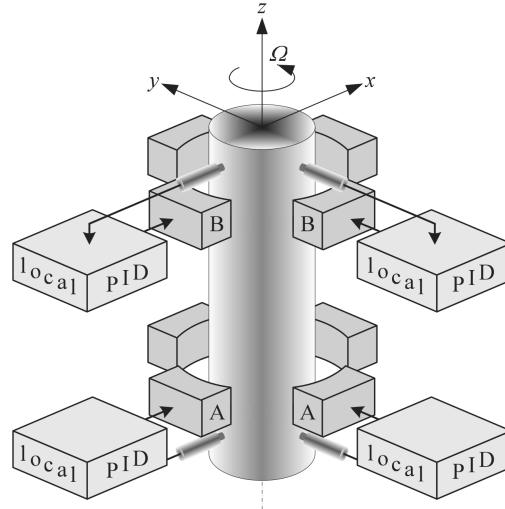


Figure 6.4: Decentralized control scheme for a conventional inner-rotor design, from [1]

complication of processor communication and coordination [22]. In addition, the decentralized control scheme provided a nice division of the required digital controller processing, allowing the UIFESS to utilize less expensive microcontrollers.

- **AMB Modeling and Control Simplification.** Each axis in the decoupled bearing units is modeled separately by the second order plant in Equation (6.14). The relatively low order plant is achieved by simplifying the rotor dynamics into four separate single DOF motion models with current controlled AMBs. In turn, the second order plant allows the use of PID controllers, a simple, well-known controller.
- **Adequate for Rigid Rotor Model.** The dynamic modeling of the UIFESS rotor is centered around the assumption that the UIFESS rotor is infinitely rigid. The “rigid rotor” assumption greatly simplifies the modeling of the UIFESS rotor dynamics [17].
- **Common in Industry.** Decentralized control of a rigid rotor is common practice for industrial AMB systems [1]. Decentralized control is a proven method for FES systems [25, 24].

6.6 PID Position Control

As mentioned in Sections 6.2 and 6.5, an important advantage of utilizing a decentralized control scheme along with a current controlled AMB scheme was to take advantage of PID controllers. The PID controller is extremely prevalent in a wide range of process control applications in industry. The PID controller is also prevalent in industrial AMB systems, as the main share of industrial AMBs utilize PID controllers [27]. The PID controller offers the following advantages:

- **Ease of Design.** PID tuning and design methods are numerous, well understood, and well documented.
- **Ease of Implementation.** As is discussed in Section 6.5, the UIFESS control system is implemented digitally within a set of microcontrollers. A PID controller is easily implemented within a digital microcontroller. In addition, the digital PID algorithm poses very little processing overhead.
- **Proven in Industrial Applications of AMB systems.** From [1], the PID controller is “well applicable for and achieving an absolutely satisfying closed-loop system in a large number of industrial applications.”

6.7 Digital Control Aspects

The UIFESS PID controllers are implemented digitally within the SB and SLFBM microcontrollers. Despite the advantages described for digital control in Section 6.4, an important consideration surrounding any digital control design is its inherent time delays due to sampling and microcontroller calculation. Sampling and calculation time delays create a phase lag between sensor feedback and controller response. In turn, the phase lag degrades the performance of the controller and in some cases can lead to instabilities.

To minimize the phase lag of the digital controller, a microcontroller of suitable speed and sampling rate capabilities must be chosen.

The sampling frequency of the digital control system must be set high enough to capture all plant dynamics that must be controlled. The Shannon theorem indicates that a signal can not be properly reconstructed when sampled at a rate lower than half the signal frequency [1]. The upper limit of frequencies that can be properly reconstructed by a given sampling rate f_s is referred to as the Nyquist frequency f_{Ny} :

$$f_{Ny} = \frac{f_s}{2} \quad (6.15)$$

Therefore, the Shannon theorem dictates that the sampling frequency must be at least twice the highest frequency where the plant dynamics exist. For example, plant dynamics at 1 kHz can only be correctly reproduced within, and controlled by, a digital controller with a sampling rate of at least 2 kHz. In practice, the sampling rate must be chosen even higher, from five to ten times the highest frequency of the plant dynamics [1].

Frequencies of the plant dynamics which are higher than f_{Ny} are mapped into the digital controller below f_{Ny} as noise. This phenomenon is known as aliasing. To prevent the aliasing induced noise from effecting the system, analog anti-aliasing filters are designed to appropriately match the sampling frequency f_s . The analog anti-aliasing filters are employed in the feedback path and are realized in hardware. The UIFESS anti-aliasing filters are described in [16].

Due to time restraints, a detailed analysis of the plant dynamics was not completed to determine the frequencies that must be controlled in order to maintain stability. However, a 10 kHz sampling rate was selected for the UIFESS controllers. A 10 kHz position sampling rate is a typical sampling rate for magnetic bearing systems according to [1] and was utilized to success for AMB applications in [27, 38].

The UIFESS employs TMS320F28335 microcontrollers from the Texas Instruments family of C2000 microcontrollers. The C2000 family are 32-bit microcontrollers designed for real-time control applications and are math-optimized. With these characteristics in mind, the TMS320F28335 is believed to produce minimum calculation delays and fast sampling times. More information on the UIFESS microcontroller selection is available in [16].

6.8 Digital PID Algorithm

Equation (6.16) gives the transfer function for a continuous time PID controller in parallel form:

$$C_c(s) = K_P + K_I \frac{1}{s} + K_D s \quad (6.16)$$

The constants K_P , K_I , and K_D represent the proportional, integral, and derivative gains of the PID controller. By appropriately setting K_P , K_I , and K_D , the closed loop response of the inherently unstable SASB and SADB plants can be stabilized. The introduction of the PID controller in a closed loop topology moves the open loop system poles from the right half of the complex plane into stable locations in the left half plane. In addition to stability, the controller gains dictate the specific response of the system to various forms of disturbances, such as an external imbalance force on the flotor.

The derivative portion $K_D s$ in (6.16) is very sensitive to high frequency noise and can potentially lead to unstable behavior. This fact is apparent since $K_D s$ goes to infinity for large values of s , and large values of s exist for high frequencies. Therefore, in practice it is necessary to limit the high frequency gain of the derivative action $K_D s$ by introducing a first order filter [39]. The derivative portion of (6.16) is approximated by:

$$K_D s \approx \frac{K_D s}{T_D s + 1} \quad (6.17)$$

which acts as a derivative term for frequencies below f_D where:

$$f_D = \frac{1}{2\pi T_D} \quad (6.18)$$

Frequencies above f_D are attenuated by the first order filter, thus limiting the high frequency gain. Substitution of (6.17) into the PID transfer function from (6.16) gives:

$$C_c(s) = K_P + K_I \frac{1}{s} + \frac{K_D s}{T_D s + 1} \quad (6.19)$$

To implement the PID algorithm within a microcontroller, the continuous time PID controller transfer function in (6.19) is first converted to its discrete equivalent in the z -domain. From the z -domain transfer function, a set of discrete time difference equations are derived and programmed within the microcontroller. The discrete time difference equations approximate continuous time differential equations and emulate the behavior of (6.19).

To transform (6.19) to the discrete domain, the bilinear transformation in (6.20) is utilized:

$$s \leftarrow \frac{2}{T_s} \frac{z - 1}{z + 1} \quad (6.20)$$

where T_s is the discrete sampling time. The bilinear transformation is a common method for transforming s -domain transfer functions into the z -domain. The bilinear transform gives better agreement to the continuous PID controller than the forward or backward transformations.

Applying the bilinear transform from (6.20) to (6.19), the discrete time PID controller transfer function is given:

$$C_d(z) = K_P + K_I \frac{T_s}{2} \frac{z + 1}{z - 1} + K_D \frac{1}{T_D + \frac{T_s}{2} \frac{z + 1}{z - 1}} \quad (6.21)$$

Figure 6.5 compares the magnitude and phase of the frequency responses for the three PID controller forms: continuous time (6.16), continuous time with derivative filter (6.19), and discrete time with derivative filter (6.21). The result of the derivative filter in (6.19) and (6.21) limits the magnitude at higher frequencies. In this instance T_D is 571 Hz. Also note the increased phase lag of the discrete PID controller at higher frequencies as a result of the bilinear transformation. The increased phase lag is an expected consequence of the bilinear transformation.

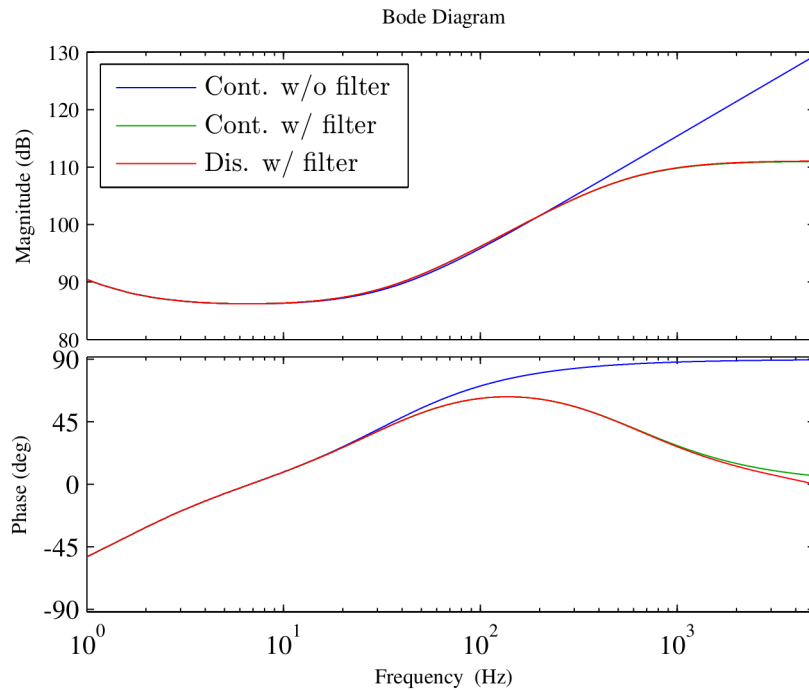


Figure 6.5: Magnitude and phase of the frequency response for three types of PID controllers: continuous time without derivative filter, continuous time with derivative filter, and discrete time with derivative filter

The z -domain PID controller transfer function in (6.21) is used to develop the discrete time difference equations which are programmed within the microcontroller. First, (6.21) is rewritten as a combination of transfer functions which separately describe the proportional, integral, and derivative actions:

$$C_d(z) = C_{Prop}(z) + C_{Int}(z) + C_{Deriv}(z) \quad (6.22)$$

Taking $C_d(z) = Y(z)/E(z)$, where $Y(z)$ is the output and $E(z)$ is the input to the PID controller, (6.22) is rewritten in terms of input and output quantities:

$$Y(z) = E(z)C_{Prop}(z) + E(z)C_{Int}(z) + E(z)C_{Deriv}(z) = Y_{Prop}(z) + Y_{Int}(z) + Y_{Deriv}(z) \quad (6.23)$$

where $Y_{Prop}(z)$, $Y_{Int}(z)$, and $Y_{Deriv}(z)$ represent the output of the proportional, integral, and derivative portions, respectively.

The PID difference equation is found using the time delay property of z-transforms:

$$\mathcal{Z}\{f(k-n)\} = z^{-n}F(z) \quad (6.24)$$

where k is the discrete unit of time representing the k^{th} instant in time. Applying (6.24) to each term from (6.23) gives:

$$y_{Prop}(k) = K_P e(k) \quad (6.25)$$

$$y_{Int}(k) = K_I \frac{T_s}{2} [e(k) + e(k-1)] + y_{Int}(k-1) \quad (6.26)$$

$$y_{Deriv}(k) = \frac{2K_D[e(k) - e(k-1)] - y_{Deriv}(k-1)(-2T_D + T_s)}{2T_D + T_s} \quad (6.27)$$

From (6.23) and Equations (6.25) through (6.27), the final form of the PID difference equation is:

$$y(k) = y_{Prop}(k) + y_{Int}(k) + y_{Deriv}(k) \quad (6.28)$$

6.9 Discretization of AMB System Plant

One important consideration behind using digital control for an analog system is considering the interface between digital and analog systems, i.e. the interface of the discrete

and continuous time domains. The digital and analog systems interface at two points in the overall system:

1. An analog to digital conversion (ADC) at the output of the analog plant
2. A digital to analog conversion (DAC) at the input of the analog plant

In order to properly design the digital control system, the ADC and DAC interactions must be modeled within the system. Figure 6.6 depicts the interaction between the analog and digital systems.

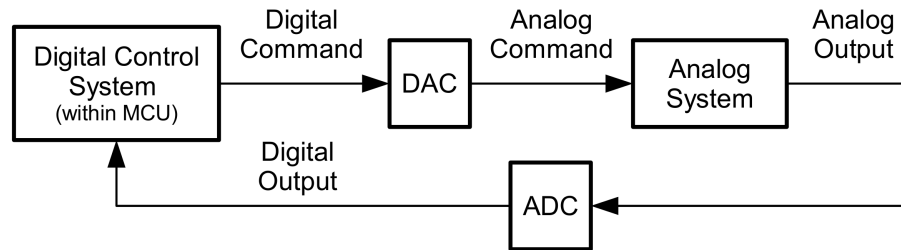


Figure 6.6: Interaction between analog and digital portions of the AMB control system

In order to represent an analog value within a digital system, an ADC operation must occur. The ADC discretizes the analog output at a specified sampling rate. In most engineering applications, modeling the ADC as an ideal sampler is an acceptable idealization [40]. Modeling the ADC as an ideal sampler operates under the following assumptions [40]:

- The discretized output of the ADC is equal to its analog counterpart, i.e. quantization errors are neglected.
- The ADC occurs instantaneously
- Sampling rate is perfectly uniform

For the DAC interaction at the input of the analog plant, the digital control system only changes state at the end of each sampling period and remains constant during each

sampling period. During the sampling period when the digital control output is constant, values in the analog plant can dynamically change. Therefore, the DAC is modeled as a zero-order hold (ZOH) element. Modeling the DAC as a ZOH operates under the following assumptions [40]:

- The analog output of the DAC is equal to its digital counterpart
- The DAC occurs instantaneously
- The DAC output is perfectly constant during the sampling period

The ZOH is the most commonly used DAC model and is utilized in most digital control texts [40]. Although the ZOH is an idealization of the true DAC behavior, it is sufficiently accurate for most engineering applications [40].

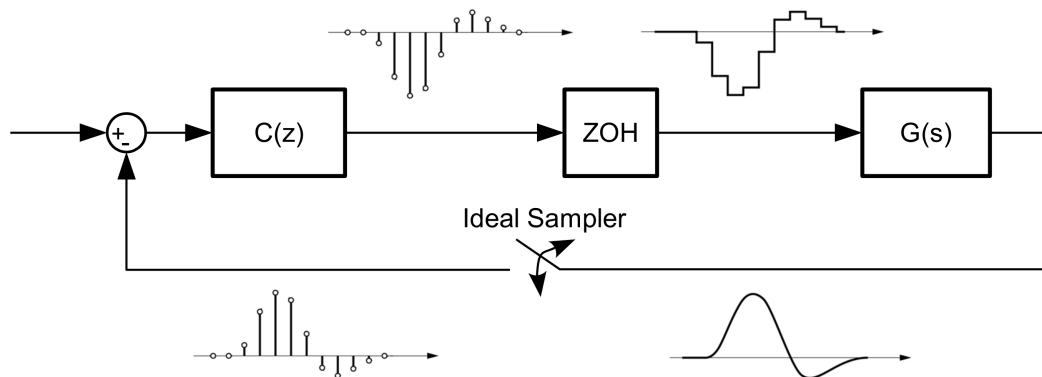


Figure 6.7: AMB control system with ideal sampler and ZOH models

Utilizing the ideal sampler and ZOH models for the ADC and DAC operations is depicted in Figure 6.7. The ZOH and ideal sampler allows for the conversion of the analog plant, which is described in the s -domain, to be modeled within the z -domain. With the entire system modeled in the z -domain, the design of the digital controller is performed. The equivalent z -domain transfer function of the analog plant utilizing the ZOH and ideal sampler models is given:

$$G_z(z) = (1 - z^{-1})\mathcal{Z} \left\{ \mathcal{L}^{-1} \left[\frac{G(s)}{s} \right]^* \right\} \quad (6.29)$$

where the * indicates that a sampling of the analog time domain function is necessary before the z-transformation is performed.

Equation (6.29) is applied to the SASB (6.8) and SADB (6.14) analog plants to convert the plants to the z-domain. Once the analog plant is modeled in the z-domain, the digital PID design can be performed for each system. The SASB and SADB plant transfer functions exhibit the identical structure:

$$G_c(s) = \frac{k_i/m}{s^2 - k_x/m} \quad (6.30)$$

and only differ in their values of k_x , k_i , and m . Therefore, (6.29) is applied to the general form of (6.30) and then specifically applied to the specific SASB or SADB case at hand.

The development begins with finding the impulse response of $G_c(s)/s$. First, partial fraction expansion is performed:

$$G_c(s)' = \frac{G_c(s)}{s} = \frac{k_i}{k_x} \left[\frac{-1}{s} + \frac{1/2}{s - \sqrt{\frac{k_x}{m}}} + \frac{1/2}{s + \sqrt{\frac{k_x}{m}}} \right] \quad (6.31)$$

Thus the impulse response becomes:

$$g_c(t)' = \frac{k_i}{k_x} \left[-1 + \frac{1}{2}e^{\beta t} + \frac{1}{2}e^{-\beta t} \right] \quad (6.32)$$

where:

$$\beta = \sqrt{\frac{k_x}{m}} \quad (6.33)$$

Taking the z-transforms of the corresponding discrete time functions of (6.32) gives $G_z(z)'$ in (6.34), where T_s is the digital sampling period. This step is accomplished using a common Laplace to z-transform table.

$$G_z(z)' = \frac{k_i}{k_x} \left[\frac{-z}{z-1} + \frac{1/2 z}{z - e^{\beta T_s}} + \frac{1/2 z}{z - e^{-\beta T_s}} \right] \quad (6.34)$$

The final step in the digital conversion is the multiplication by $(1 - z^{-1})$:

$$G_z(z) = (1 - z^{-1})G_z(z)' = \frac{\mathcal{B}_1 z + \mathcal{B}_0}{z^2 + \mathcal{A}_1 z + 1} \quad (6.35)$$

where:

$$\mathcal{B}_1 = \mathcal{B}_0 = \frac{k_i}{k_x} \left[\frac{1}{2} e^{-\beta t} + \frac{1}{2} e^{\beta t} - 1 \right] \quad (6.36)$$

$$\mathcal{A}_1 = -e^{-\beta t} - e^{\beta t} \quad (6.37)$$

Equation (6.35) gives the z-domain transfer function for the SASB and SADB system plants and correctly models the effects of the ZOH and ideal sampler on the continuous time s-domain system plant. Figure 6.7 is now redrawn in Figure 6.8 using the z-domain plant in (6.35). The z-domain plant in (6.35) is used to design the digital PID controllers for the SASB and SADB models.

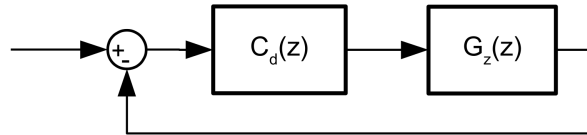


Figure 6.8: Equivalent z-domain system to Figure 6.7

6.10 Underlying “Inner” Current Control

The inner current control for each bearing coil is performed with separate hysteresis (also known as bang-bang) controllers. Hysteresis control was chosen for its simplistic design and low processing overhead within the microcontroller. The low processing overhead is especially important for the SLFBM controller, which is responsible for current control within 24 different coils.

The hysteresis current control algorithm is shown in Figure 6.9. The variable i_{meas} denotes the measured bearing coil current. The variable i_{cmd} denotes the bearing

coil current command by the PID position controller. The commanded current i_{cmd} is updated after each execution of the PID position controller algorithm.

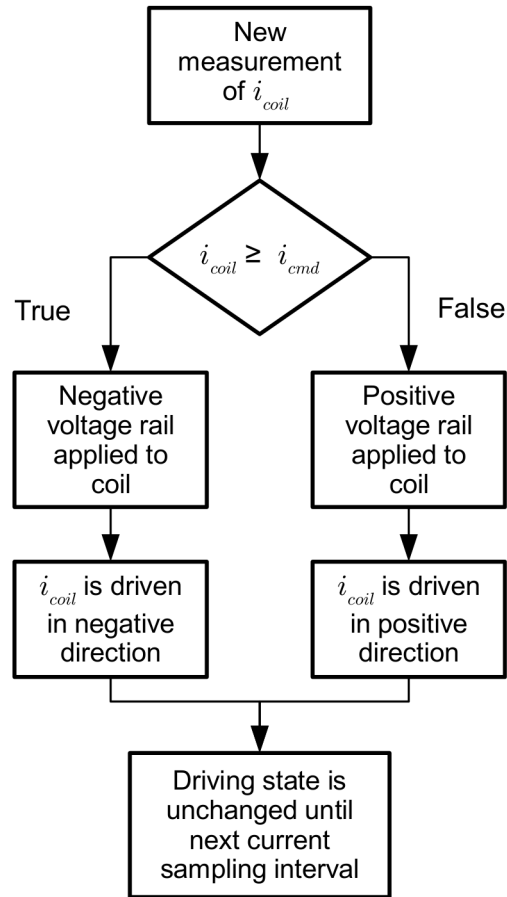


Figure 6.9: Hysteresis current control algorithm

The current control is an underlying or “inner” control loop and is executed more frequently than the “outer” PID position control loop. For this scheme to work, the dynamics of associated with the underlying control loop need to be faster than that of the position control. Section 7.4 investigates the cooperation between the underlying current control and PID position control loops for the UIFESS design.

Chapter 7

Single Axis Single Bearing Test Setup

7.1 Purpose and Introduction

A single axis single bearing (SASB) test setup was created to help develop, test, and improve the AMB control software and hardware used for the SB and SLFBM systems. The SASB test setup intentionally emulates the SASB model described in Section 5.6. The SASB model contains the essential control challenges while offering a simple construction and efficient means to perform numerous experimental tests. The SASB test setup served as an intermediate step between the simulation and implementation of the more complex SB and SLFBM systems.

A description of the physical apparatus of the SASB test setup is given in the following section. The PID controller design for the SASB test setup is described in Section 7.3. The PID controller design is then evaluated in simulation using a Simulink model in Section 7.4.

A description of the hardware and software implementation for the SASB test setup is found in Sections 7.6 and 7.7, respectively. Control performance data of the SASB test setup is compared to the results from the Simulink simulation in Section 7.8.

Sections 7.5 and 7.9 describe necessary adaptations to the UIFESS control scheme that were discovered during SASB testing. These adaptations are in the form of additional filtering (Section 7.5) and prevention of integral windup (Section 7.9).

7.2 Test Setup Description

The SASB test setup is depicted in Figure (7.1). As in the SASB model, the setup contains a “U” shaped iron electromagnet with an iron bar flotor. The “U” electromagnet is oriented to impose an attractive magnetic force on the flotor against the force of

gravity. The flotor is constrained to movement along one axis (the z-axis) and is fixed to the rails with mechanical bearings. The SASB test setup is depicted in Figure 7.1 with designations of its major components.

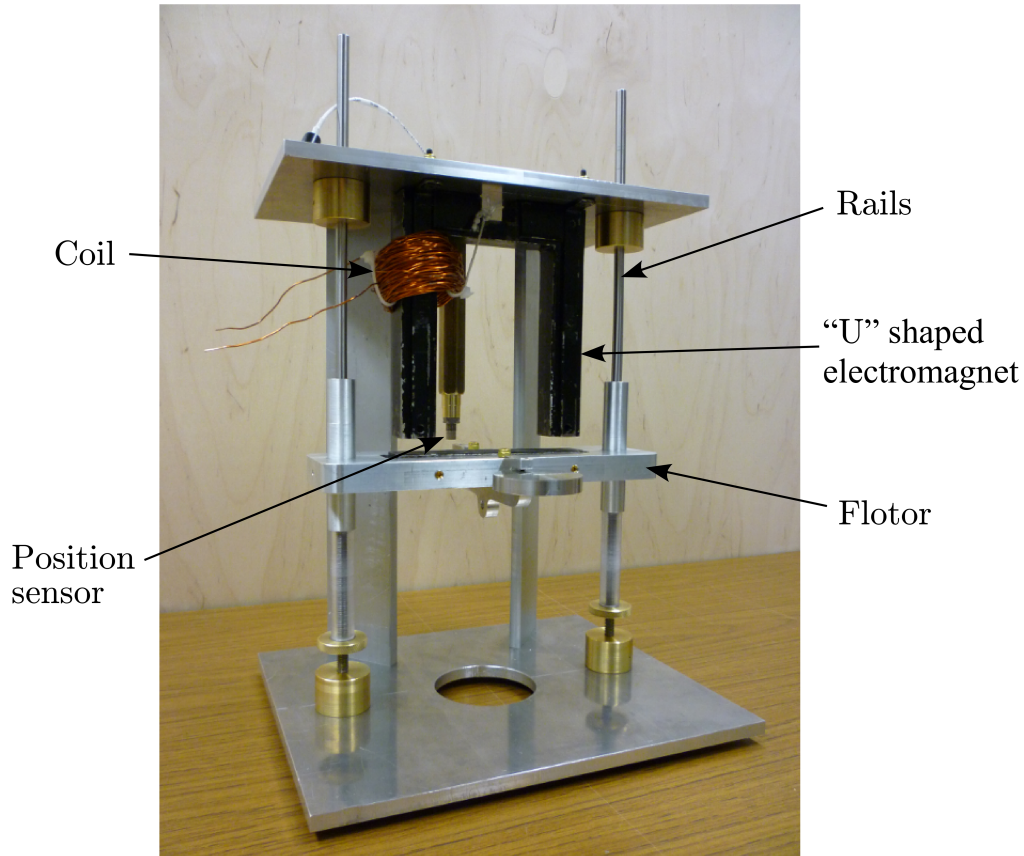


Figure 7.1: SASB test setup

Although the flotor is not fully suspended, the friction between the mechanical bearings and the rail is minimal and is neglected. The mechanical bearings are not load bearing and merely serve to prevent movement along other axes. Since the majority of the force is along the z-axis, the resulting friction caused by the rails is small.

A single position sensor is used to measure the air gap. The position sensor information is fed back to the PID position controller at a sampling rate of 10 kHz. The PID position control algorithm is then executed at each 10 kHz sampling interval, delivering a current command to the hysteresis current controller. Using information from the current sensor, which is sampled at 80 kHz, the hysteresis current controller attempts to

match the current command by appropriately switching the H-bridge. Figure 7.2 shows a high-level block diagram describing the functionality of the SASB test setup.

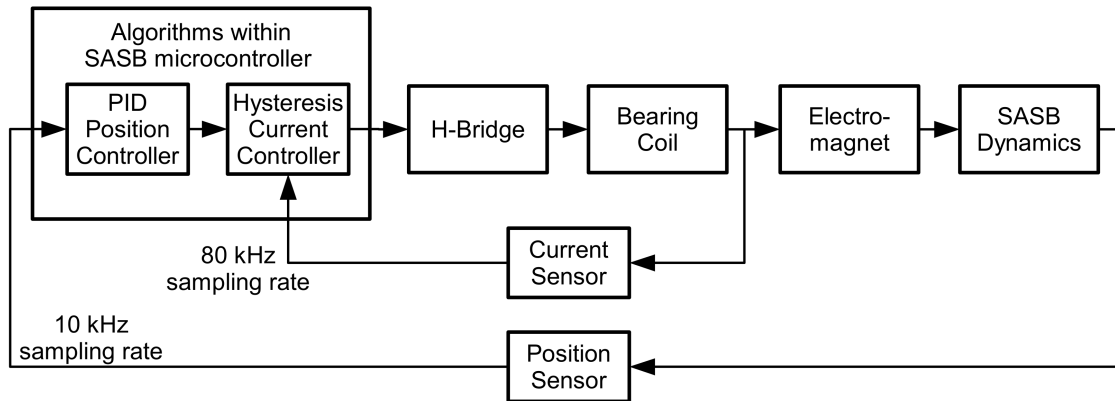


Figure 7.2: High-level block diagram of SASB functionality

7.2.1 System Parameters

Table 7.1 contains the SASB parameters. The nominal air gap is set to 1.00 mm, the same as the UIFESS air gap. The bias current was found by determining the necessary current at which the magnetic force equaled the gravitational force on the flotor at the nominal air gap. From the bias current and air gap values, the bias flux density within the air gap was calculated using (5.12). The bias force was calculated using (5.19).

Table 7.1: SASB test setup parameters

Parameter	Value
Pole Face Cross Sectional Area ($A_{PoleFace}$)	6.71 cm ²
Number of turns (N)	150
Coil Gauge	18 AWG
Nominal Air Gap (g_0)	1.00 mm
Bias Flux Density (B_{bias})	0.180 T
Bias Current (i_{bias})	1.91 A
Bias Force	17.3 N
Nominal Inductance	9.50 mH
Coil Resistance	0.800 Ω
Force/displacement Factor (k_x)	34.6 N/mm
Force/current Factor (k_i)	18.1 N/A

Although the bias flux density was calculated to be considerably less than 0.6 T, the B_{bias} value is still within the linear region of the B-H curve.

7.3 PID Controller Design for SASB Test Setup

The PID controller for the SASB test setup was designed and simulated using MATLAB Simulink. From (6.35), the SASB test setup z-domain plant is calculated as:

$$G_{z_{SASB}}(z) = 5.1321 \cdot 10^{-8} \frac{z + 1.0000}{z^2 - 2.0002z + 1.0000} \quad (7.1)$$

The poles and zeros of (7.1) are given in Table 7.2 and reveal the instability of the SASB plant due to the pole located outside of the unit circle at 1.0141. The instability is expected, since the instabilities present in the s-domain SASB plant from (6.8) are now represented in the z-domain.

Table 7.2: Poles and zeros of SASB plant

	Location
Pole 1	1.0141
Pole 2	0.9861
Zero 1	-1.0000

The *pidtool* command in MATLAB evokes a “PID Tuner” tool that provides a step response tuning tool to appropriately set the K_P , K_I , and K_D gains as well as the derivative filter term T_D . The “PID Tuner” tool calculates settling time, rise time, overshoot, bandwidth, gain margin, and phase margin for a particular plant and PID design. The tool allows the user to tweak various parameters and instantaneously view the resulting step response.

Utilizing the “PID Tuner” tool to design and visualize the SASB PID response, the PID parameters were set to achieve the following conditions:

- **A “small” value for K_D .** As previously described in Section 6.8, the nature of the derivative term and its practical realization is extremely sensitive to high frequency noise. Even with the aid of the first order filter in (6.17), the derivative of high frequency signals can produce large values. The undesirable effects of this phenomenon becomes less prominent if the gain associated with the derivative action, i.e. K_D , is minimized. Therefore, the smallest value for K_D is chosen such that the other design constraints are satisfied.
- **An open loop phase margin of 60° .** A 60° open loop phase margin provides a good balance between system stability and performance. Additional phase lag due to microcontroller calculation time and filtering (see Section 7.5) is expected, thus, a 60° phase margin will provide sufficient margin such that the additional phase lag does not threaten system stability.
- **Correspond with underlying current control.** The response speed of the PID position controller could not be set higher than the response capability of the underlying current controller. The Simulink model described in Section 7.4 was used to match the response speeds of the two controllers to ensure good performance.
- **No greater than 25% overshoot in the step response.** This condition was only set as an upper bound for testing purposes. The 25% overshoot upper bound was arrived at ad hoc for the SASB test setup as a balance between performance and achieving a “small” value for K_D .
- **No oscillations in the step response.** Oscillations in the control system were avoided to prevent the possibility of exciting resonant frequencies elsewhere in the system.

It is important to note that these conditions were selected to allow testing of the SASB test setup and were believed to be conservative. The most important goal of the SASB

test setup was to enable the development of the hardware and software systems. Therefore, these conditions are not intended to optimize the performance of the SASB test setup, only to allow it to serve as a working testbed.

Obeying the conditions above, the summary of the PID controller parameters and expected closed loop performance of the system is given in Table 7.3. From Table 7.3, the settling time is the time the response reaches 2% of the steady state value. The rise time is the time the response takes to rise from 10% to 90% of the steady state value. The K_P , K_I , K_D , and T_D parameters given in Table 7.3 are utilized in the PID controller developed in (6.21):

$$C_{d_{SASB}}(z) = K_P + K_I \frac{T_s z + 1}{2 z - 1} + K_D \frac{1}{T_D + \frac{T_s z + 1}{2 z - 1}} \quad (7.2)$$

Closing the loop with the addition of the PID controller, as shown in Figure 6.8, stabilizes the SASB plant. The poles and zeros of the closed loop system are shown in Figure 7.3 and explicitly given in Table 7.4. Since all poles lie inside the unit circle, the closed loop system is stable.

Table 7.3: SASB PID position controller parameters

PID Controller Parameters		Closed Loop Performance	
Parameter	Value	Metric	Value
K_P	$2.041 \cdot 10^4$	Settling Time	181 ms
K_I	$1.688 \cdot 10^5$	Rise Time	1.20 ms
K_D	93.61	Percent Overshoot	20.2%
T_D	$2.787 \cdot 10^{-4}$	Phase Margin	60.0°
f_D	571.0 Hz		
T_s	0.100 ms		

In order to predict the actual SASB test setup system response, a SASB Simulink model is developed in Section 7.4. The SASB Simulink model includes the bearing coil dynamics and magnetic force nonlinearities, and will provide a testbed for verifying the SASB controller design with the aforementioned inclusions.

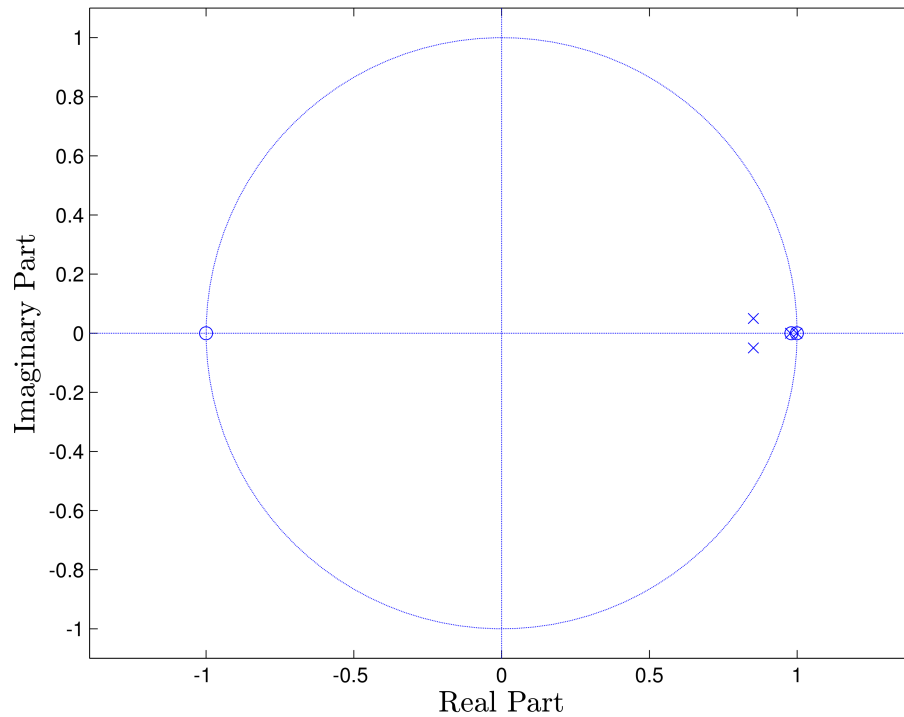


Figure 7.3: Pole-zero plot of the closed loop SASB system

7.4 SASB Simulink Model

As previously discussed, the PID controller design in the previous section was performed under the following assumptions:

- A linearized, small signal SASB system plant.
- Instantaneous current response within the bearing coil. As a result, the bearing coil dynamics and the underlying current control loop were not considered.

Although these assumptions are essential for the purpose of the PID controller design, in practice, however, the assumptions do not hold. The linearized, small signal SASB is a linear approximation of a nonlinear system about the operating (i.e., bias) point and only represents a portion of the total signal. In addition, the bearing coil dynamics limit the speed at which the coil current can change and will impact the SASB system response.

Table 7.4: Poles and zeros of closed loop SASB system

	Location
Pole 1	0.9990
Pole 2	0.9775
Poles 3,4	$0.8519 \pm 0.0497j$
Zero 1	-1.0000
Zero 2	0.9991
Zero 3	0.9804

To verify the performance of the PID controller while considering these issues, a SASB Simulink model was developed. The SASB Simulink model includes the magnetic force nonlinearities of the SASB system from (5.35) along with bearing coil dynamics from (5.36). The SASB Simulink model provides a more realistic testbed for the PID controller design and helps evaluate its performance in conjunction with the underlying current control loop.

The Simulink model can be divided into three interconnected subsystems: the PID position control, the underlying current control and bearing coil dynamics, and the plant dynamics, and are depicted in Figures 7.4, 7.5, and 7.6, respectively.

The PID and current controller Simulink blocks are sampled and calculated at 10 kHz and 80 kHz rates, respectively, simulating the digital sampling time delays and ZOH behavior that will exist during implementation. The coil and plant dynamics, which are analog systems, are simulated in continuous time. Therefore, the SASB Simulink model appropriately models the interaction between the digital control and the analog dynamics.

Figure 7.7 shows the SASB air gap response to an input step change from 1.00 mm to 1.10 mm. To compare the expected performance to the simulated performance, the settling time, rise time, and percent overshoot are measured for the response in Figure 7.7 and are given in Table 7.5.

The discrepancies between the expected and simulated air gap response are mainly due to the inclusion of the magnetic force nonlinearities. Although the simulated result

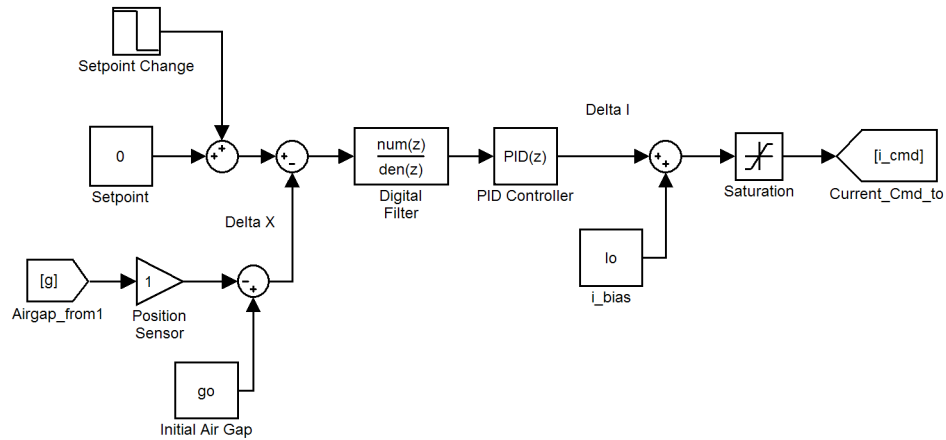


Figure 7.4: PID position control subsystem from SASB Simulink model

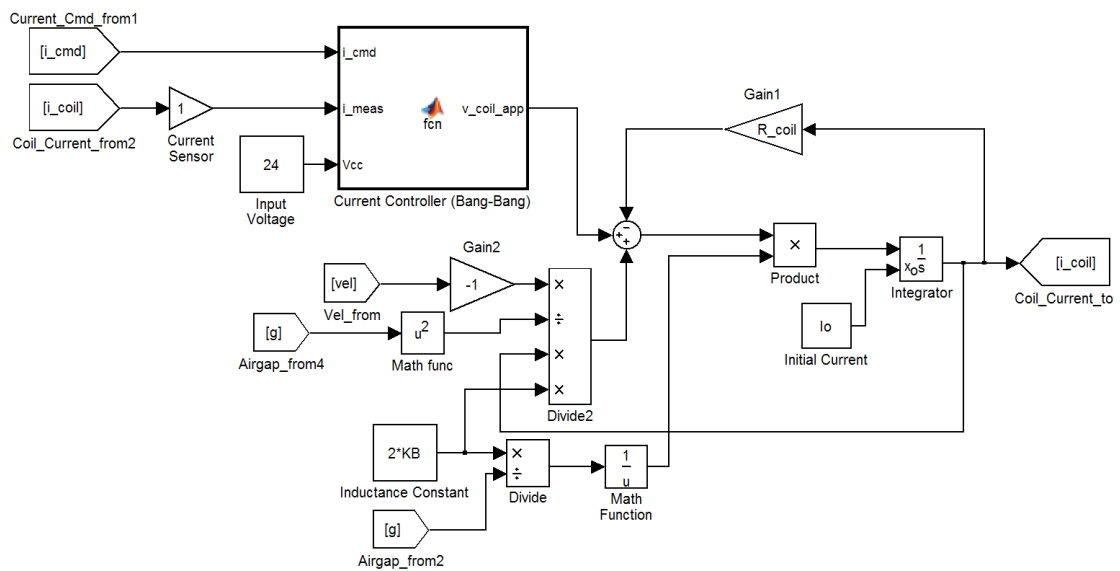


Figure 7.5: Current control and coil dynamics subsystem from SASB Simulink model

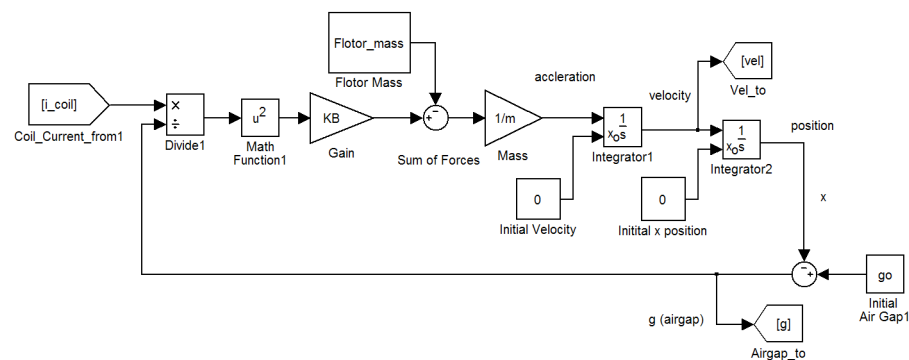


Figure 7.6: Plant dynamics subsystem from SASB Simulink model

Table 7.5: Performance of SASB air gap response simulation

Metric	Value
Setting Time	204 ms
Rise Time	6.40 ms
Percent Overshoot	13.3%

is a slower response, the overshoot of the response is 13.3%, and is well below the maximum value. In addition, no oscillations are present in the response as initially desired. Therefore, the simulated result for the air gap response was deemed acceptable.

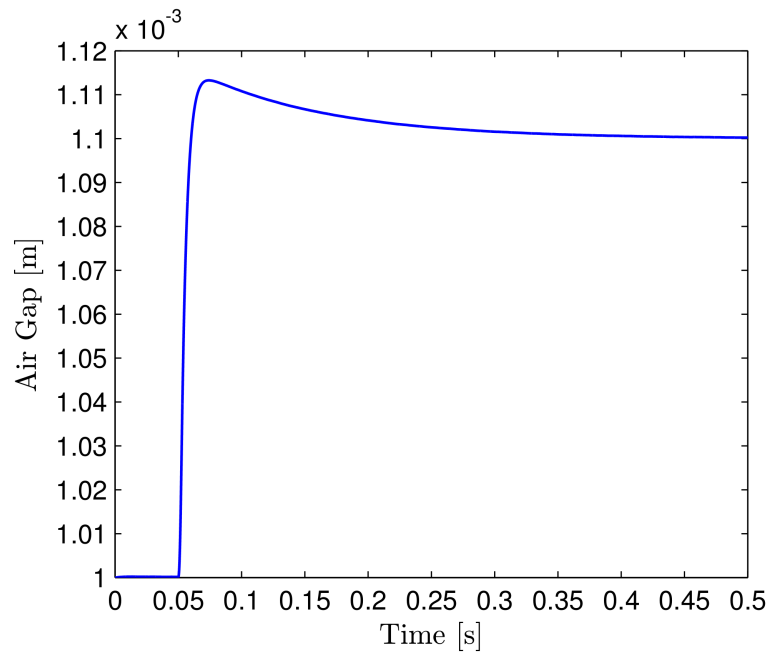


Figure 7.7: SASB air gap response to input step change

Figure 7.8 shows the coil current response to the same input step change as Figure 7.7. Zooming in to a portion of Figure 7.8, Figure 7.9 reveals the switching behavior of the underlying current controller (in green) as it attempts to match the current command set by the PID position controller (in blue).

The SASB Simulink simulations helped verify the small signal PID design and its behavior along with the coil dynamics.

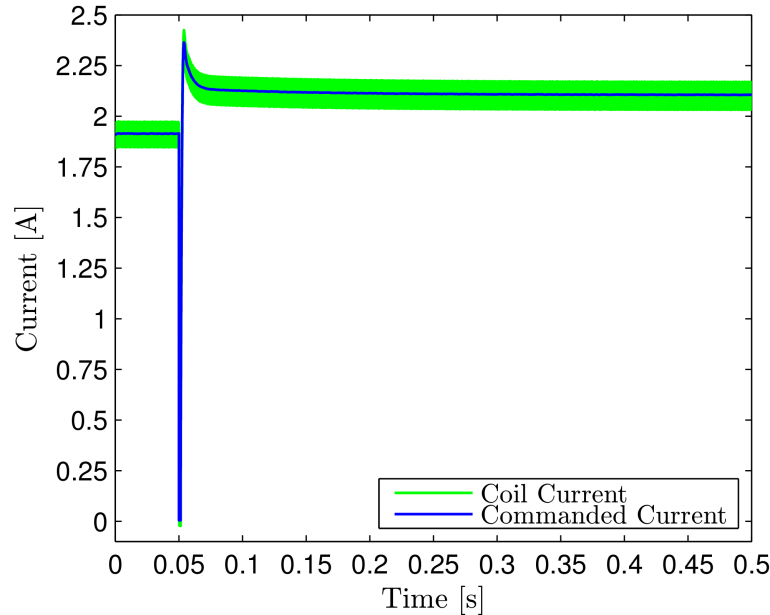


Figure 7.8: SASB coil current response to input step change

7.5 Digital Filter

To aid in the attenuation of high frequency noise, an additional digital filter was placed at the input of the PID position controller as seen in Figure (7.4). Placing a filter at the input to a PID controller or similar SISO controller is a common practice to further reduce high frequency noise and, for high speed magnetic bearing systems, to avoid destabilization of high frequency (i.e., flexible) system modes [1].

However, gain reduction at higher frequencies results in phase reduction at lower frequencies. In turn, the phase reduction lowers the open loop phase margin and reduces the relative stability of the system. Therefore, the filter poles must be chosen appropriately to avoid excessive reduction of the phase margin while providing adequate high frequency attenuation.

A digital Butterworth filter was implemented due to its simplicity and maximally flat pass-band. The digital Butterworth is an infinite impulse response (IIR) filter and is computationally more efficient than a non-recursive finite impulse response (FIR)

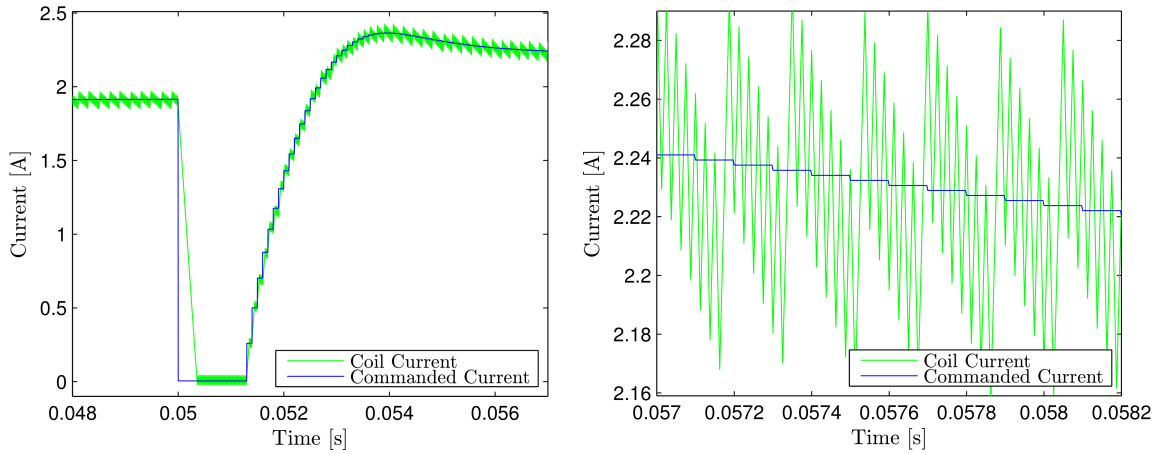


Figure 7.9: Zoomed in SASB coil current response to input step change showing current controller switching

filter of the same order. A 2nd order digital Butterworth filter with a cutoff frequency of 1.5 kHz was designed using the MATLAB command *butter*. The z-domain transfer function for the filter is given as:

$$F_{d_{filter}}(z) = \frac{Y_{f_{out}}}{X_{f_{in}}} = \frac{b_0 + b_1z^{-1} + b_2z^{-2}}{1 + a_1z^{-1} + a_2z^{-2}} \quad (7.3)$$

with the coefficients given in Table 7.6. In turn, the discrete difference equation of (7.3) is:

$$y_{f_{out}}(k) = b_0x_{f_{in}}(k) + b_1x_{f_{in}}(k-1) + b_2x_{f_{in}}(k-2) - a_1y_{f_{out}}(k-1) - a_2y_{f_{out}}(k-2) \quad (7.4)$$

Table 7.6: Filter parameters for 2nd order digital Butterworth filter with 1.5 kHz cutoff frequency

Filter Coefficient	Value
a_1	-0.7478
a_2	0.2722
b_0	0.1311
b_1	0.2622
b_2	0.1311

The Bode plots in Figure 7.10 show the effect of the digital filter. The magnitude plot in Figure 7.10 shows the digital filter reducing the gain of the PID controller at high frequencies. However, as seen in the phase plot of Figure 7.10, the filter adds additional phase lag. In turn, this reduces the phase margin from 60.0° to 50.2° . Although the resulting 50.2° phase margin is still an acceptably high value, the necessity of the filter is analyzed in Section 7.8 to determine whether or not it should be used in the final design.

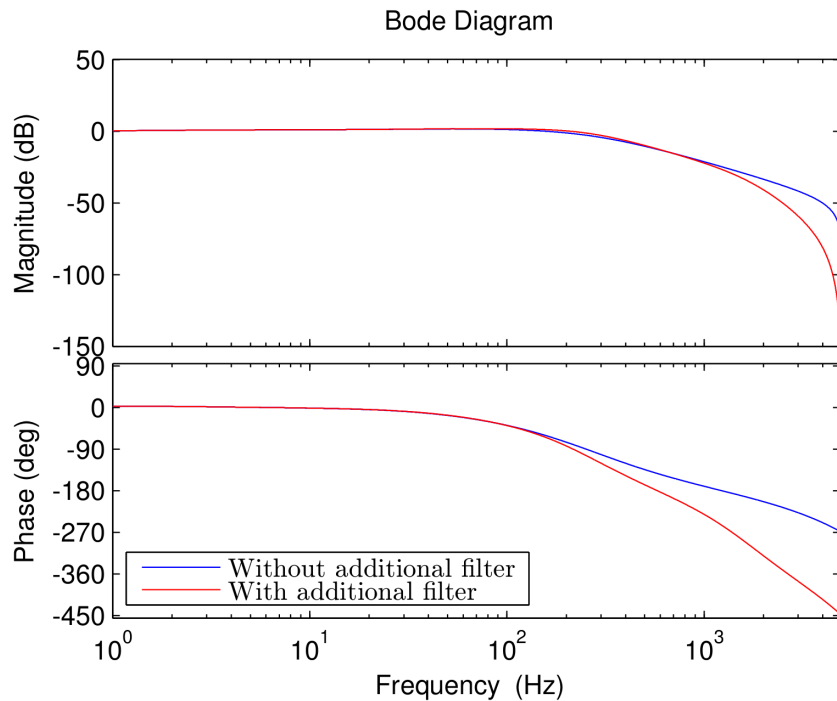


Figure 7.10: Bode plots comparing PID controller frequency response with and without the additional digital filter

7.6 SASB Hardware Implementation

The SASB hardware setup is summarized in Figure 7.11. The UIFESS printed circuit board (PCB) is a custom PCB designed by Kevin Ramus that contains the Pololu motor driver and sensor signal conditioning circuitry. The sensor signal conditioning is responsible for scaling the position and current sensor signals to the input voltage range

of the ADC pins on the MCU. The sensor signal conditioning also contains anti-aliasing low pass filters.

The Pololu motor driver is an off-the-shelf PCB that contains the H-bridge coil driver and current sensor. The MCU output pins control the switching state of the H-bridge coil driver. The Kaman 2306 is an eddy current displacement sensor. For more information, a highly detailed description of the SASB test setup hardware is given in [16].

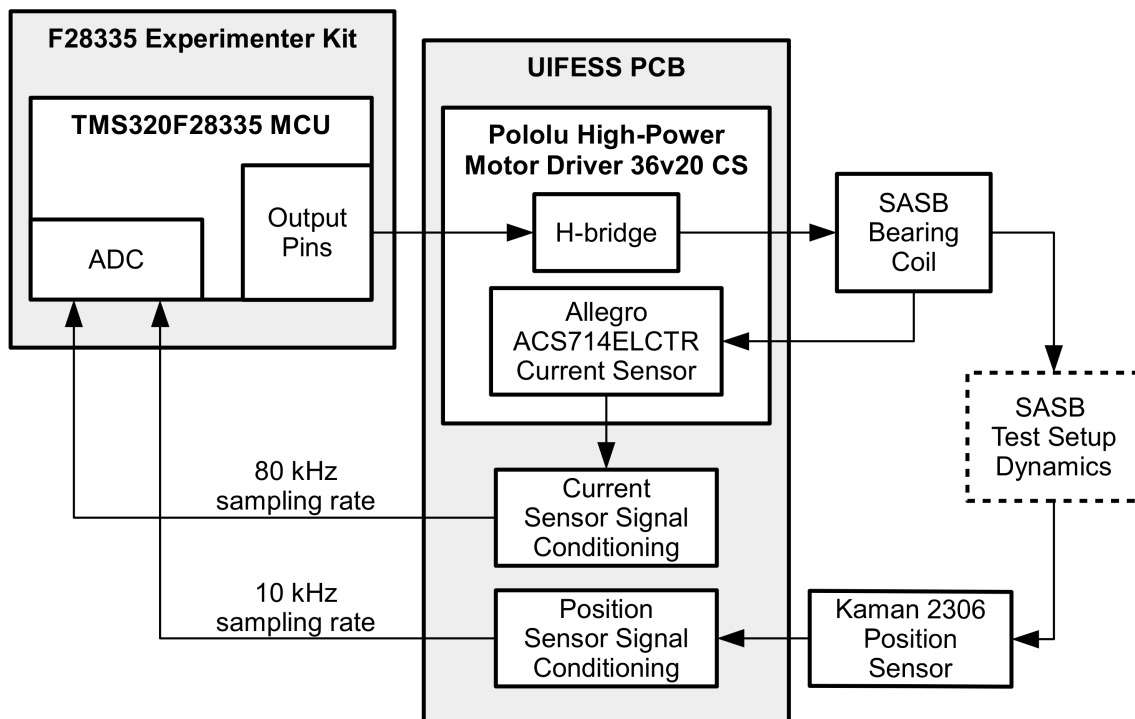


Figure 7.11: Top level SASB hardware diagram

7.7 SASB Software Implementation

The control software was written in the C programming language. The control software was compiled and downloaded into the MCU using Code Composer Studio (v5.5), an Integrated Development Environment (IDE) provided by Texas Instruments.

The control software is required to perform the following tasks:

1. Read the position and current sensor measurements.
2. Execute the PID position controller and hysteresis current controller algorithms.
3. Provide commands to the power electronics to enact the proper control for the SASB system.

The time delay between steps 1 and 3 must be kept to a minimum. The time delay introduces a phase lag in the control system which can degrade the performance of the control system and exhibit negative effects on the stability of the overall SASB system. Therefore, special attention was placed on writing fast, efficient code. Figure 7.12 outlines the top level of the control software structure.

7.8 Control Performance

In order to verify the performance of the SASB test setup, the response to a commanded step change was compared to the SASB Simulink model. An oscilloscope was used to capture the position and current sensors during the step change. The oscilloscope utilized is capable of 40 MSamples/sec and is located on the Electronics Explorer Board by Digilent. As simulated in Figure 7.7, a 1.00 mm to 1.10 mm step change was performed on the SASB test setup.

Figure 7.13 compares the air gap response of the SASB test setup with that of the SASB simulation from Section 7.4. The actual and simulated air gap responses are in close agreement, although the overshoot of the actual response is slightly larger at 17%.

Figure 7.14 compares the coil current response of the SASB test setup with that of the SASB simulation from Section 7.4. The simulated coil current response from Figure 7.8 has been superimposed onto the actual coil current response for comparison. The SASB test setup requires additional bias current to overcome the reluctance of the iron, which was neglected during the simulation. However, the additional bias current raises the bias flux within the air gap from the calculated value of 0.18 T to around

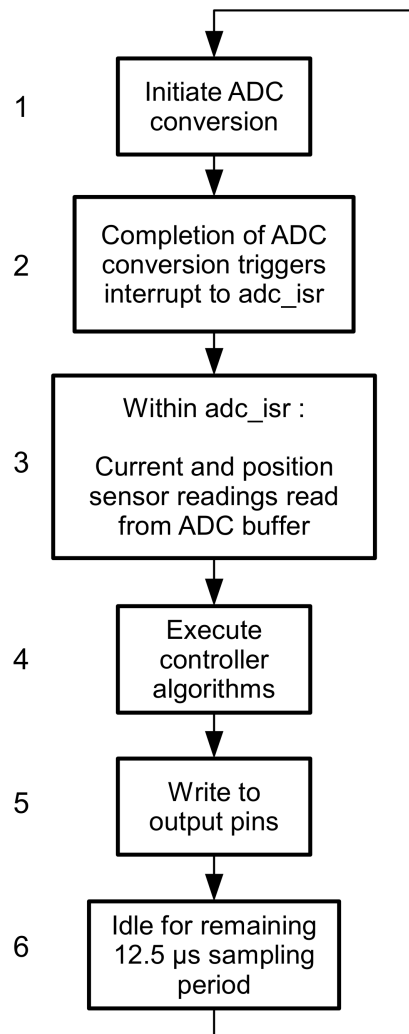


Figure 7.12: Top level SASB software flow chart

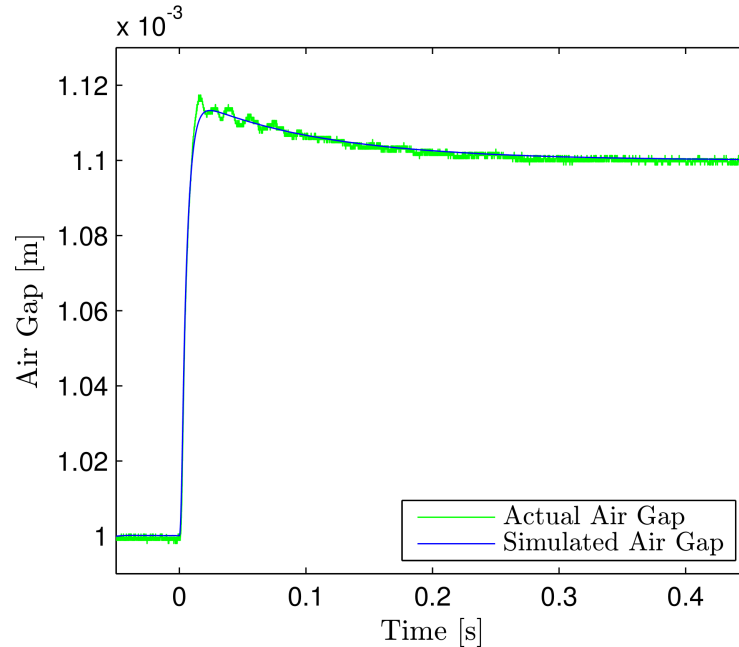


Figure 7.13: Actual vs. simulated air gap response to step change

0.2 T, and therefore the iron operation point is still within the linear region of the B-H curve. Despite the inconsistency between actual and simulated coil bias current, the small signal current response is in close agreement when an artificial offset of 0.6 A is added to the simulated current response.

As described in Section 7.5, the SASB simulation features a digital filter which is placed in series with the PID controller. Although the filter provides attenuation to high frequency noise, the filter adds additional computation time. In addition, the digital filter also adds phase delay, which reduces the phase margin from 60.0° to 50.2° and decreases the relative stability of the overall system. The necessity of the digital filter was analyzed by completely removing the filter from the control scheme and observing the response to an identical step change to Figures 7.13 and 7.14. Figure 7.15 gives the air gap response, Figure 7.16 gives the coil current response.

Without the digital filter, the overshoot in Figure 7.15 becomes 20%. In addition, the switching and maximum error bounds of the coil current have increased. For these reasons, the digital filter remained within the control system design despite the trade

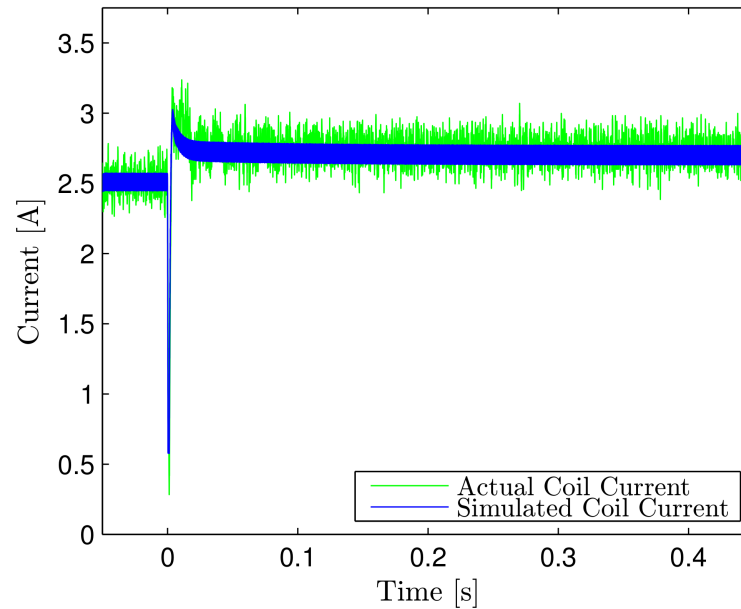


Figure 7.14: Actual vs. simulated coil current response to step change

offs of reduced phase margin and additional computation time. However, the effects of the 60.0° to 50.2° phase margin reduction and additional computation time are minimal, reaffirming the choice to include the digital filter.

7.9 Integral Windup Prevention for PID Controller

During the testing of the SASB test setup, undesirable behavior that is characteristic of integral windup was observed. Integral windup occurs when the integral action of the PID controller, which is essentially a running summation of the error signal, becomes large and exhibits excessive resistance to quick changes in the error signal. In turn, the integral action dominates the behavior of the PID controller due to its large value and hinders the overall controller response.

In order for the integral summation to “wind-down,” the error signal must change sign for a significant period of time. The consequence of this behavior is large overshoot and results in the control signal changing from one extreme to the other. In the case of

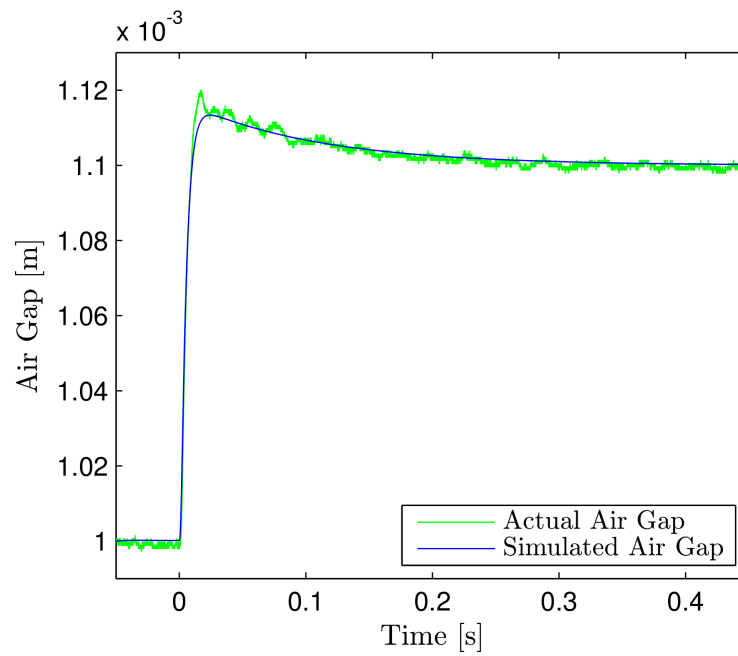


Figure 7.15: Actual vs. simulated air gap response to step change without additional digital filter

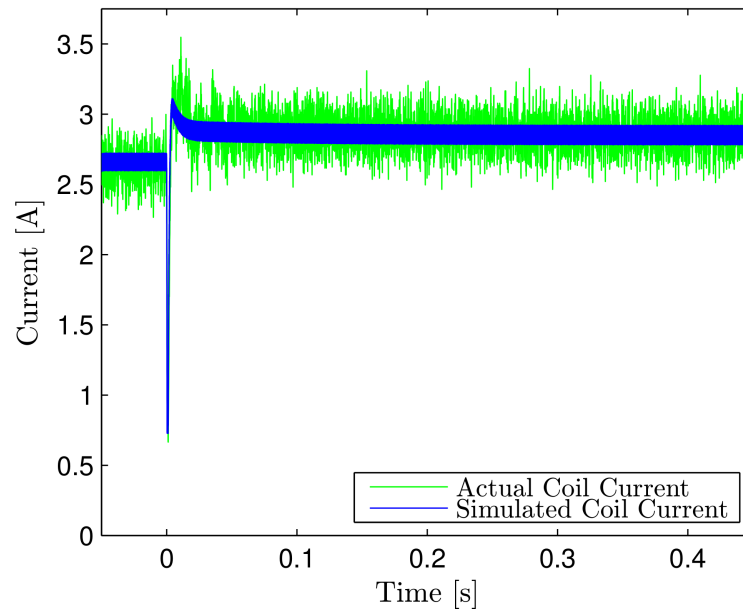


Figure 7.16: Actual vs. simulated coil current response to step change without additional digital filter

the SASB test setup, the flotor would “bounce” between crashing into the bearing and being completely unsupported.

In order to correct this issue, the integral summation is reset when the error signal falls outside of a set range. During the time when the error signal remains outside of the specified range, the integral term is latched in a constant state of reset and a PD control algorithm is adopted. Figure 7.17 describes this strategy. A similar strategy is

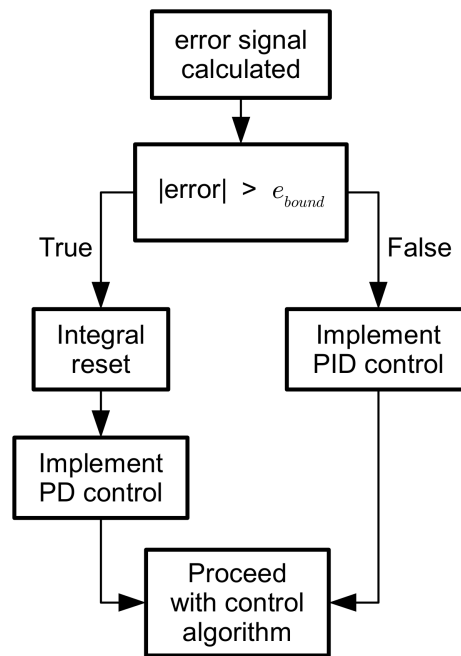


Figure 7.17: PD and PID control strategy to prevent integral windup

implemented in [41]. Setting e_{bound} to 0.50 mm, the algorithm described in Figure 7.17 prevents the “bouncing” behavior and allows the SASB test setup to react more quickly to large deviations from its nominal air gap of 1.00 mm.

7.10 Conclusion

The correlation between the simulation and actual data from the SASB test setup provided confidence in the modeling, simulation, and implementation of a simple magnetic bearing system. In turn, the concepts and experience gained from the SASB test setup

were applied to the SB and SLFBM, which utilize the SADB model. The SADB model is very similar to the SASB model, and from the standpoint of implementation, requires minimal adaptation from the SASB test setup.

Chapter 8

Stabilization Bearing Design

8.1 Introduction

This chapter describes a number of topics surrounding the Stabilization Bearing (SB). The motivation and purpose for the SB is described in Section 8.2. The design of the SB is described in two decoupled design phases. The first design phase, described in Section 8.3, sets the SB lamination geometry in order to achieve the largest amount of magnetic force possible per lamination. The second design phase, described in Section 8.4, sets the SB and spacer lengths in order to achieve sufficient restoring moments and a stable MOI ratio for the rotor.

FEA is performed on the SB lamination design to verify the expected force output and susceptibility to magnetic saturation. Results from the FEA are given in Section 8.6. The PID controller design for the SB is given in Section 8.8. Similar to the SASB test setup, a Simulink simulation is utilized to evaluate the SB PID controller design. The Simulink simulation is described in Section 8.9.

The implementation of the SB is described in Sections 8.10 through 8.12. Finally, control performance data from the SB is compared with Simulink simulation results in Section 8.13.

8.2 Theory of Operation

As described in Section 1.3, two magnetic bearing systems are used to maintain the radial air gap distance within the University of Idaho's FES system (UIFESS). Together, the two magnetic bearing sections provide forces in two x-y planes, located at two different heights on the z-axis. The top magnetic bearing system is a dedicated AMB, and is designated as the Stabilization Bearing (SB). The bottom magnetic bearing system is

integrated within the operation of the FRRM and is designated as the Self-Bearing Machine (SLFBM). Both magnetic bearing systems correct radial air gap imbalance within their respective x-y planes and work together to perform corrective moments about the x and y axes.

In some applications, the magnetic bearing design is performed alongside the apparatus it will eventually support, e.g. a rotating machine. This provides the greatest flexibility in setting the magnetic bearing geometry to achieve the best performance. In other situations, the magnetic bearing is added to an existing design to add additional support or replace a conventional contact bearing. In this case, the magnetic bearing must conform to the existing design space. The SB design for the UIFESS fits into the second category, many of the SB design constraints were already in place.

The original UIFESS design did not include a dedicated AMB, the SLFBM solely provided the radial forces for air gap control. The original design relied upon the passive HTS bearing to prevent rotor tilt. However, it was determined that the passive HTS bearing would not adequately provide this function, and a dedicated AMB, referred to as the SB, was added.

As an addition to the UIFESS, the SB design needed to conform to the physical dimensions imposed by the existing UIFESS design. These dimensions are outlined in Table 8.1 and depicted in Figure 8.3.

Table 8.1: SB design constraints

Parameter	Value
Rotor outer radius (r_{ro})	3.75 in
Hub radius (r_{hub})	0.50 in
Air gap distance (g_0)	1.00 mm
SB stator radius (r_{stator})	2.62 in

In addition to the constraints on physical dimensions, the incorporation of the SB into the UIFESS had to fulfill the following criteria:

1. The SB must be capable of producing a sufficiently large restoring moment on the rotor.
2. The addition of the SB must result in a stable I_z/I_x moment of inertia (MOI) ratio of the rotor.

To meet the above criteria and constraints, the incorporation of the SB into the UIFESS was performed in two design phases.

The first phase is the SB lamination geometry design. The goal of this phase is to optimize the physical geometry of the SB lamination to produce the largest amount of magnetic force per lamination. In turn, the SB lamination optimization results in the largest force-per-length SB design possible, making the most efficient use of the iron to produce force. The first design phase is described in Section 8.3.

The second phase is ensuring rotor stability. This phase involves an iterative process to set the SB and spacer length to achieve an acceptable MOI ratio and sufficiently large SB moment. The second design phase is described in Section 8.4. Additional design constraints were imposed for this phase, which are also described in Section 8.4.

8.3 Stabilization Bearing Lamination Geometry

The force output of a magnetic bearing is strongly dependent on the magnetic bearing geometry. The dependency is apparent from the bearing magnetic force equation (subsequently given in (8.2)), which is proportional to the cross sectional area $A_{PoleFace}$ and to the square of the number of turns N . In turn, $A_{PoleFace}$ and N depend on the SB lamination geometry, which is investigated in this section to maximize the magnetic force output.

The eight-pole design shown in Figure 8.1 is a common geometry for radial AMBs. The main advantage of an eight-pole design is the ability to decouple its magnetic forces into two orthogonal axes. Two pole pairs can be assigned to each Cartesian axis, i.e.

two pole pairs for the x axis and two pole pairs for the y axis. This resolves the bearing forces into two orthogonal directions. Any force vector needed for air gap correction within the x-y plane can be created by a combination of x and y bearing forces.

The ability to resolve forces into two Cartesian axes makes the eight-pole design well suited for decentralized control. With the placement of position sensors along the same two Cartesian axes, a local PID control scheme can correct for position deviations along each axis. Each Cartesian axes is modeled by a separate SADB model. In turn, the local PID controller is designed from the SADB plant.

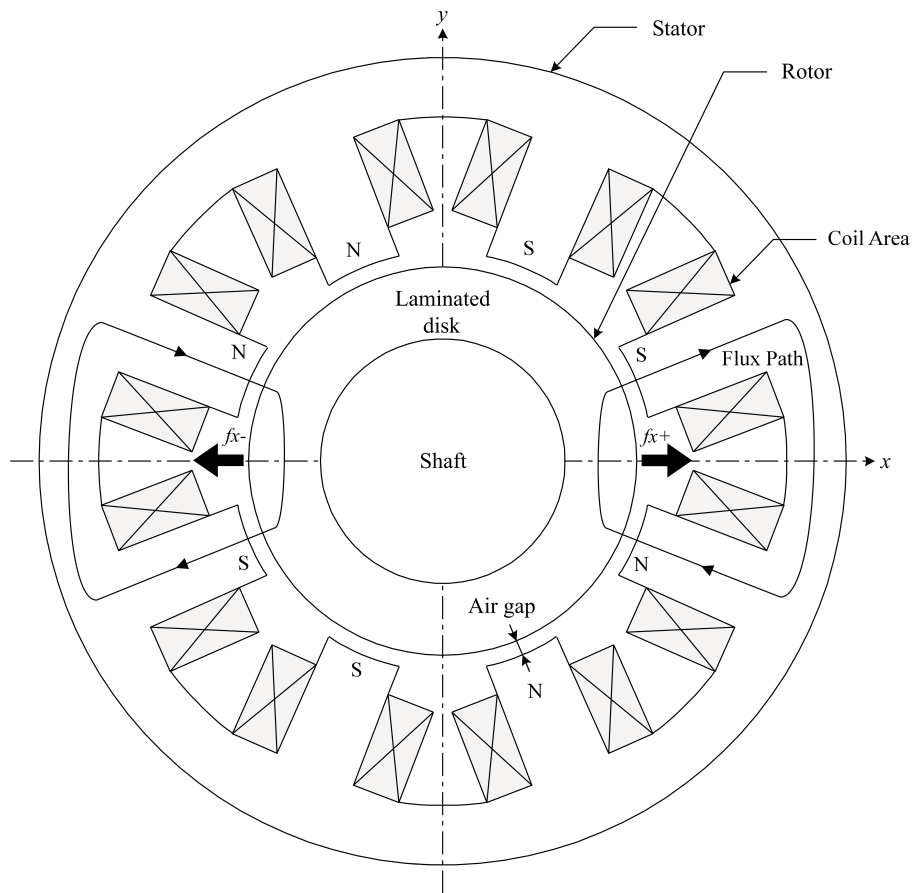


Figure 8.1: Eight pole magnetic bearing cross section, from [33]

The bearing geometry in Figure 8.1 is used for a typical machine design, where the rotor is located inside the stator. The UIFESS employs an inside-out design, where the rotor is located on the outside of the stator. Therefore, the magnet geometry in

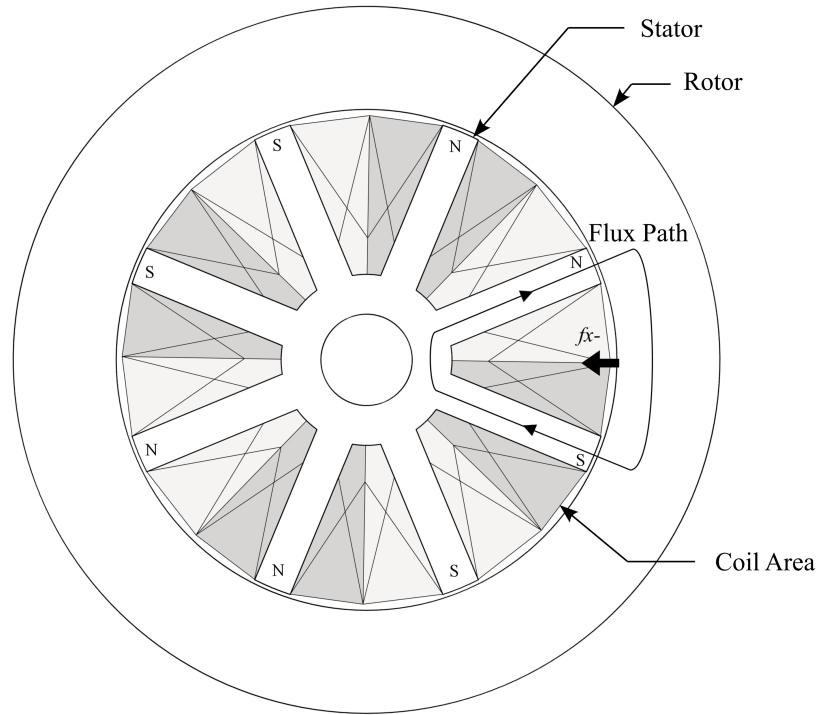


Figure 8.2: UIFESS inside-out eight pole magnetic bearing cross section

Figure 8.2 is utilized for the SB. The SB pictured in Figure 8.2 operates identically to the typical bearing geometry in Figure 8.1, by assigning two pole pairs to each x and y axis, resolving the forces along the x and y axes.

The flux path generated by each pole pair is shown in Figure 8.2. Following a similar derivation to Section 5.2, (8.1) gives the air gap flux density for each pole pair.

$$B = \mu_0 \frac{Ni}{s} \quad (8.1)$$

Note that (8.1) differs from the previously derived equation (5.12) by a factor of 1/2. For the geometry in Figure 8.2, the closed surface of Ampere's Law encircles N turns from each pole, resulting in the total enclosed turns equaling $2N$. Continuing the derivation, the attractive force for each pole pair becomes:

$$f = \frac{B^2 A_{PoleFace}}{\mu_0} = \left(\mu_0 \frac{Ni}{s} \right)^2 \frac{A_{PoleFace}}{\mu_0} = \mu_0 N^2 A_{PoleFace} \left(\frac{i}{s} \right)^2 \quad (8.2)$$

where

- $A_{PoleFace}$ is the cross sectional area of the pole face.
- N is the number of turns per pole.
- i is the current in the coils.
- s is the air gap distance.
- μ_0 is the permeability of free space.

The cross sectional area of the pole face $A_{PoleFace}$ is equal to

$$A_{PoleFace} = l_{SB}W_{pole} \quad (8.3)$$

where l_{SB} is the length of the SB bearing and W_{pole} is the width of the pole face. From (8.2), the force of a pole pair is thus proportional to both l_{SB} and W_{pole} .

Figure 8.3 depicts the geometric parameters of the SB laminations, including W_{pole} . The length of the SB bearing l_{SB} exists perpendicular to the plane of the page in Figure 8.3. Therefore, note that the cross sectional area of the pole face $A_{PoleFace}$ is perpendicular to the SB laminations.

Increasing l_{SB} results in a longer bearing that produces more force due to the increase in $A_{PoleFace}$. The SB length l_{SB} is set in Section 8.4, since its selection has a large effect on the rotor stability. At first it would also appear that increasing W_{pole} would also result in an increase in force. However, increasing W_{pole} decreases the available space for coil turns N , another parameter that determines bearing force. Thus, the optimum relationship between the number of coil turns and the size of W_{pole} must be reached to achieve the largest pole pair force possible.

To find the optimum relationship, bearing parameters were described in terms of θ_1 . The pole pair force relationship is then investigated over a range of θ_1 values to find

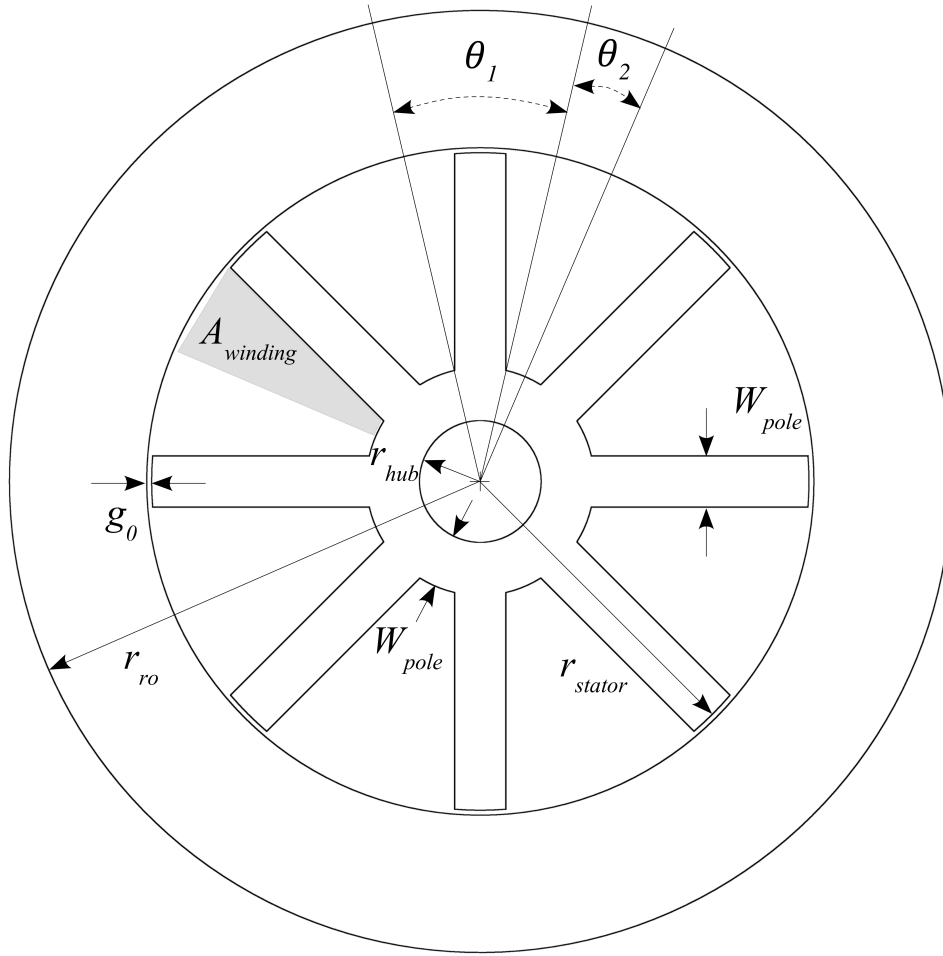


Figure 8.3: Geometric parameters of SB laminations

the value of θ_1 which results in the largest pole pair force. In turn, the optimal θ_1 value is used to set the remaining SB lamination dimensions.

To operate the bearing in a differential driving mode (as described in 5.7), the stator back iron path must be the same width as each pole tooth to avoid premature saturation. Equating the widths of the pole teeth and back iron gives the following relationship for W_{pole} :

$$\frac{W_{pole}(\theta_1)}{2} = (W_{pole}(\theta_1) + r_{hub}) \sin\left(\frac{\theta_1}{2}\right) \quad (8.4)$$

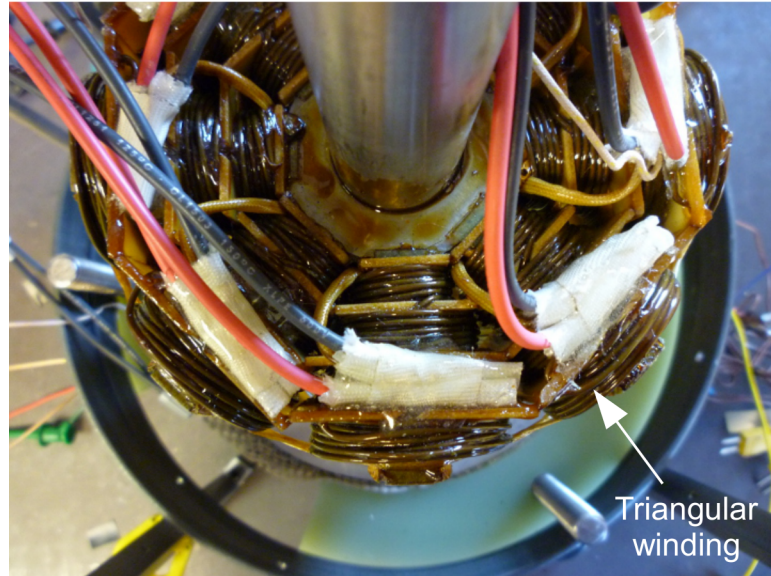


Figure 8.4: SB triangular winding

Equation (8.4) is now rearranged to find W_{pole} as a function of θ_1 :

$$W_{pole}(\theta_1) = \frac{2r_{hub}\sin\left(\frac{\theta_1}{2}\right)}{1 - 2\sin\left(\frac{\theta_1}{2}\right)} \quad (8.5)$$

In order to maximize the available winding space between pole teeth, a triangular winding shape was fit over each pole tooth. Strom Electric in Troy, Idaho, fabricated these windings, shown in Figure 8.4. The area available for coil windings $A_{winding}$ is shown in Figure 8.3 and given as:

$$A_{winding}(\theta_1) = \pi (r_{stator}^2 - r_1(\theta_1)^2) \frac{\theta_2(\theta_1)}{360^\circ} + \pi (r_{stator} - r_1(\theta_1))^2 \frac{(\theta_1/2)}{360^\circ} \quad (8.6)$$

where

$$r_1(\theta_1) = W_{pole}(\theta_1) + r_{hub} \quad (8.7)$$

$$\theta_2(\theta_1) = \frac{1}{2} \left(\frac{\pi}{4} - \theta_1 \right) \quad (8.8)$$

The maximum number of turns which fit inside $A_{winding}$ is given in (8.9). The coil fill factor k_{FF} is given in (8.10) and was determined from a triangular winding

prototype created by Strom Electric. The number of turns N is also dependent on the gauge of the coil wire, represented by the wire radius r_{wire} . In this instance r_{wire} is assumed constant. However, the wire gauge will eventually become a design parameter and dictate the number of turns in the final SB design.

$$N(\theta_1) = \frac{A_{winding}(\theta_1)k_{FF}}{\pi(r_{wire})^2} \quad (8.9)$$

$$k_{FF} = 0.281 \quad (8.10)$$

Finally, (8.3) is rewritten as a function of θ_1 :

$$A_{PoleFace}(\theta_1) = l_{SB}W_{pole}(\theta_1) \quad (8.11)$$

Equations (8.4) through (8.11) derive the geometric bearing parameters from Equation (8.2) in terms of θ_1 . The force per pole pair can now be written as a function of θ_1 in (8.12).

$$f(\theta_1) = \mu_0 N(\theta_1)^2 A_{PoleFace}(\theta_1) \left(\frac{i}{s}\right)^2 \quad (8.12)$$

By substitution of (8.9) into (8.12), the portion of (8.12) which is dependent on θ_1 is isolated as $\gamma(\theta_1)$:

$$\gamma(\theta_1) = A_{winding}(\theta_1)^2 W_{pole}(\theta_1) \quad (8.13)$$

The parameter $\gamma(\theta_1)$ describes the relationship between pole pair force and θ_1 . For a given set of parameters (i , s , l_{SB} , etc.), the largest pole pair force exists when $\gamma(\theta_1)$ is at its maximum. Figure 8.5 plots $\gamma(\theta_1)$ over the possible values for θ_1 .

Figure 8.5 shows $\gamma(\theta_1)$ is at its maximum value when θ_1 is 25.9°. With θ_1 set as 25.9°, Equations (8.4), (8.8), and (8.6) are used to calculate the SB lamination dimensions listed in Table 8.2.

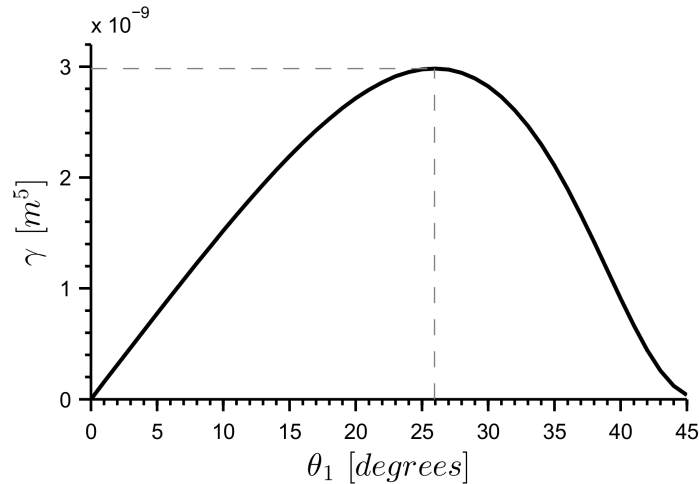
Figure 8.5: Force per SB pole pair over θ_1

Table 8.2: Calculated SB lamination design parameters

Parameter	Value
θ_1	25.9°
θ_2	9.50°
Pole width (W_{pole})	0.407 in
Winding Area ($A_{winding}$)	0.832 in ²

8.3.1 Lamination Material

The SB lamination material was chosen as M-36 grade silicon steel. There are two reasons for this selection:

1. An efficient means to obtain high quality M-36 laminations of the approximate size required was already available. The SLFBM laminations, which utilized M-36 for its laminations had been successfully fabricated to the SLFBM design specifications. Details regarding the SLFBM lamination design can be found in [17]. In short, M-36 laminations were readily available.
2. M-36 silicon steel exhibits an acceptable linear B-H relationship between 0.1 T and 1.2 T. The linear relationship is beneficial for the linear B-H approximation utilized in Section 6.3.2. The M-36 B-H relationship is shown in Figure 8.6.

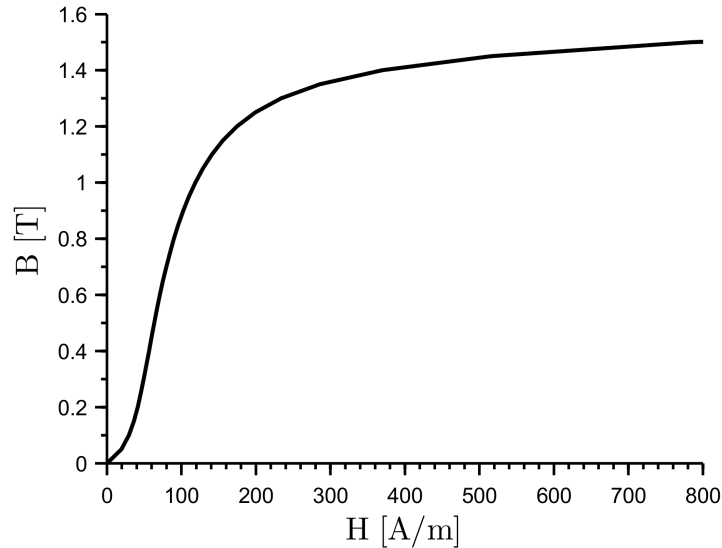


Figure 8.6: B-H curve for M-36 silicon steel

The thickness of each M-36 lamination is 0.0185 inches. The lamination thickness was dictated by the availability from the supplier, which sells M-36 sheets at a thickness of 0.0185 inches.

8.3.2 Number of Turns

The flux density within the M-36 laminations is dependent on the magnetomotive force Ni provided by the bearing coil. A larger number of turns decreases the value of current required to produce the same flux density within the laminations. Likewise, more current is required if a smaller number of turns is selected.

For a given wire radius, (8.9) calculates the number of turns which fit inside the winding area $A_{winding}$. The possible wire radii are taken from standard AWG sizes. The bias flux B_{bias} for the SB is set as 0.6 T. To select the number of turns, a relationship between the current required to maintain B_{bias} and the coil wire radius is developed.

Rearranging (8.1), the current required for a given stator tooth flux density B_{tooth} becomes:

$$i = \frac{B_{tooth}s_0}{\mu_0 N} \quad (8.14)$$

By substituting (8.9) into (8.14), a relationship between wire radius and the required current for a given B_{tooth} is found:

$$i(r_{wire}) = \frac{B_{tooth} s_0 \pi (r_{wire})^2}{\mu_0 A_{winding} k_{FF}} \quad (8.15)$$

Setting $B_{tooth} = B_{bias}$, (8.15) and (8.9) are plotted against the available sizes of r_{wire} in Figure 8.7.

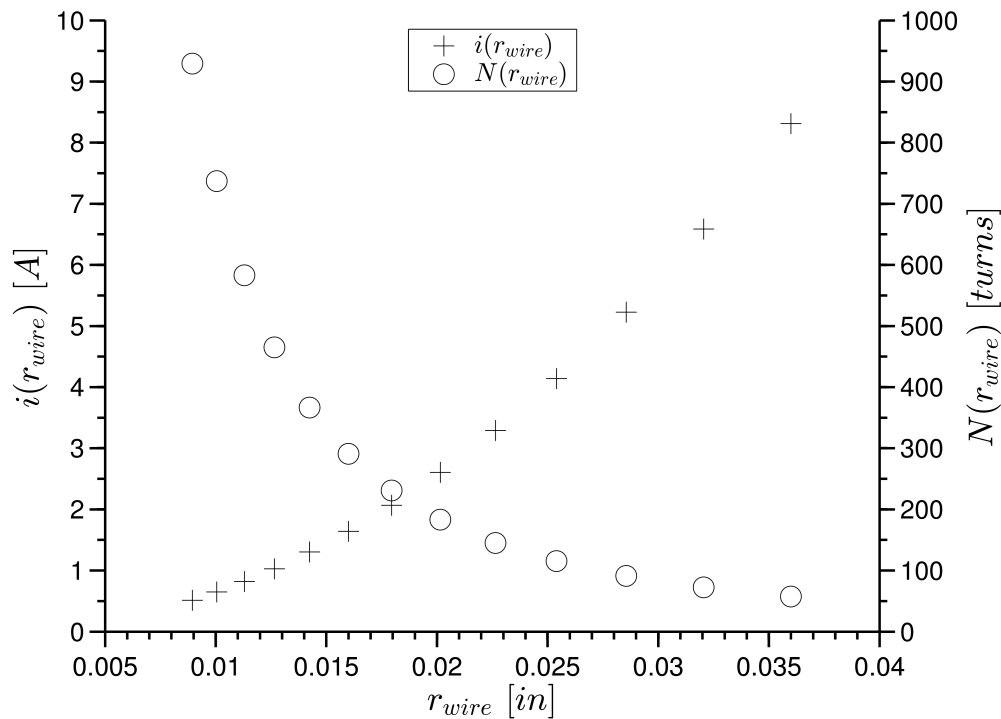


Figure 8.7: Required bias current and number of turns vs. wire radius

A wire radius of 0.02015 inches was selected, corresponding to size 18 AWG. A wire size of 18 AWG sets the bias current to 2.6 Amps and provides a reasonable force-to-current range for the SB power amplifiers and current sensors. Selecting a smaller wire radius begins to dramatically increase the required number of turns with minimal decrease in bias current. In addition, a large number of turns causes the coil fabrication to be more difficult and increases coil resistance.

8.3.3 Stabilization Bearing Coil Inductance and Resistance

The calculated values of nominal inductance and coil resistance give an estimate of the SB coil time constant for each pole pair and provide a useful design check. The nominal coil inductance and coil resistance parameters were also utilized in the SB Simulink simulations in Section 8.9 since the SB had not yet been fabricated.

Neglecting leakage inductance, (8.16) is used to calculate the nominal bearing inductance of each pole pair. The nominal bearing inductance is taken at the bias point with $g = 1.00$ mm:

$$L_{SB_{pp}} = \frac{2\mu_0 N^2 A_{cs}}{g} = 16.6 \text{ mH} \quad (8.16)$$

Although (8.16) is a function of air gap distance g and will become perturbed with respect to rotor displacement, the change in rotor displacement is assumed to be small and its effect on the inductance is neglected. Therefore, the result from (8.16) will provide an estimate of the bearing coil inductance during normal operation.

The bearing coil resistance is estimated by:

$$R_{coil} = 2R_{slot} + 2R_{end} \quad (8.17)$$

where R_{slot} and R_{end} are the slot and end resistances of each coil. The coil resistance $R_{SB_{pp}}$ of each SB pole pair is thus:

$$R_{SB_{coil}} = 2 \frac{N^2 \rho l_{slot}}{A_{winding} k_{FF}} + 2 \frac{N^2 \rho l_{end}}{A_{winding} k_{FF}} = 0.545 \Omega \quad (8.18)$$

where l_{slot} and l_{end} are the slot and end lengths and ρ is the resistivity of copper. Slot length l_{slot} is equal to 0.75 in and end length l_{end} is equal to 2.05 in.

From the results of (8.16) and (8.18), the time constant for each SB pole pair is:

$$\tau_{LR} = \frac{L_{SB_{pp}}}{R_{SB_{pp}}} = 30.5 \text{ ms} \quad (8.19)$$

8.4 Rotor Stability

The SB and spacer lengths, shown in Figure 8.8, were set to meet two overall design constraints:

1. The combined moments imposed on the rotor by the SLFBM and SB must be large enough to overcome a worst case rotor tilt. The moment contribution from the SB is largely determined by the spacer length, which sets the length of the lever arm for the moment imposed by the SB. In addition, the SB and SLFBM coil currents required to impose the restoring moment must be kept below the values given in Table 8.3 to prevent operating the iron near the nonlinear extremes of the B-H curve and remain in the vicinity of the linear approximations.
2. The rotor must not exhibit a I_z/I_x moment of inertia (MOI) ratio that is equal or close to one. As the rotor MOI ratio approaches one, the rotor becomes more sensitive to dynamic imbalances that will excite rotational resonance modes [1, 17]. To avoid the negative effects of resonant mode excitation, an MOI ratio between 0.90 and 1.10 is avoided in the UIFESS design.

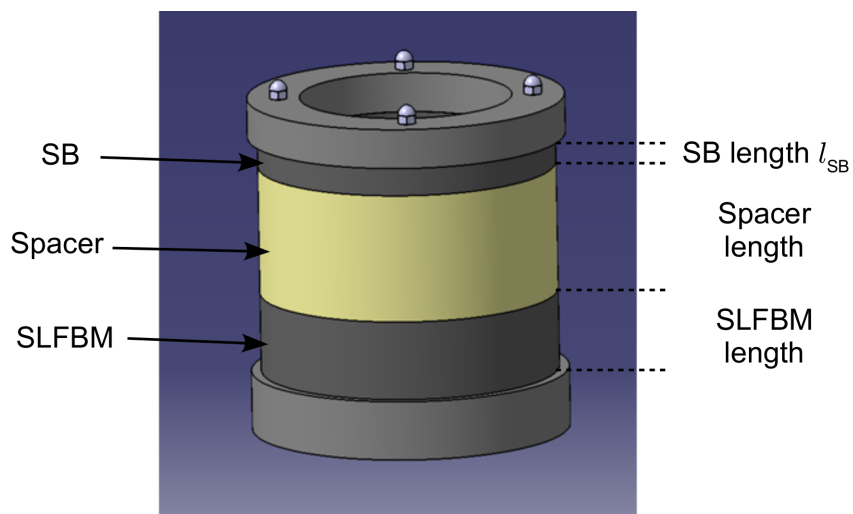


Figure 8.8: UIFESS rotor assembly

Due to time constraints, completing a dynamic rotor model to determine the precise force requirements of the SB was not feasible. Instead, a simpler, static force model was used. The static force model is included in [17]. The static force model investigates SB and SLFBM forces on the rotor during a worse case scenario for rotor tilt. In the worst case scenario, shown in Figure 8.9, the combined bearing forces of the SB and SLFBM must be capable of restoring the rotor back to a nominal air gap of 1.00 mm.

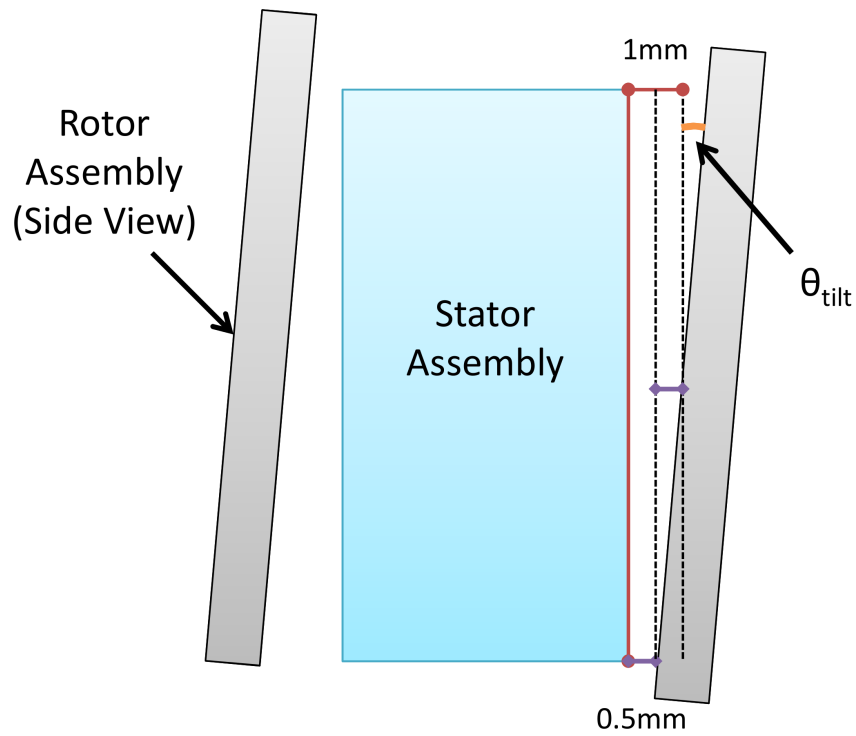


Figure 8.9: Worst case scenario for rotor tilt

Utilizing the static model to calculate the total moment imposed on the rotor by the SB and SLFBM, the SB length, spacer length, and spacer material were varied. Early in the design process, nylon was selected as the spacer material due to its ease of machining and low cost. With the spacer density set, an ad hoc approach ensued as combinations of SB and spacer lengths were varied against the amount of corrective current necessary to impose a restoring moment on the rotor. The possible combinations of SB and spacer lengths were limited by the physical design constraints in Table 8.3.

Combinations of SB and spacer lengths which resulted in a MOI ratio between 0.90 and 1.10 were automatically disregarded. Figure 8.10 describes the design process.

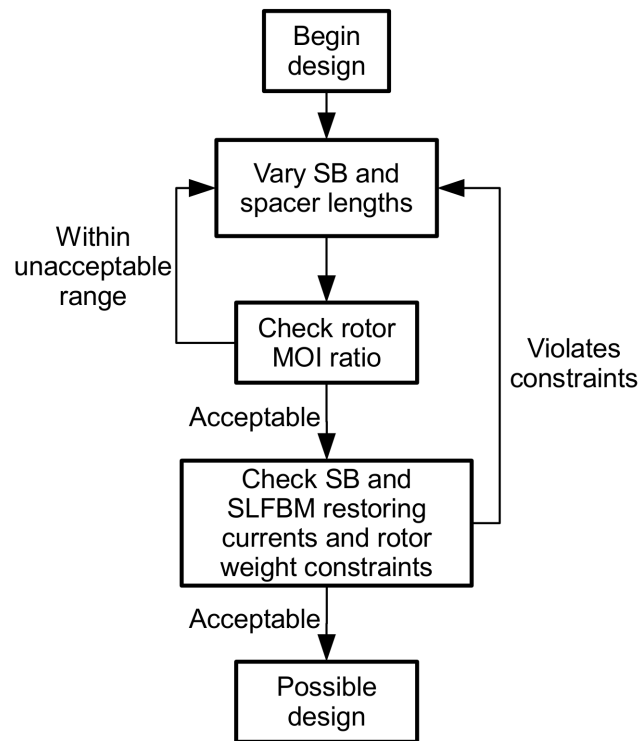


Figure 8.10: Design process for setting SB and spacer lengths

Table 8.3 displays the final results of the rotor stability design process along with the various design constraints. The design values in Table 8.3 provide a restoring moment to the rotor during a worst case rotor tilt scenario while providing negligible translational force. The ability to provide a restoring moment without translating the entire rotor is an important function, as the imposed translation would ultimately need to be prevented by the bearing. The final design parameters provide additional margin in Δi_{SB} in the event a larger SB moment is required.

A more detailed explanation of the development of the static model and rotor stability design process is available in [17].

Table 8.3: Rotor stability design parameters and constraints

Parameter	Design Value	Design Constraint
SB length (l_{SB})	0.75 in	Minimum length = 0.50 in
Spacer length	3.25 in	Minimum length = 2.80 in
MOI ratio	0.77	$1.10 < \text{MOI} < 0.90$
Required SB current change	1.35 A	Maximum $\Delta i_{SB} = 2.20$ A
Required SLFBM current change	0.65 A	Maximum $\Delta i_{SLFBM} = 0.80$ A
Rotor weight	36.1 lbs	Maximum weight = 40.0 lbs

8.5 Summary of SB Design Parameters

Table 8.4 summarizes all of the SB design parameters and expected capabilities calculated in Sections 8.3 and 8.4.

Table 8.4: SB parameters

Parameter	Value
Pole Face Cross Sectional Area ($A_{PoleFace}$)	0.306 in ²
Number of turns per pole (N)	183
Coil Gauge	18 AWG
Nominal Air Gap (g_0)	1.00 mm
Bias Flux Density (B_{bias})	0.60 T
Bias Current (i_{bias})	2.60 A
Bias Force	52.0 N
Saturation Flux Density (B_{sat})	1.2 T
Saturation Current	5.20 A
Maximum Force (at Saturation)	226.0 N
Nominal Inductance	16.6 mH
Coil Resistance	1.09 Ω
Force/displacement Factor (k_x)	207.53 N/mm
Force/current Factor (k_i)	79.82 N/A

8.6 FEA Verification

With the SB design completed, a Finite Element Analysis (FEA) was used to verify the expected bearing forces. The magnetomotive force (MMF) drop of the iron was neglected throughout the design process, therefore an FEA analysis will help investigate

the validity of this assumption and determine if premature saturation occurs. The FEA analysis was performed using the Finite Element Method Magnetics (FEMM) program by David Meeker, a freeware FEA program [42].

Figure 8.11 displays the SB flux density with all coils excited with the bias current of $i = 2.6$ A. The FEMM simulation calculates the force from each pole pair as 52.5 N,

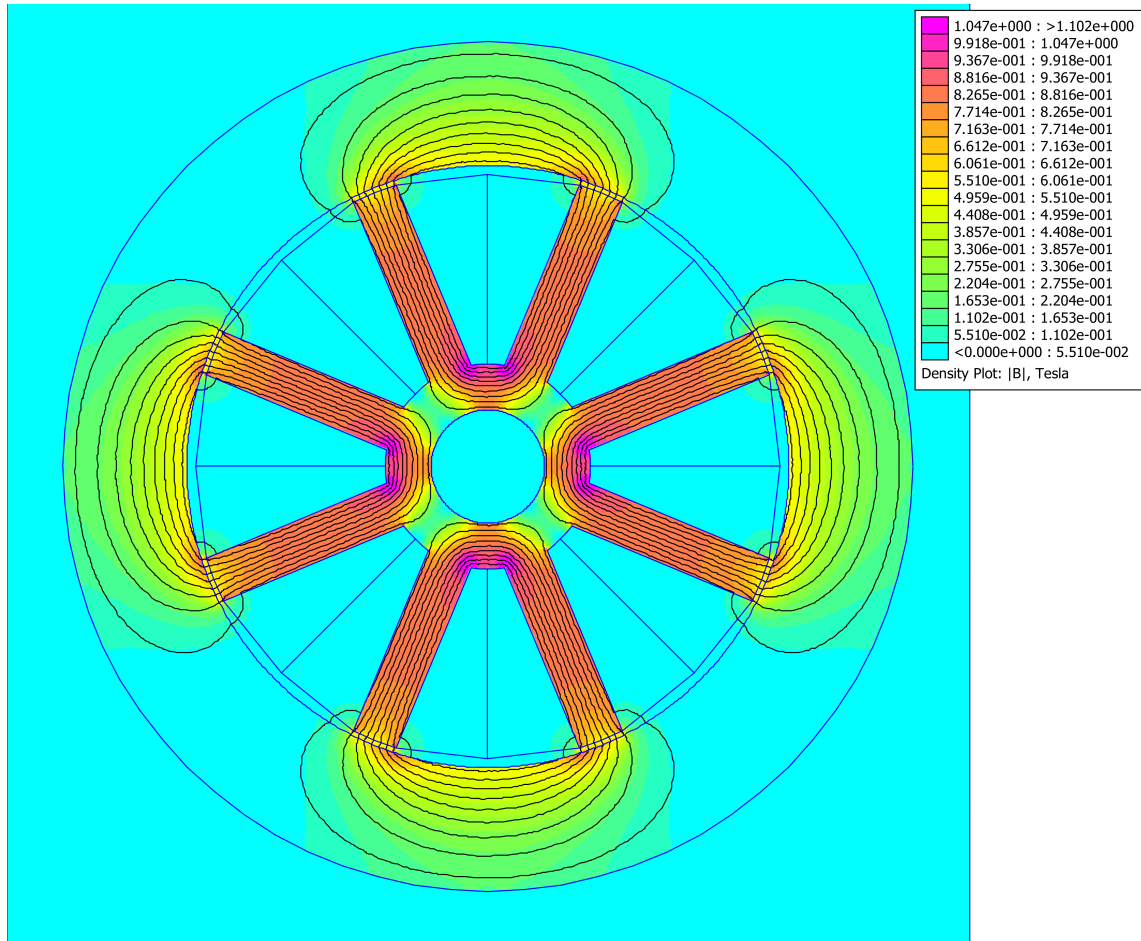


Figure 8.11: FEA results for SB with 2.6 A in all coils

showing close agreement with calculations. However, the flux density plot in Figure (8.11) shows slightly larger values for flux density in the stator teeth at approximately 0.7 T. As current in the coils is increased, saturation of the stator teeth may occur earlier than expected.

Figure 8.12 compares the calculated magnetic force/current relationship against FEMM simulation for a pole pair. The calculated and FEMM simulation force/current

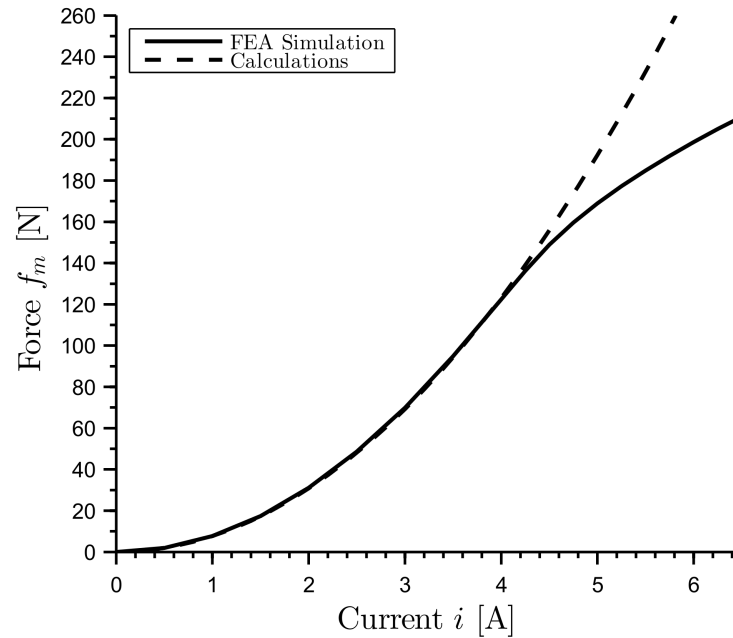


Figure 8.12: Calculated and FEA magnetic force vs. current for each SB pole pair

curves in Figure 8.12 show close agreement until roughly 4.5 A, when the magnetic force calculated by FEMM simulation begins to level off. This is due to magnetic saturation of the stator laminations, which limits the magnetic flux and decreases the available bearing force.

The relationship calculated by FEMM in Figure 8.12 is an important aspect to keep in mind as the SB control system is designed. Once tested experimentally, this phenomenon may call for an adjustment of the bias point. However, until experimentation is performed the discrepancy at larger currents is of no serious concern. The PID controllers have a degree of robustness which should account for the deviation.

8.7 Point Mass Simplification of Rotor

The SB and SLFBM work in tandem to control the rotor. Therefore, to utilize the SADB system plant, the equivalent mass of the rotor is determined at the location of each bearing. The equivalent mass at each bearing location represents the effective mass that must be controlled by each bearing. Simplifying the rotor to the point mass system in Figure 8.13 gives the equivalent masses m_{SB} and m_{SLFBM} at each bearing. The equivalent masses m_{SB} and m_{SLFBM} are calculated using (8.20) and (8.21), where the total rotor mass m_t is equal to 16.343 kg. The same point mass procedure is used in [24].

$$m_{SB} = m_t \frac{l_2}{l_t} = 5.31 \text{ kg} \quad (8.20)$$

$$m_{SLFBM} = m_t \frac{l_1}{l_t} = 11.04 \text{ kg} \quad (8.21)$$

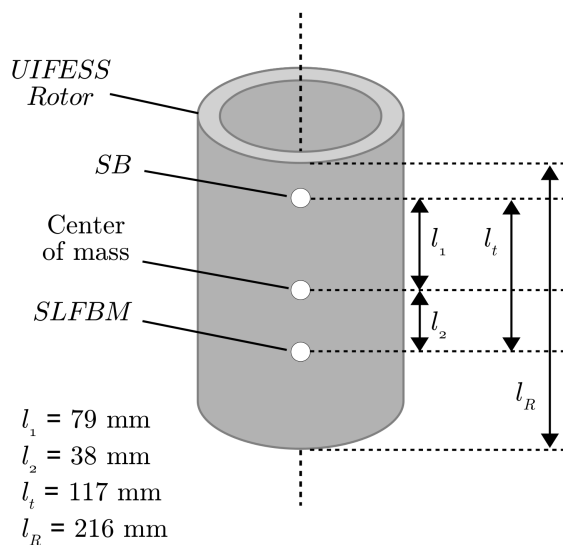


Figure 8.13: Point mass representation of the rotor

8.8 PID Controller Design for SB

As stated in Section 8.3, each axis of the SB is modeled as a separate SADB system. The SADB system plant is taken from (6.35) with the values for k_x and k_i taken from Table 8.2. The equivalent mass at the SB is taken from (8.20). With these parameters the SADB system plant is:

$$G_{z_{SB}}(z) = 7.5190 \cdot 10^{-8} \frac{z + 1.0000}{z^2 - 2.0004z + 1.0000} \quad (8.22)$$

Like the SASB plant in Section 7.3, the SADB plant in (8.22) is also unstable and exhibits a pole outside the unit circle at 1.02.

The PID controller design for the SB is very similar to SASB test set up described in Section 7.3. The PID controller was designed using the “PID Tuner” tool to the same conditions stated in Section 7.3. However, the design conditions in Section 7.3 are only utilized for testing purposes. As testing for both the UIFESS and SB progress, these design conditions may change to account for new performance requirements. In this event, the SB PID position controller will need to be redesigned to account for the new performance requirements.

The SB PID controller is taken from the expression developed in (6.21):

$$C_{d_{SB}}(z) = K_P + K_I \frac{T_s}{2} \frac{z + 1}{z - 1} + K_D \frac{1}{T_D + \frac{T_s}{2} \frac{z+1}{z-1}} \quad (8.23)$$

The PID controller parameters for (8.23) and the expected closed loop performance of the SADB system is given in Table 8.5.

To reduce the high frequency gain of the PID controller, the identical 2nd order Butterworth filter from Section 7.5 is utilized for the SADB system. The addition of the filter reduces the open loop phase margin from 60.0° to 50.2° , but is required to reduce the negative effect of high frequency noise. Placing the filter at the input of the PID

Table 8.5: SB PID position controller parameters and closed loop performance

PID Controller Parameters		Closed Loop Performance	
Parameter	Value	Metric	Value
K_P	$1.421 \cdot 10^4$	Settling Time	236 ms
K_I	$1.175 \cdot 10^5$	Rise Time	1.10 ms
K_D	65.16	Percent Overshoot	24.2%
T_D	$2.787 \cdot 10^{-4}$	Phase Margin	60.0°
f_D	571.0 Hz		
T_s	0.100 ms		

controller, the complete closed loop SADB system transfer function is:

$$H_{SBCL}(z) = \frac{F_{d_{filter}}(z)C_{d_{SB}}(z)G_{z_{SB}}(z)}{1 + F_{d_{filter}}(z)C_{d_{SB}}(z)G_{z_{SB}}(z)} \quad (8.24)$$

The poles and zeros of (8.24) are given in Table 8.6. Looking at poles listed in Table 8.6, stability is maintained with the addition of the filter since none of the closed loop poles exist outside of the unit circle.

Table 8.6: Poles and zeros of closed loop SB system

	Location
Pole 1	0.9989
Pole 2	0.9805
Poles 3,4	$0.8766 \pm 0.0977j$
Poles 5,6	$0.3546 \pm 0.3543j$
Zero 1	0.9991
Zero 2	0.9804
Zero 3	-1.0000
Zeros 4,5	$-1.0000 \pm 3.6919 \cdot 10^{-6}j$

8.9 SADB Simulink Model

The SADB model features an additional bearing over the SASB model which is capable of pulling an object in both directions. In essence, the SADB model is the combination of two opposing SASB models acting on the same object. Therefore, in order to test the SB system, the SASB Simulink model from Section 7.4 was adapted to feature

two opposing magnetic bearings operated in the “differential driving mode” strategy described in Section 5.7.

The SADB Simulink model serves the same purpose for the SB as the SASB Simulink model served for the SASB test setup. Like the SASB model, the SADB Simulink model emulates the digital sampling and ZOH hold behavior of the position and current controllers. The SADB Simulink model includes the magnetic force nonlinearities, bearing coil dynamics, and underlying current controllers in similar fashion to the SASB Simulink model.

Note that the SADB model simulates *one axis* of the SB. Simulation of the SADB model assumes all forces exist within a single axis. Although in practice each of the SB bearings will exhibit some force along the other axes, this behavior is neglected in simulation in order to isolate each PID controller and verify its functionality.

The SB Simulink model is depicted as four interconnected subsystems: the PID position control, the underlying bearing coil current control, bearing coil dynamics, and plant dynamics, shown in Figures 8.14, 8.15, 8.16, and 8.17, respectively.

Figures 8.18 and 8.19 show the x_1 and x_2 air gap responses, respectively, to a command change in x_1 from 1.00 mm to 1.10 mm. As expected, the air gaps are compliments of one another since x_1 and x_2 are the air gaps on each side of the rotor (from Figure 5.10). To compare the expected performance to the simulated performance, the settling time, rise time, and percent overshoot are measured for the response in Figure 8.18 and are given in Table 8.7. As in the SASB model, the air gap response of the SADB differs from the expected performance metrics. However, since the percent overshoot is still lower than the maximum design value and no oscillations are present in the response, the PID controller design was deemed satisfactory.

Figures 8.20 and 8.21 show the bearing coil current responses of i_1 and i_2 , respectively, for the 1.00 mm to 1.10 mm commanded step change in x_1 . Figures 8.20 and 8.21 show both the current commanded from the PID controller (blue) and the actual

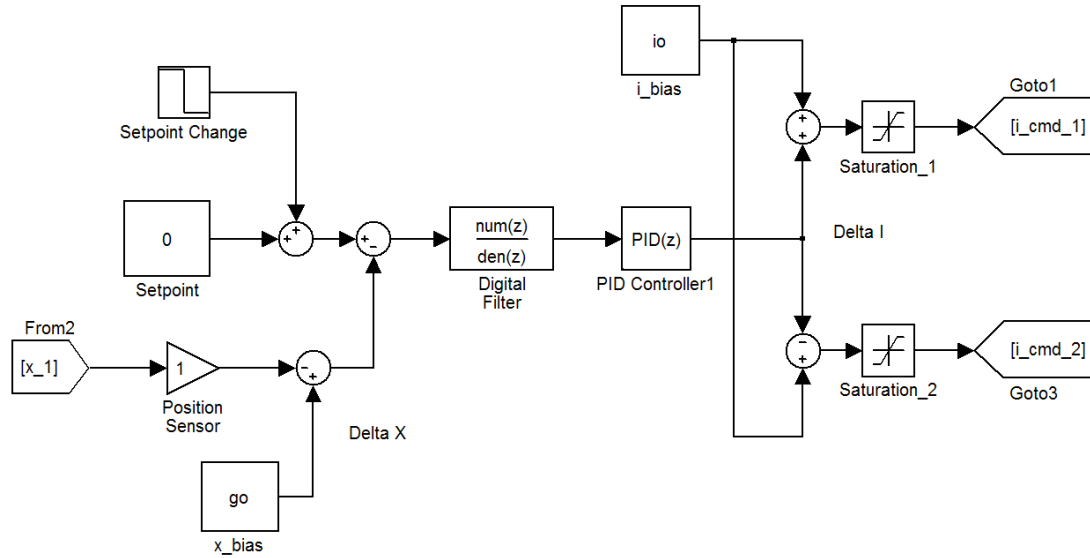


Figure 8.14: PID position control subsystem from SADB Simulink model

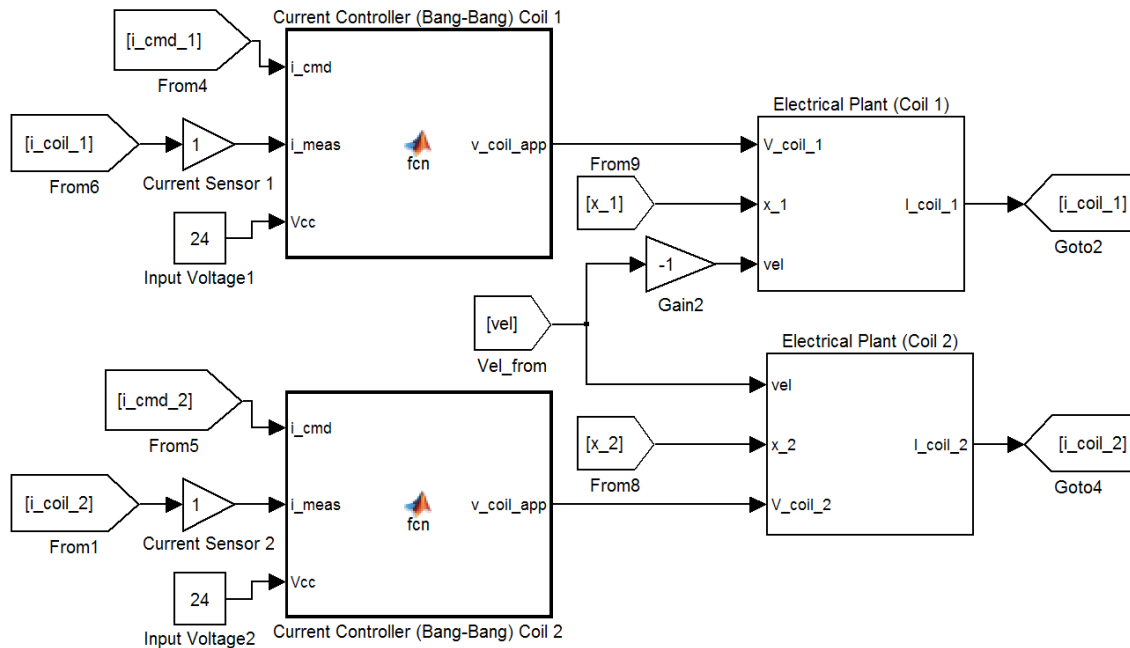


Figure 8.15: Underlying bearing coil current control subsystem from SADB Simulink model

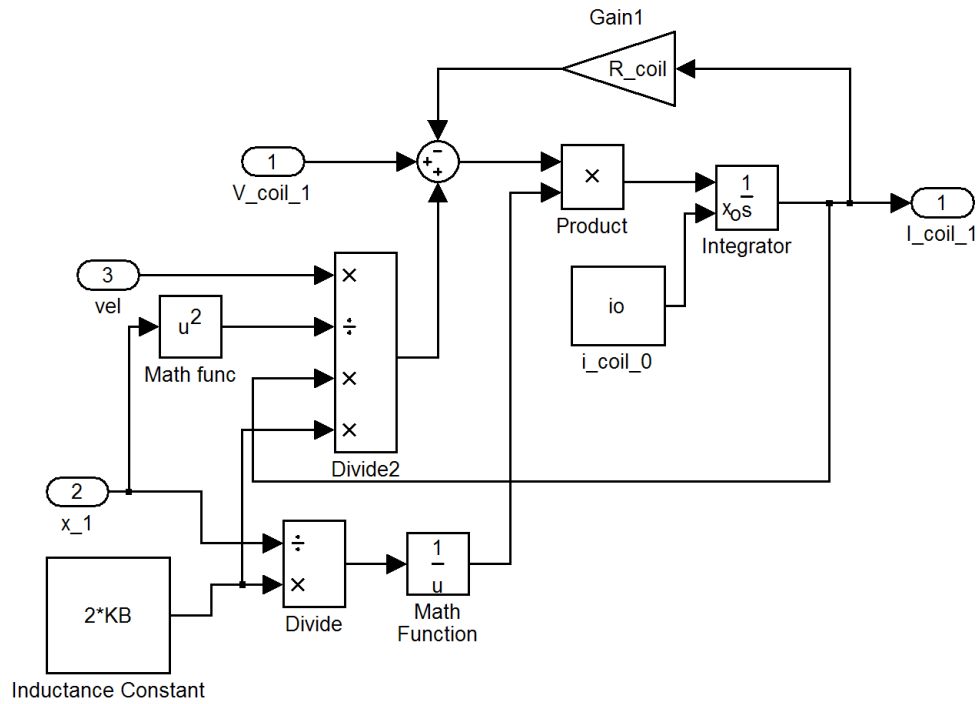


Figure 8.16: Bearing coil dynamics subsystem from SADB Simulink model

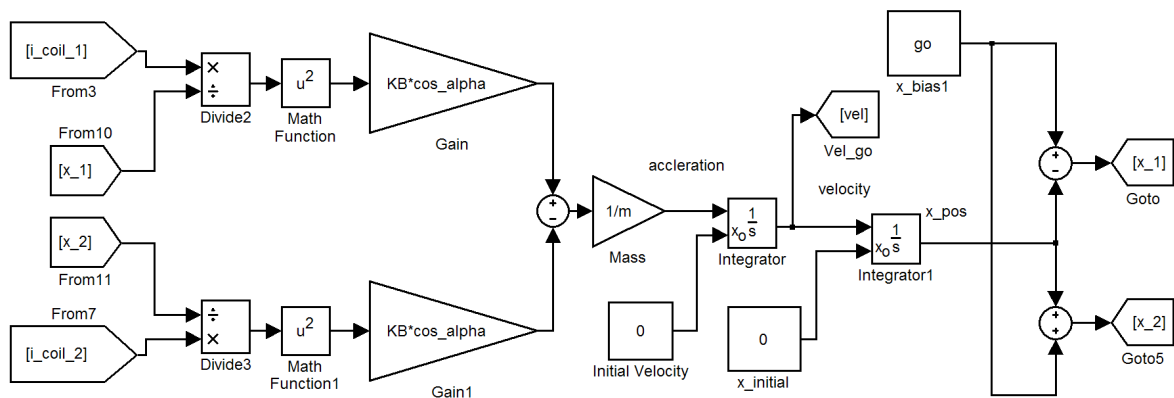


Figure 8.17: Plant dynamics subsystem from SADB Simulink model

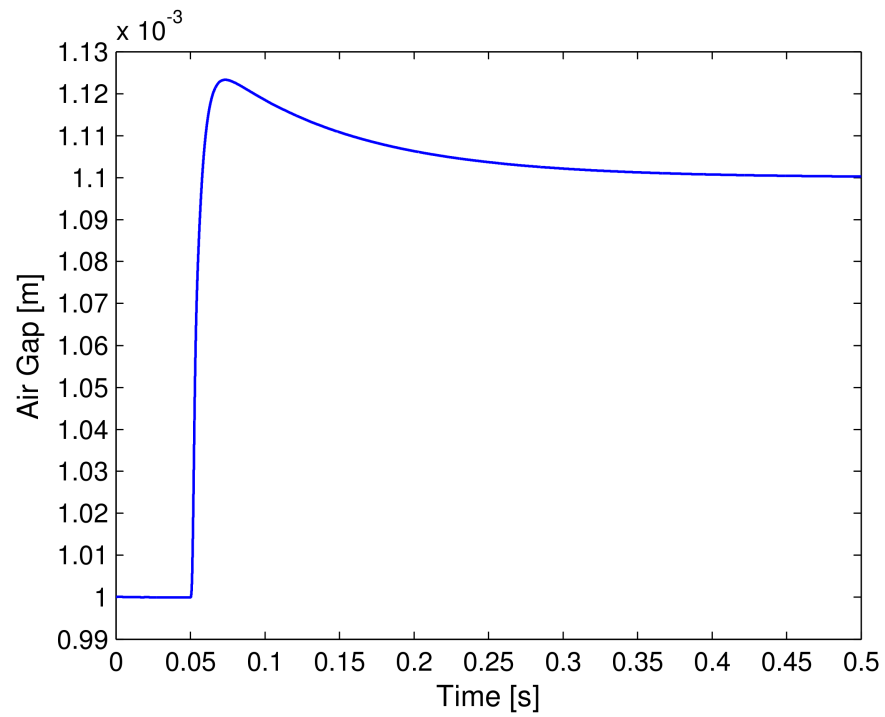
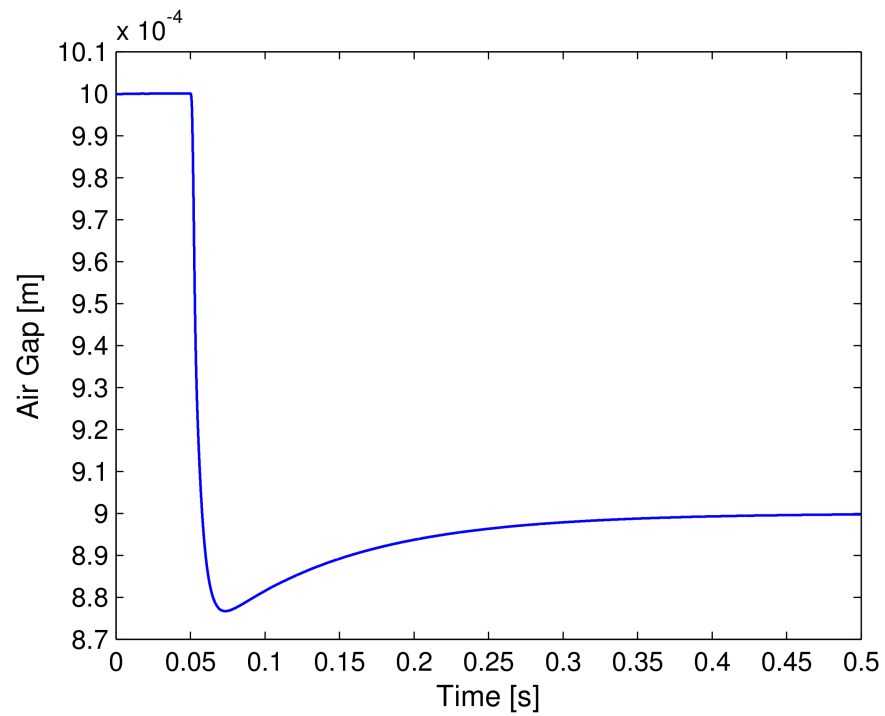
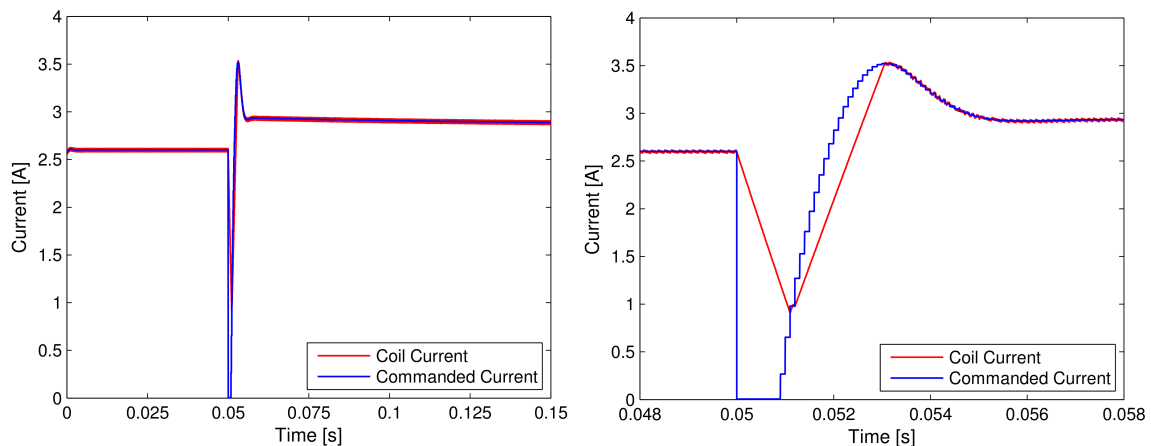
Figure 8.18: SADB air gap response x_1 to input step changeFigure 8.19: SADB air gap response x_2 to input step change

Table 8.7: Performance of SADB air gap response simulation

Metric	Value
Setting Time	236.0 ms
Rise Time	4.81 ms
Percent Overshoot	23.3%

current in the coil (red). As shown in the figures, to initially increase air gap x_1 , current i_2 increases while i_1 decreases. However, as x_1 approaches its commanded position (1.10 mm), currents i_1 and i_2 settle to new steady state values. With x_1 at 1.10 mm, the steady state value of i_1 is larger than its previous steady state value due to the increase in air gap x_1 . Conversely, the new steady state value of i_2 is smaller since air gap x_2 has decreased.

The current command signals from the PID controller are artificially limited to remain between 0 and 8 A. The limitations prevent potential high currents and negative currents in the bearing coils. The plots on the right hand side of Figures 8.20 and 8.21 show the current controller attempting to match the commanded current. Although the underlying current control struggles for current commands with large swings, the air gap response (for x_1 and x_2) is still satisfactory.

Figure 8.20: SADB coil current response i_1 to input step change

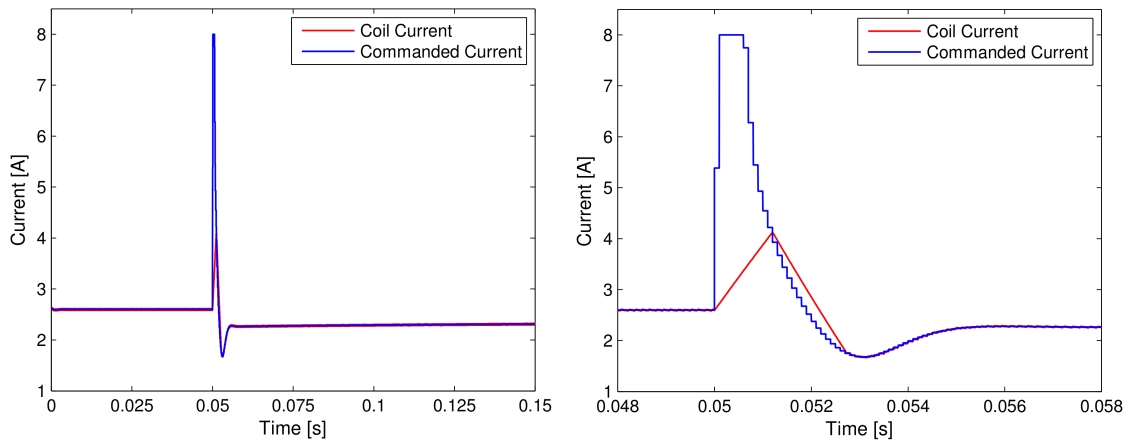


Figure 8.21: SADB coil current response i_2 to input step change

8.10 SB Wiring and Orientation

Figure 8.22 displays the wiring and position sensor orientation of the SB. As previously stated, the SB poles are utilized in pairs with their coils connected in series. In turn, each of the four pole pairs act as a separate bearing and impose a pulling force on the rotor in one of the four cardinal directions within the x-y plane of the SB.

From Figure 8.22, pole pairs (6,7), (2,3), (1,8), (4,5) make up the four separate bearings which impose pulling forces in the $+x$, $-x$, $+y$, and $-y$ directions, respectively. The separate bearings created by the pole pairs are labeled A through D as described in Table 8.8. Position sensor 1 reads the air gap in the x-axis g_x and position sensor 2 reads the air gap in y-axis g_y . The SB is composed of two decoupled SADB systems:

- **x-axis SADB:** Position sensor 1, bearings B and D
- **y-axis SADB:** Position sensor 2, bearings A and C

8.11 SB Hardware Implementation

The hardware required to implement the SB, shown in Figure 8.23, is an extension on the SASB test setup. The SB enacts control within two axes, with one position sensor

Table 8.8: SB pole pair bearing designations

Bearing	Pole Pair
A	(1,8)
B	(2,3)
C	(4,5)
D	(6,7)

8.12 SB Software Implementation

Much like the SB hardware implementation, the SB control software is an extension of the SASB test setup control software with additional capability to account for controlling two axes with four total bearings. The top level SB control software is identical to the SASB test setup and is described in Figure 7.12.

8.13 Control Performance

Within the time-line of completing this thesis, levitating the UIFESS rotor using the HTS bearing was still in an initial testing phase and had yet to be incorporated into the final UIFESS system. Therefore, the SB testing was performed with the rotor set on a platform supported by ball bearings. Although the platform inhibited motion along the z-axis, the rotor was free to “slide” in any direction within the x-y plane. Therefore, the SB could still be tested for 2 axis control.

For these tests, the SB was the only bearing system activated. The SLFBM was not energized. Therefore, for this phase in testing, the SB acted on the entire mass of the rotor, not just the equivalent mass developed in Section 8.7.

Another caveat for the SB testing concerns the position sensor mounting. The initial mechanical design for the SB position sensor mounts proved highly susceptible to vibration and were abandoned. A makeshift sensor mounting solution provided the capability to test the SB. However, the makeshift sensor mounting solution which is used to record the SB testing is still far from ideal. It is the author’s belief that a

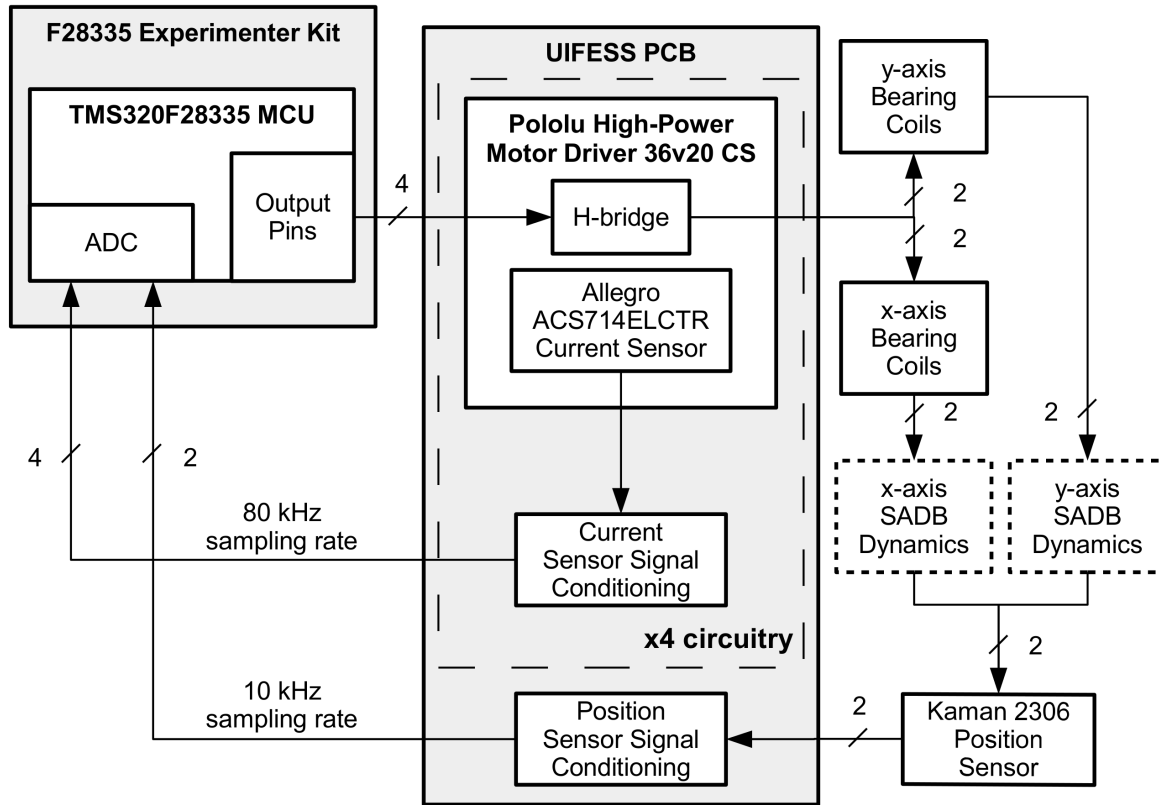


Figure 8.23: Functional block diagram of SB hardware

large portion of the oscillations present in the following results are due to sensor mount vibrations that can be mitigated by a sensor mount redesign.

Two SB test scenarios were investigated:

1. A commanded step change in g_x from 1.00 mm to 1.10 mm while holding g_y constant at 1.00 mm. This test mimicked the SADB Simulink simulation from Section 8.9 and isolated the controller performance along one axis.
2. A commanded step change in both g_x and g_y from 1.00 mm to 1.05 mm initiated simultaneously. This test investigates the cooperation of the two SADB systems. The same command step change is performed in simulation for a single axis for comparison.

The results from the two test scenarios are presented in the following sections.

8.13.1 Test Scenario One

Figure 8.24 compares the actual (blue) and simulated (red) air gap g_x response to a commanded step change from 1.00 mm to 1.10 mm. Figures 8.25 and 8.26 give the D and B bearing coil currents, respectively, and compares the result to the simulated response.

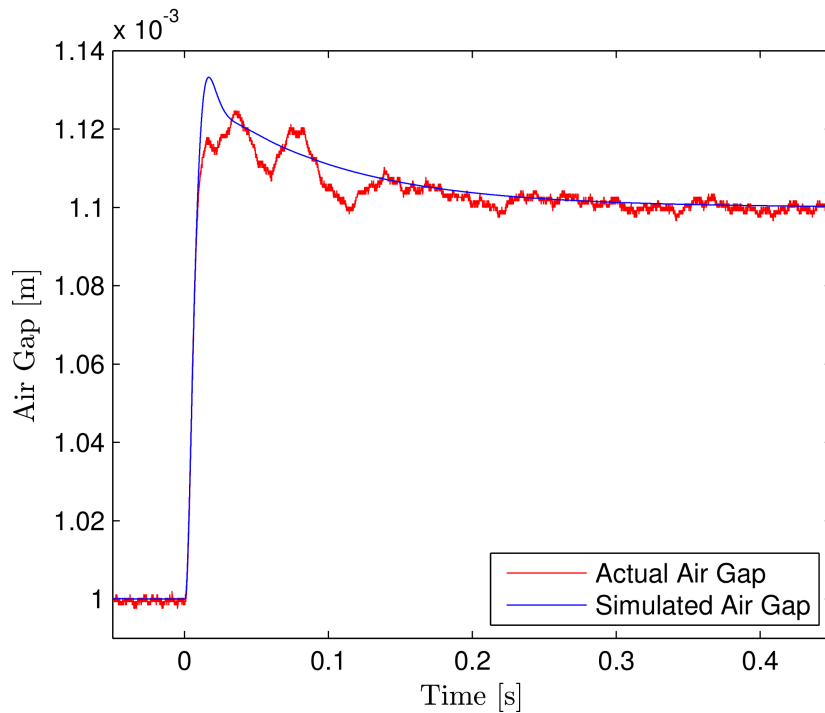


Figure 8.24: Air gap g_x for test scenario 1

8.13.2 Test Scenario Two

Figures 8.27 and 8.28 compare the actual (blue) and simulated (red) air gap responses for g_x and g_y , respectively. Both air gaps are commanded from 1.00 mm to 1.05 mm simultaneously.

The bearing coil responses for D, B, A, and C are given in Figures 8.29, 8.30, 8.31, and 8.32, respectively.

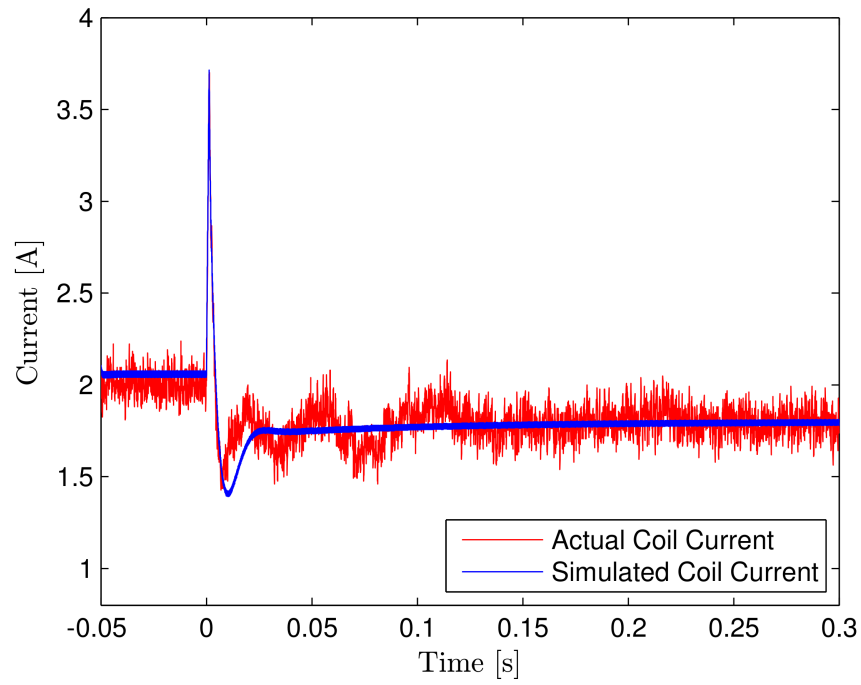


Figure 8.25: Bearing coil current D for test scenario 1

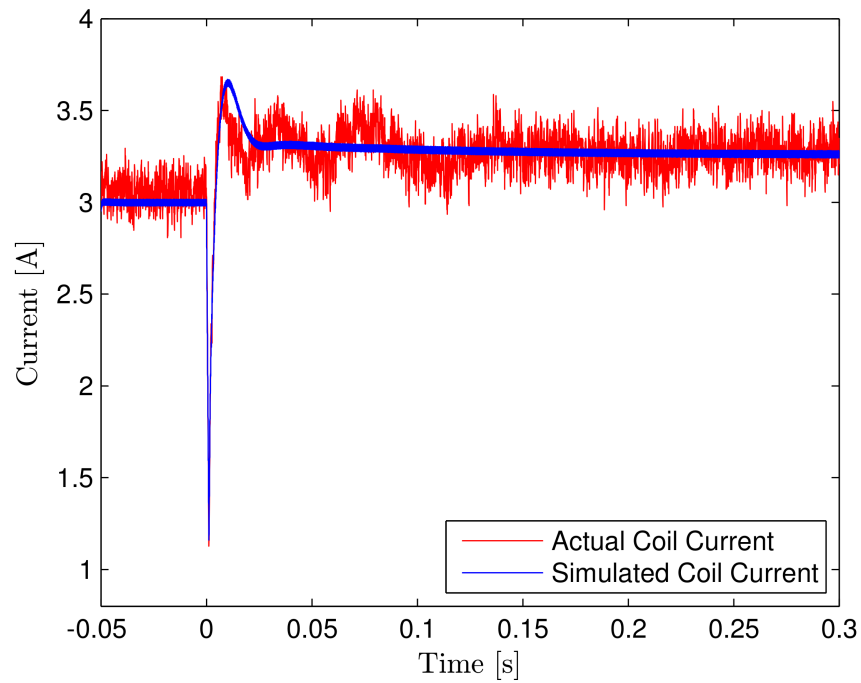
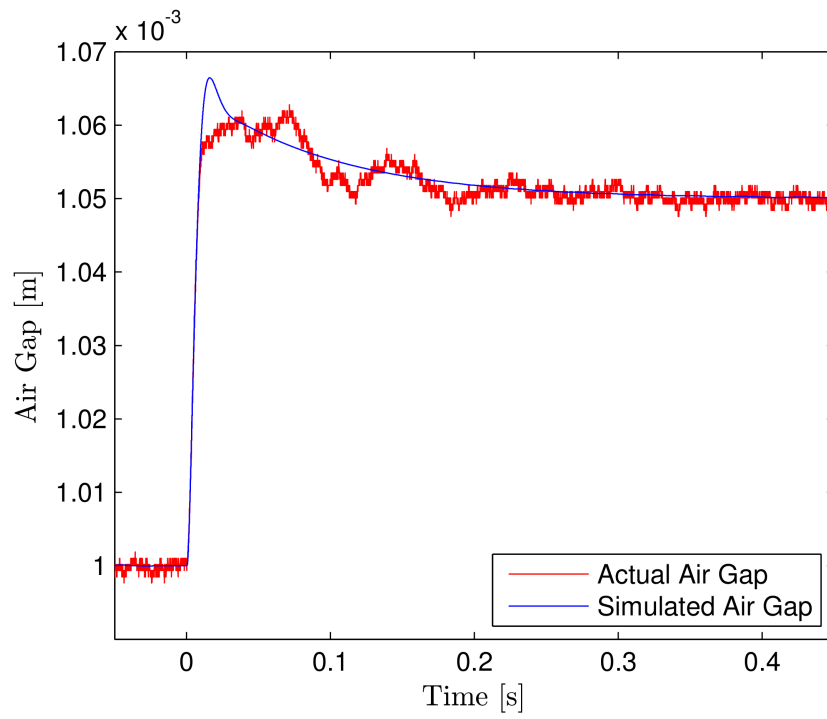
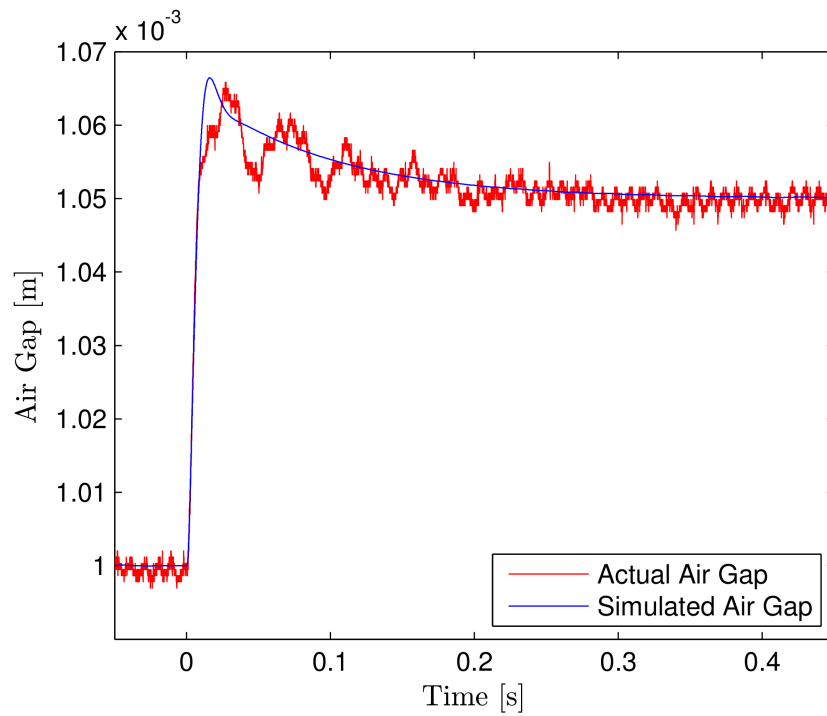


Figure 8.26: Bearing coil current B for test scenario 1

Figure 8.27: Air gap g_x for test scenario 2Figure 8.28: Air gap g_y for test scenario 2

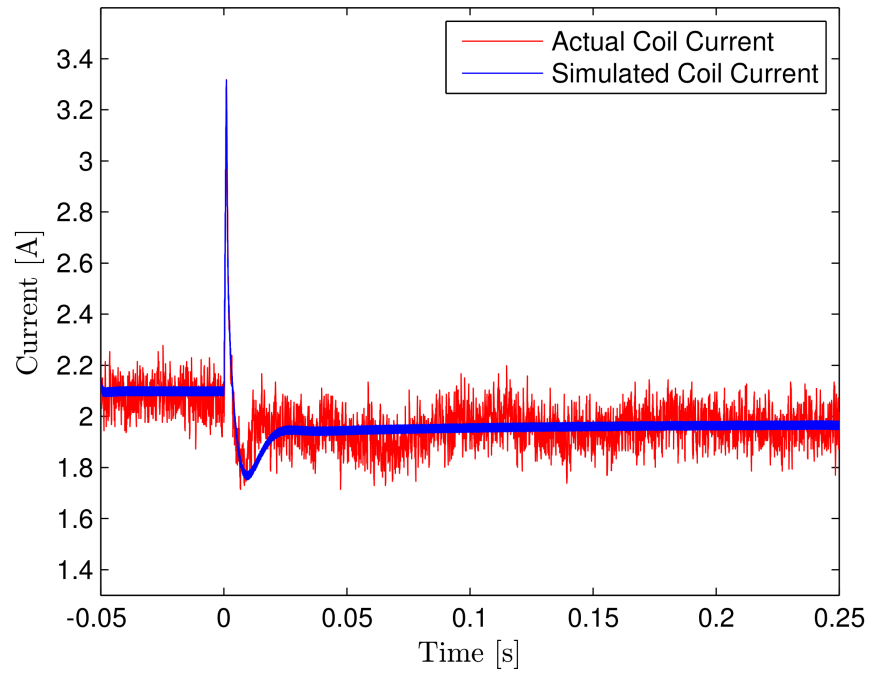


Figure 8.29: Bearing coil current D for test scenario 2

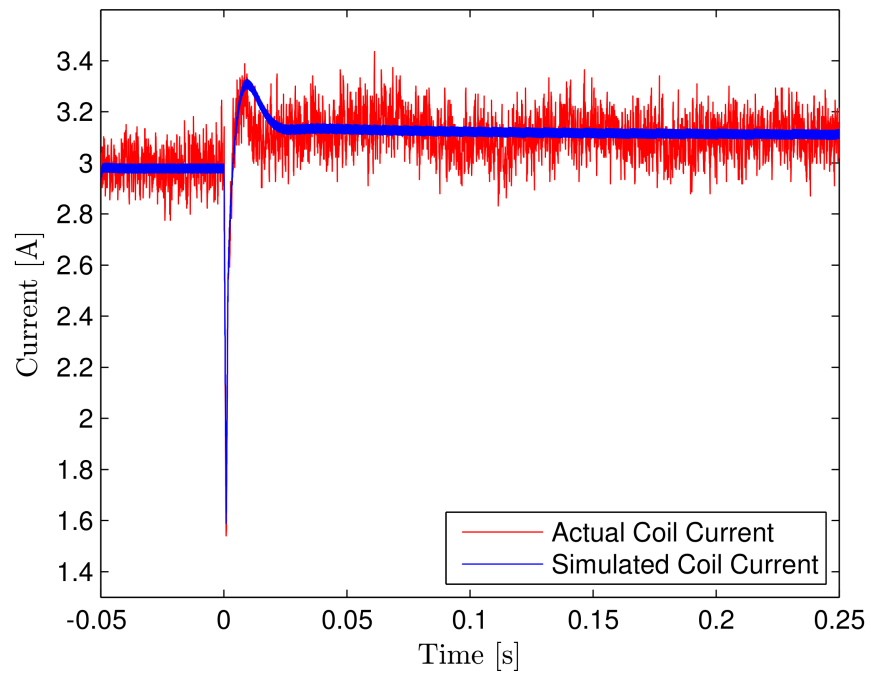


Figure 8.30: Bearing coil current B for test scenario 2

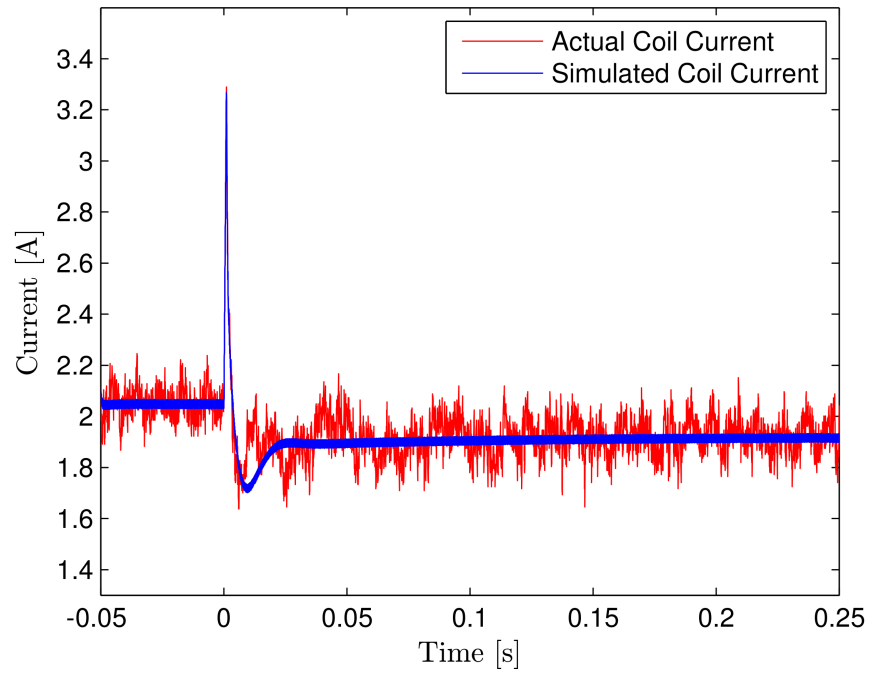


Figure 8.31: Bearing coil current A for test scenario 2

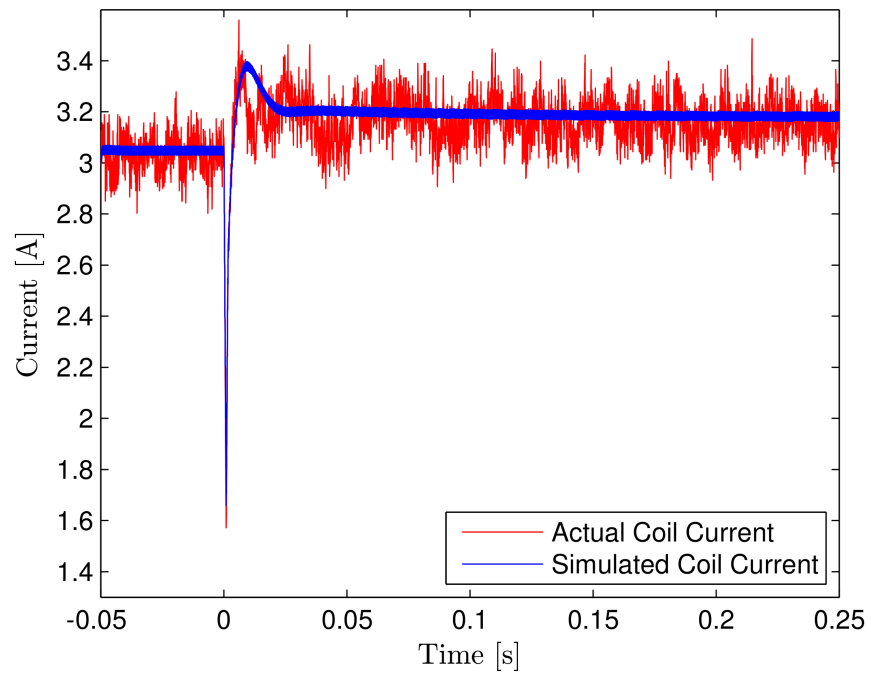


Figure 8.32: Bearing coil current C for test scenario 2

8.13.3 Test Scenario Results Summary

For both test scenarios, the actual and simulated results of the SB show less correlation than that of the SASB test setup. The lack of correlation is believed to be due to two limitations:

- The SB tests were performed with the rotor set upon a sliding support plate. Although the rotor was free to “slide” within the x-y plane, rotor movement was subject to friction. During the actual SB implementation, the rotor will experience zero friction. In addition, the SB was responsible for controlling the entire mass of the rotor and not the equivalent mass as it was designed to control.
- The SB sensor mounts used during testing were susceptible to vibration. The sensor vibrations are apparent from the large oscillations in the air gap response from Figures 8.28.

Both of the limitations listed above were due to time restrictions. It is the author’s opinion that with a fully levitated rotor and redesigned sensor mounts, the correlation between the actual and simulated data would improve. However, the results from these two test scenarios prove the SB is clearly capable of stabilizing the rotor.

Chapter 9

Self-bearing Machine Control

9.1 Introduction

This chapter describes the integration of the rotation and bearing control algorithms for the self-bearing machine (SLFBM). The SLFBM is a field regulated reluctance machine (FRRM) which has been adapted to additionally perform the functions of an AMB. The SLFBM rotation is described in Sections 9.2 and 9.3. The bearing control function and the integration of this function into of the SLFBM is described in Section 9.4.

The initial work in designing the PID position controller for the SLFBM is given in 9.5. The SLFBM PID position controllers were only designed for use in a simulation, and are given in analog form. The digital PID position controller design, implementation of the SLFBM rotation algorithm, and experimental testing of the SLFBM are items of future work.

9.2 Theory of Operation

A self-bearing machine (SLFBM) is a functional combination of a rotary machine and an active magnetic bearing [1]. In other words, a SLFBM provides both torque and corrective forces to the rotor. The advantages of a SLFBM is its compact design by removing the need for a dedicated AMB system. In turn, the removal of a dedicated AMB system reduces the size, mass, and hardware complexity of the overall system. However, the combination of rotary and bearing functions in a SLFBM requires a more complex control system to perform both functions simultaneously.

The UIFESS adapts the functionality of the Field Regulated Reluctance Machine (FRRM) to provide corrective forces and serve as a SLFBM. The FRRM is the mechanism through which energy is stored and extracted from the flywheel. To store energy,

the FRRM is operated as a motor and spins up the flywheel to high speeds. To extract the stored energy, the FRRM is operated as a generator and relies upon the inertia of the flywheel to generate electrical energy. Although the behavior of the FRRM changes during periods of motoring, idling, and generation, the bearing action of the SLFBM must continue to operate to stabilize the rotor.

Previous work in [43] investigated various machine types for use in a flywheel energy storage application. The analysis in [43] showed the FRRM to possess the the highest force density among the machines considered. Although a more in depth description of why the FRRM was selected for the UIFESS design is available in [17], the advantages of the FRRM which led to its selection are summarized below:

- The FRRM rotor can be degaussed, reducing the magnetic losses during idling. Ultimately, this leads to a more efficient FES system.
- The FRRM design does not require slip rings or brushes, resulting in zero physical contact with the rotor.
- The FRRM design allows for independent control of excitation and armature windings to provide independent control of torque and regulation of the field flux. In turn, this ability allows the FRRM to operate along different torque-speed curves much like a separately excited DC machine.
- The FRRM is a high force density machine.

Due to the highly specific requirements of the UIFESS and the limited availability of FRRMs, the UIFESS FRRM was designed and fabricated in-house at the University of Idaho. A detailed description of the FRRM design is available in [17]. Figure 9.1 depicts the final design of the FRRM machine laminations. The UIFESS FRRM is a 4 pole machine with 6 coils per pole. In Figure 9.1, the \otimes symbol represents current traveling into the page and the \odot symbol represents current traveling out of the page.

Each coil in Figure 9.1 is represented by a number. The “a” modifier indicates the return winding of the coil.

To achieve rotation, the FRRM coils are operated in a time share mode. For a portion of time each coil is operated as the excitation (field) winding and for a portion of time as the armature winding. The operation mode for a particular winding is dependent on rotor position. The winding operation modes of the FRRM perform the corresponding function as the excitation and armature windings of a conventional DC machine. During the time when the winding is located under the pole face, the winding is operated and controlled as an armature winding. During the time when the winding is located in the interpole region, the winding is operated and controlled as an excitation winding.

The excitation windings induce magnetic flux within the rotor. The excitation windings for each pole are composed of four coils, and will be collectively referred to as the d-axis coils. The armature windings are responsible for torque production. The armature windings for each pole are composed of two coils, and will be collectively referred to as the q-axis coils. The d-axis current i_d and the q-axis current i_q are the currents within each d-axis and q-axis coil, respectively. Figure 9.1 displays the location of flux and torque producing (d and q-axis) coils relative to the location of the rotor poles.

9.3 SLFBM Rotation Control

Torque is applied to the rotor at the face of each rotor pole by the Lorentz force principle. The rotor flux (which is provided by the d-axis coils) linked across the air gap interacts with the current in the q-axis coils to produce a tangential force at the face of each rotor pole; in turn, creating a torque on the rotor. As the rotor moves in response to the applied torque, the operation mode of the FRRM is adjusted accordingly to continuously apply torque to the rotor as it rotates.

In other words, the operation mode of each coil is dependent on the rotor position as it rotates around the stator. Table 9.1 shows the coil operation mode or “state” for each rotor position, and gives the value of current within the coil. The negative signs in Table 9.1 indicate the coil current is flowing in the opposite direction to the polarity given in Figure 9.1.

Figure 9.2 displays the drive control for the FRRM. Control is accomplished through measurement feedback of rotor position and coil currents. The FRRM torque is proportional to both i_d and i_q . The d-axis current i_d is set to achieve a particular torque-speed curve while the q-axis is manipulated in real time to achieve the desired operating point within the curve. The d-axis current adjustment Δi_d is the result of the self-bearing action and is described in Section 9.4.

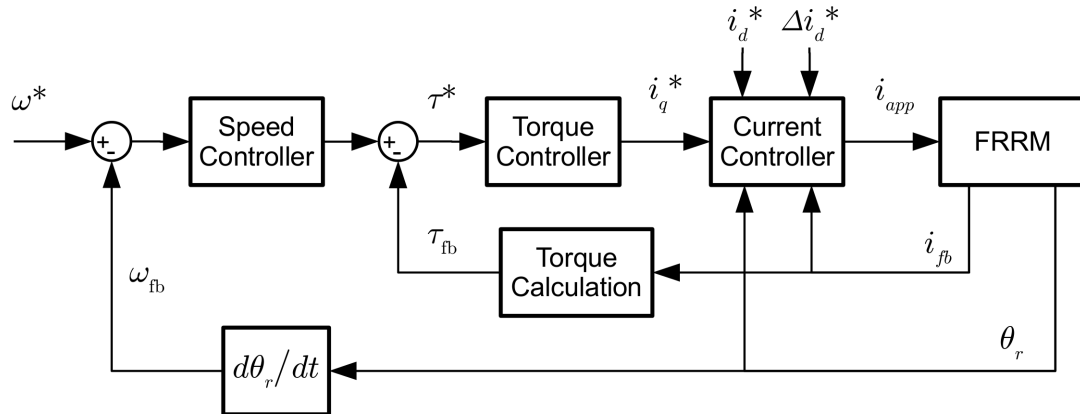


Figure 9.2: SLFBM drive control system

Figure 9.2 is a high level description and is only meant to provide a functional understanding of the FRRM drive. The details and design behind the speed and torque controllers are beyond the scope of this thesis. The current control block in Figure 9.2 is expanded in Figure 9.3. The multiplexer (MUX) in Figure 9.3 is controlled by θ_1 and is responsible for dictating the operating mode of each coil depending on the rotor position θ_1 as described in Table 9.1.

Table 9.1: Coil states during operation

Phase #	θr (degrees)																							
	0	15	30	45	60	75	90	105	120	135	150	165	180	195	210	225	240	255	270	285	300	315	330	345
1	I_q		I_d				$-I_q$		$-I_d$				I_q		I_d				$-I_q$		$-I_d$			
2		I_d				$-I_q$		$-I_d$				I_q		I_d				$-I_q$		$-I_d$				I_q
3	I_d				$-I_q$		$-I_d$				I_q		I_d				$-I_q$		$-I_d$				I_q	
4				$-I_q$		$-I_d$				I_q		I_d				$-I_q$		$-I_d$				I_q		I_d
5			$-I_q$		$-I_d$					I_q		I_d				$-I_q$		$-I_d$				I_q		I_d
6		$-I_q$		$-I_d$						I_q		I_d				$-I_q$		$-I_d$				I_q		I_d
7	$-I_q$		$-I_d$				I_q		I_d					$-I_q$		$-I_d$				I_q		I_d		
8		$-I_d$				I_q		I_d					$-I_q$		$-I_d$				I_q		I_d			$-I_q$
9	$-I_d$				I_q		I_d					$-I_q$		$-I_d$				I_q		I_d				$-I_q$
10				I_q		I_d					$-I_q$		$-I_d$				I_q		I_d				$-I_q$	$-I_d$
11			I_q		I_d					$-I_q$		$-I_d$				I_q		I_d				$-I_q$		$-I_d$
12		I_q		I_d					$-I_q$		$-I_d$				I_q		I_d				$-I_q$		$-I_d$	
13	I_q		I_d				$-I_q$		$-I_d$				I_q		I_d				$-I_q$		$-I_d$			
14		I_d				$-I_q$		$-I_d$				I_q		I_d				$-I_q$		$-I_d$				I_q
15	I_d				$-I_q$		$-I_d$				I_q		I_d				$-I_q$		$-I_d$				I_q	
16				$-I_q$		$-I_d$				I_q		I_d					$-I_q$		$-I_d$				I_q	I_d
17			$-I_q$		$-I_d$					I_q		I_d				$-I_q$		$-I_d$				I_q		I_d
18		$-I_q$		$-I_d$				I_q		I_d					$-I_q$		$-I_d$				I_q		I_d	
19	$-I_q$		$-I_d$				I_q		I_d					$-I_q$		$-I_d$				I_q		I_d		
20		$-I_d$				I_q		I_d					$-I_q$		$-I_d$				I_q		I_d			$-I_q$
21	$-I_d$				I_q		I_d					$-I_q$		$-I_d$				I_q		I_d				$-I_q$
22				I_q		I_d					$-I_q$		$-I_d$				I_q		I_d				$-I_q$	$-I_d$
23			I_q		I_d					$-I_q$		$-I_d$				I_q		I_d				$-I_q$		$-I_d$
24		I_q		I_d					$-I_q$		$-I_d$				I_q		I_d				$-I_q$		$-I_d$	

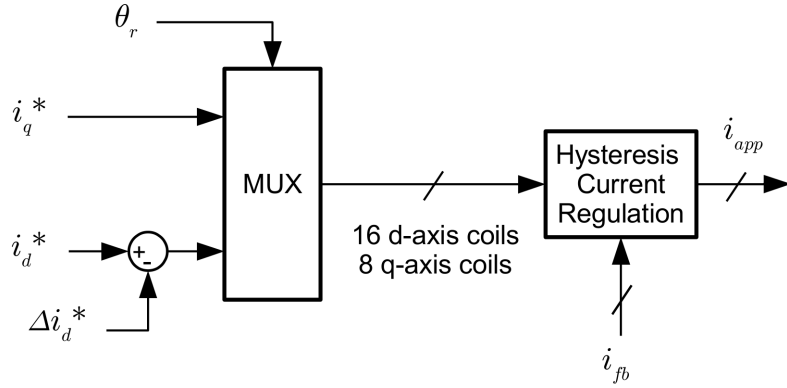


Figure 9.3: SLFBM current control, expanded from Figure 9.2

9.4 SLFBM Bearing Control

The self-bearing behavior of the FRRM is achieved by varying the d-axis coil currents with respect to radial disturbances. Changing the d-axis currents changes the magnetic flux within the rotor. In turn, the rotor magnetic flux B_{rotor} creates a magnetic force which acts across the air gap underneath each pole, attempting to pull the rotor pole toward the stator. As the rotor spins, the d-axis coils are constantly adjusted to maintain a constant air gap. The magnetic force across the air gap due to the d-axis coils is:

$$f_{m_d} = 8\mu_0 N^2 A_{CS} \left(\frac{i_d}{g} \right)^2 \quad (9.1)$$

where N is the number of turns of each coil, A_{CS} is the cross sectional area of the pole face, and g is the air gap underneath the pole face. The expression in (9.1) is taken from [17].

The four pole structure of the UIFESS FRRM provides a natural division of forces into two orthogonal axes. In turn, the SADB model can be applied to each of the orthogonal axes. However, unlike the SB, the orthogonal axes rotate along with the rotor poles. This poses a problem since the position sensors are stationary and the d-axis air gap (i.e. the air gap underneath each rotor pole) rotates. Therefore, position

sensor readings must be transformed to a rotating frame that moves along with the rotor poles.

To calculate air gaps underneath the rotating rotor poles, the stationary measurements must be transformed to rotating coordinates. Equation (9.2) gives the stationary to rotational coordinate transformation:

$$\begin{bmatrix} X_R \\ Y_R \end{bmatrix} = \begin{bmatrix} \cos \theta_r & -\sin \theta_r \\ \sin \theta_r & \cos \theta_r \end{bmatrix} \begin{bmatrix} X_S \\ Y_S \end{bmatrix} \quad (9.2)$$

where θ_r gives angular rotor position. The coordinates in (9.2) are shown relative to the SLFBM in Figure 9.4.

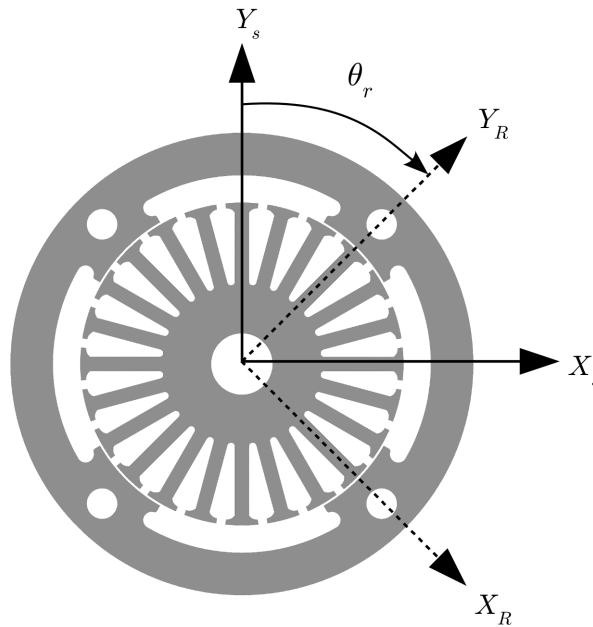


Figure 9.4: Depiction of stationary to rotational reference frame for the SLFBM

Utilizing the stationary-to-rotational reference frame transformation, the air gaps are modeled as two decoupled SADB systems, each controlled with a separate PID controller to control the radial air gap. The PID controllers output a small signal Δi_d^* for each axis that is used to adjust the nominal value of i_d^* during current control. Figure 9.5 describes the AMB algorithm for the SLFBM. For the sake of brevity, the

small signal adjustments in each axes (Δi_{dx}^* and Δi_{dy}^*) are collectively represented as Δi_d^* , which is featured in Figures 9.2 and 9.3.

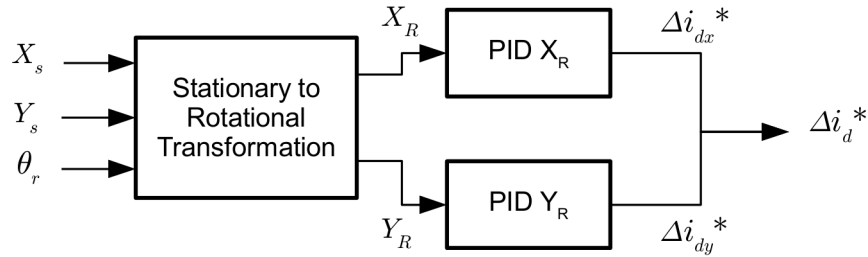


Figure 9.5: SLFBM bearing function control algorithm

9.5 PID Controller Design for SLFBM

For the timeline of this thesis, testing of the radial bearing function of the SLFBM has only been performed in simulation in [17]. The simulation of the UIFESS rotor dynamics has yet to incorporate modeling of the discrete controller and bearing coil dynamics. Currently, the simulation assumes analog PID controllers. Therefore, the PID controllers for the UIFESS rotor dynamics simulation in [17] were designed using the analog plant from (6.14):

$$G_{cSLFBM}(s) = \frac{k_i/m_{SLFBM}}{s^2 - k_x/m_{SLFBM}} \quad (9.3)$$

where k_x , k_i , and m_{SLFBM} are given in Table 9.2.

Calculating the equivalent position stiffness k_x and current stiffness k_i is more difficult for the FRRM than for the SB and SASB test setup. Due to the complex geometry and resulting flux paths within the FRRM, a “modified winding” approach was used to find k_x and k_i . The “modified winding” approach is described in [17]. The equivalent mass “seen” by the SLFBM is taken from (8.21).

Table 9.2: SLFBM bearing control parameters

Parameter	Value
Force/displacement Factor (k_x)	665.14 N/mm
Force/current Factor (k_i)	366.84 N/A
Equivalent Mass (m_{SLFBM})	11.04 kg

Both of the X_r and Y_r PID controllers have identical form. Utilizing the “PID Tuner” tool, the analog PID controller is given in (9.4). Similar to the SB PID controller design, the controller in (9.4) is designed to achieve a 60° open loop phase margin.

$$C_{SLFBM}(s) = 41929 + 1174808 \frac{1}{s} + 44.4 s \quad (9.4)$$

Simulation results implementing the SLFBM PID controllers are given in [17]. As the UIFESS rotor dynamics model is adapted to model the discrete PID controllers, the PID controller design process presented here must also be adapted to the method presented Section 8.8 for the SB.

Chapter 10

Summary and Conclusions

10.1 Summary

Active magnetic bearings (AMB) provide frictionless support to rotating machinery. The absence of friction in an AMB allows for very high rotational speeds and low energy loss, characteristics which are especially advantageous for FES systems. This thesis described the initial work in implementing AMBs for the UIFESS, an experimental FES storage system which was designed at the University of Idaho and is currently undergoing the initial phases of testing at the same facility.

In order to properly characterize and design the UIFESS AMB systems, individually referred to as the SB and SLFBM systems, the mathematical model of an AMB was developed and described. Separate AMB models were developed for both single bearing and dual bearing cases, referred to as the SASB and SADB models, respectively. The SADB model was used to model the SB and SLFBM systems. Before delving into the design of these systems, however, the SASB test setup was used to verify the modeling, simulation, and implementation of the SASB model. The process of proving the SASB model on the SASB test setup provided essential experience before tackling the design of the SB and SLFBM systems.

Both AMB models are inherently nonlinear and were linearized in order to represent the models as LTI systems. Although the linearization is only an approximation of the truly nonlinear AMB system behavior, LTI systems can be analyzed using well established techniques from classical control theory. In turn, a linearized AMB model is required to properly design a linear control law.

To achieve an accurate linear approximation, the linearization was performed around an advantageous operating point along the iron B-H curve. The midpoint of quasi linear behavior of the iron is 0.6 T, and was chosen as the operating (bias) point

for the linearization of the AMB model. During operation, small signal control adjustments around the 0.6 T bias point will exhibit a relatively linear behavior from the iron.

The SB and SLFBM systems were designed to implement a decentralized PID control scheme. Decentralized PID control is a common control scheme for AMB applications, especially in industry. A decentralized PID control scheme decouples each control axis into a separate low order plant. A local PID controller is designed to control each decoupled plant, and is responsible for maintaining the air gap within a single axis. The decentralized PID control offers simplicity in controller design and implementation, as each local PID controller can exist within a separate MCU.

The UIFESS control system is implemented digitally to offer greater flexibility. The digital PID controller is an outer control loop which maintains the air gap. An inner “underlying” hysteresis current control loop regulates the bearing coil current and is also implemented digitally.

Once represented as LTI systems, the SASB and SADB models were transformed into the complex frequency domain to obtain a small signal transfer function for each AMB model. The SASB and SADB small signal transfer functions have identical structure and only differ in the values of their coefficients. Since the UIFESS AMB control is implemented in a digital microcontroller, the AMB transfer functions were converted from the continuous time complex frequency domain (s -domain) to the discrete time complex frequency domain (z -domain) to account for the effects of the digital sampling delay and ZOH element. The relative stability of each decoupled AMB system plant and PID position controller was evaluated to make sure the design exhibited a certain degree of robustness.

With the SASB and SADB system plants modeled in the z -domain, the digital PID controllers are designed using MATLAB. The digital PID design assumed a linear magnetic bearing model and instantaneous bearing coil dynamics. In practice, neither

of these assumptions hold. The nonlinear magnetic bearing behavior and the bearing coil dynamics will effect bearing performance. To evaluate the PID design in the face of these additional effects, Simulink models were created. The Simulink models reflect the interaction between discrete and continuous time domains using discrete blocks for the digital control system and continuous blocks for the analog system plant.

As previously mentioned, hardware and software testing began with the SASB test setup. Results from the SASB were promising, and good agreement was achieved between simulated and test data. The similarities between the SASB and SADB models allowed the SASB test setup to function as a test bed for debugging the hardware and software that was utilized for SB and will eventually control the SLFBM.

The SB was tested and two axis control was demonstrated. The decoupled PID controllers in each of the SB axes worked together to maintain the radial air gap. Simulation and test data were compared, the test data features slight oscillations due to the position sensor mount susceptibility to vibration. Redesigned sensor mounts should mitigate the issue.

In addition to the control of the UIFESS AMB systems, this thesis described the geometric design of the SB. The SB is an 8 pole outer-rotor type dedicated AMB and was an addition to the original UIFESS design to enable restoring moments on the rotor. The SB lamination geometry was optimized to produce the largest amount of magnetic force possible. The lengths of the SB and spacer were then set to achieve a stable moment of inertia ratio and impose a restoring moment during a worst case rotor tilt scenario. The SB and spacer lengths were also constrained by other parameters and were selected using an iterative approach. FEA software was used to verify the calculated force output of the SB. Calculations closely matched FEA results for bearing coil currents less than 4.5 A. Currents larger than 4.5 A begin to saturate the SB stator poles.

This thesis also described the integration of rotation and bearing control algorithms for the SLFBM. The UIFESS adapts the FRRM design to also perform the AMB func-

tions. The integration between the rotation and bearing control is accomplished by adjusting the d-axis currents to impose corrective radial forces on the rotor. The bearing control system for the SLFBM was designed in this thesis and tested in a simulation from [17].

10.2 Conclusions

The following list describes the main conclusions from this work:

- The modeling and simulation of the SASB and SADB were effective in predicting the behavior of the SASB test setup and the SB. Although the bearing coil dynamics were ignored during the PID position controller design, the SASB and SADB Simulink models provided a testbed for evaluating the system behavior when the bearing coil dynamics are included.
- The SASB test setup provided a useful testbed for designing the software and hardware for the SB and SLFBM. The SASB test setup allowed for rapid debugging since the SASB isolated a single axis. Achieving AMB control in a single axis was important from both a conceptual and practical standpoint, since the decentralized control scheme decouples control into a number of different axes. Future researchers on the UIFESS project can also utilize the SASB test setup to experiment with new control algorithms before moving to the actual UIFESS.
- The decentralized PID approach was effective in providing 2 axis air gap control to the SB. The results from test scenario 2 prove that control in each decoupled axis can work in unison to adjust the rotor position. This is a promising result as the UIFESS project moves forward to apply the decentralized PID approach to the SLFBM.

- The initial groundwork for the implementation of AMBs on the UIFESS has been set in place. The software and hardware systems for the SB and SLFBM have been proven in the initial testing of the SB. Future UIFESS researchers will have a foundation to improve the AMB software and hardware design to move from controlling low speed flywheels to controlling high speed flywheels.
- The control of a self-bearing field regulated reluctance machine (FRRM) has been introduced. To the author's knowledge, a self-bearing FRRM has yet to be investigated in literature. Continued development of the self-bearing FRRM algorithms and characterization of its performance are areas of novel research for future UIFESS researchers.

Chapter 11

Recommendations for Future Work

This chapter recommends topics worthy of future research related to the work described in this thesis. The following topics refer to the low speed UIFESS design. The topics are presented in the order of the author's opinion of importance to the UIFESS project.

- **Redesign position sensor mounts.** As stated in 8.13, the position sensor mounts were highly susceptible to vibration and were abandoned. Although a makeshift sensor mounting solution allowed for the testing of the SB, the makeshift solution is not a permanent one. A complete redesign of the position sensor mounts is required to prevent mechanical vibrations from degrading the performance of the SB and SLFBM position (air gap) control systems.
- **Complete the initial testing of the SLFBM.** The bearing function of the SLFBM needs to be tested in two axes to verify the decentralized PID control scheme presented in Section 6.5. However, before the SLFBM can be tested experimentally, the discrete SLFBM PID position controllers must be designed and verified using the Simulink model in [17].
- **Complete the design of the rotation algorithm.** Design of the speed controller and torque controller is needed. The SLFBM control software must also be written. In addition, characterization of the FRRM torque must be obtained experimentally to provide an accurate relationship between FRRM torque and coil currents i_d and i_q .
- **Perform a complete SLFBM test.** The rotation and bearing function algorithms of the SLFBM must be implemented and tested simultaneously.
- **Determine rotor stability for all potential rotor speeds.** The dynamic stability of the rotor with respect to rotation speed must be found to provide an upper

bound for rotor speed utilizing the decentralized PID control scheme. This avenue of future work would also draw from work in [17]. This analysis will help characterize the performance requirements of the SB and SLFBM PID position controllers, which will require redesign to account for these new performance requirements.

- **Investigate other controller types for underlying current control.** The current switching ripple may improve by moving away from pure hysteresis current control. A double band hysteresis current controller or a pulse-width modulation (PWM) based proportional-integral (PI) controller may provide better performance from the underlying current control.
- **If necessary, move to parallel/conical decomposition control.** If rotor stability poses an issue at speeds attainable by the UIFESS, parallel/conical decomposition control should be investigated. Decentralized PID control can be easily extended and adapted into a parallel/conical control scheme. This scheme promises better stability at higher speeds and is described in reference [1].
- **Bearing loss analysis for SB and SLFBM.** Determination of the SB and SLFBM losses will be extremely important to characterize the efficiency of the UIFESS system.

References

- [1] G. Schweitzer, E. H. Maslen, et al. *Magnetic Bearings: Theory, Design, and Application to Rotating Machinery*. Springer, 2009.
- [2] B. Bolund, H. Bernhoff, and M. Leijon. “Flywheel energy and power storage systems.” In: *Renewable & Sustainable Energy Reviews* (2005).
- [3] R. A. Johnston. *All Things Medieval: An Encyclopedia of the Medieval World*. ABC-CLIO, 2011.
- [4] M.I. Daoud et al. “On the development of flywheel storage systems for power system applications: A survey.” In: *Electrical Machines (ICEM), 2012 XXth International Conference on*. Sept. 2012, pp. 2119–2125. DOI: 10.1109/ICELMach.2012.6350175.
- [5] I. Hadjipaschalis, A. Poullikkas, and V. Efthimiou. “Overview of current and future energy storage technologies for electric power applications.” In: *Renewable and Sustainable Energy Reviews* 13.6–7 (2009), pp. 1513–1522. ISSN: 1364-0321. DOI: <http://dx.doi.org/10.1016/j.rser.2008.09.028>. URL: <http://www.sciencedirect.com/science/article/pii/S1364032108001664>.
- [6] V. J. Lyons et al. *Space Power and Energy Storage Roadmap*. Tech. rep. NASA, Apr. 2012.
- [7] S. Vazquez et al. “Recent advances on Energy Storage Systems.” In: *IECON 2011 - 37th Annual Conference on IEEE Industrial Electronics Society*. Nov. 2011, pp. 4636–4640. DOI: 10.1109/IECON.2011.6120075.
- [8] F.A. Bhuiyan and A. Yazdani. “Energy storage technologies for grid-connected and off-grid power system applications.” In: *Electrical Power and Energy Conference (EPEC), 2012 IEEE*. Oct. 2012, pp. 303–310. DOI: 10.1109/EPEC.2012.6474970.
- [9] R. Pena-Alzola et al. “Review of flywheel based energy storage systems.” In: *Power Engineering, Energy and Electrical Drives (POWERENG), 2011 International Conference on*. May 2011, pp. 1–6. DOI: 10.1109/PowerEng.2011.6036455.

- [10] H. Bleuler. “A Survey of Magnetic Levitation and Magnetic Bearing Types.” In: *JSME International Journal* (1992).
- [11] S. Earnshaw. “On the Nature of the Molecular Forces which Regulate the Constitution of the Luminiferous Ether.” In: *Transactions Of the Cambridge Philosophical Society* Vol. 7 (1842), pp. 97–112.
- [12] R. A. Rarick. “Control of an Active Magnetic Bearing With and Without Position Sensing.” MS thesis. Cleveland State University, 2007.
- [13] G. Schweitzer. “Active magnetic bearings - chances and limitations.” In: *The 6th IFToMM International Conference on Rotor Dynamics*. 2002, pp. 1–14.
- [14] F. Wolff. *Flywheel Energy Storage Technology Being Developed*. Tech. rep. NASA, Mar. 2001.
- [15] *Magnetic bearings-from product innovation to proven solutions*. URL: <http://evolution.skf.com>.
- [16] K. Ramus. “Power Electronic Components and Hardware for an Experimental Flywheel Energy Storage System.” MS thesis. University of Idaho, 2014.
- [17] B. Wimer. “Dynamic Model and Design of an Integrated Flywheel Energy Storage System.” MS thesis. University of Idaho, 2014.
- [18] J. W. Beams, J.L. Young, and J. W. Moore. “The Production of High Centrifugal Fields.” In: *Journal of Applied Physics* 17.11 (Nov. 1946), pp. 886–890. ISSN: 0021-8979. DOI: 10.1063/1.1707658.
- [19] R. Larssonneur. “Design and Control of Active Magnetic Bearing Systems for High Speed Rotation.” PhD thesis. Swiss Federal Institute of Technology, 1990.
- [20] *International Symposium on Magnetic Bearings*. URL: www.magneticbearings.org.

- [21] H. Bleuler et al. “Application of digital signal processors for industrial magnetic bearings.” In: *Control Systems Technology, IEEE Transactions on* 2.4 (Dec. 1994), pp. 280–289. ISSN: 1063-6536.
- [22] H. Bleuler. “Decentralized Control of Magnetic Rotor Bearing Systems.” PhD thesis. Swiss Federal Institute of Technology, 1984.
- [23] C. Wei and D. Soffker. “Improving PID-Control of AMB-Rotor System Design I: Optimization Strategy.” In: *Proceedings of ISMB13*. 2012.
- [24] S. Myburn. “The development of a fully suspended AMB system for a high-speed flywheel application.” MS thesis. North-West University, South Africa, 2007.
- [25] P. Kascak. “Fully Levitated Rotor Magnetically Suspended by Two Pole Pair Separated Conical Motors.” PhD thesis. Case Western Reserve University, 2010.
- [26] P. Anantachaisilp, Z. Lin, and P. Allaire. “PID Tuning Methods for Active Magnetic Bearing Systems.” In: *Proceedings of ISMB13*. 2012.
- [27] J. Ritonja, Bostjan Polajzer, and D. Dolinar. “Decentralized Control for Active Magnetic Bearings.” In: *Power Electronics and Motion Control Conference, 2006. EPE-PEMC 2006. 12th International*. Aug. 2006, pp. 1413–1418. DOI: 10.1109/EPEPEMC.2006.4778601.
- [28] S. Liu and S. Xuecheng. “Robust PID Controller Design for Active Magnetic Bearing.” In: *Proceedings of ISMB7*. 2000.
- [29] S. Sivrioglu, K. Nonami, and M. Saigo. “Low power consumption nonlinear control with \mathcal{H}_∞ compensator for a zero-bias flywheel AMB system.” In: *Journal of Vibration and Control* 10.8 (Aug. 2004), pp. 1151–66.
- [30] U. Schonhoff et al. “Implementation results of μ -synthesis control for an energy storage flywheel test rig.” In: *Proceedings of ISMB7*. 2000.

- [31] B. H. Kenny and P. E. Kascak. "Sensorless Control of Permanent Magnet Machine for NASA Flywheel Technology Development." In: *International Energy Conversion Engineering Conference*. 2002.
- [32] J. H. Lee et al. "A Study on the Design Procedure of the Eight Pole Magnetic Bearings for the Inner-rotor and the Outer-rotor Type." In: *Journal of Electrical Engineering and Technology* 8.6 (July 2013), pp. 1424–1430.
- [33] H. Chang and S.-C. Chung. "Integrated design of radial active magnetic bearing systems using genetic algorithms." In: *Mechatronics* 12 (2002), pp. 19–36.
- [34] V. Gourishankar. *Electromechanical Energy Conversion*. International Textbook Company, 1965, pp. 186–199.
- [35] L. Bakay et al. "Losses in an optimized 8-pole radial AMB for Long Term Flywheel Energy Storage." In: *Electrical Machines and Systems, 2009. ICEMS 2009. International Conference on*. 2009, pp. 1–6. DOI: 10.1109/ICEMS.2009.5382789.
- [36] L. Kucera. *Robustness of Self-Sensing Magnetic Bearing*. Tech. rep. ETH Zurich, 1997.
- [37] G. Schweitzer and R. Lange. "Characteristics of a Magnetic Rotor Bearing for Active Vibration Control." In: *Conference on Vibrations in Rotating Machinery*. Instn. of Mech. Engrs., Cambridge. 1976.
- [38] C. R. Sabirin et al. "Modeling and Digital Control of an Active Magnetic Bearing System." In: *Rev. Roum. Sci. Techn. – Électrotechn. et Énerg.* 57 (2007), pp. 157–181.
- [39] K. J. Astrom. *Control System Design*. Lund Institute of Technology. 2002.
- [40] S. M. Fadali and A. Visioli. *Digital Control Engineering*. Academic Press, 2009.

- [41] W. Zhang and Y. Hu. “A Prototype of Flywheel Energy Storage System Suspended by Active Magnetic Bearings with PID controller.” In: *Power and Energy Engineering Conference, 2009. APPEEC 2009. Asia-Pacific*. Mar. 2009, pp. 1–4.

- [42] D. C. Meeker. *Finite Element Method Magnetics*. (Version 4.2), <http://www.femm.info>.

- [43] I. M. Higginson. “Force Density and Radial Stiffness Development for Low Idle Loss Machine Topologies.” MS thesis. University of Idaho, 2011.